

Contents

2	1 Introduction	3
3	2 Pixel detectors	5
4	2.1 Signal formation	5
5	2.2 Charge Coupled Devices	7
6	2.3 Hybrid pixels	7
7	2.4 CMOS MAPS and DMPAS	9
8	2.4.1 DMAPS: large and small fill factor	10
9	2.4.2 A modified sensor	11
10	2.5 Analog front end	13
11	2.5.1 Preamplifier	13
12	2.6 Readout logic	14
13	3 Use of pixel detectors	17
14	3.1 Tracking in HEP	17
15	3.1.1 Hybrid pixels at LHC and at SuperKEKB	18
16	3.1.2 First attempts to MAPS	21
17	3.2 Other applications	23
18	3.2.1 Applicability to FLASH radiotherapy	23
19	4 TJ-Monopix1	28
20	4.1 The sensor	29
21	4.2 Front end	31
22	4.2.1 ALPIDE-like	32
23	4.3 Readout logic	33
24	5 Arcadia-MD1	37
25	5.1 The sensor	37
26	5.1.1 Two different FE flavor	38
27	5.2 Readout logic and data structure	38
28	5.2.1 Matrix division and data-packets	38
29	6 Characterization	42
30	6.1 TJ-Monopix1 characterization	42
31	6.1.1 Threshold and noise: figure of merit for pixel detectors	42
32	6.1.2 Linearity of the ToT	46
33	6.1.3 Calibration of the ToT	47
34	6.1.4 Changing the bias	51

35	6.1.5 Measurements with radioactive sources	52
36	6.1.6 Dead time measurements	55
37	6.2 ARCADIA-MD1 characterization	57
38	7 Test beam measurements	61
39	7.1 Apparatus description	61
40	7.1.1 Accelerator	62
41	7.1.2 Mechanical carriers	63
42	7.2 Measurements	63
43	7.2.1 MIP spectrum using cosmic rays as source	68
44	A Pixels detector: a brief overview	69
45	A.1 Radiation damages	69
46	Bibliography	72
47	Characterization of monolithic CMOS pixel sensors for charged particle detectors and	
48	for high intensity dosimetry	

⁴⁹ **Chapter 1**

⁵⁰ **Introduction**

⁵¹ Since the 1980s, when the fabrication of device with very small electrodes (50-100 μm)
⁵² became a practical possibility, pixel detectors have been widely employed for imaging and
⁵³ tracking charged particles in the vertex region of experiments at accelerators. Thanks to
⁵⁴ their excellent spatial resolution, today even better than 10 μm , they allow for true three
⁵⁵ dimensional space-point determination even at high particle fluxes and in particular for
⁵⁶ the identification of secondary vertices of short-lived particles such as τ and B mesons.
⁵⁷ Requirement imposed by accelerators are stringent and they will become even more so
⁵⁸ with the increase of luminosity; in this scenario CMOS Monolithic Active Pixel Sensors
⁵⁹ (MAPS), based on the technology of CMOS cameras, are being developed to improve
⁶⁰ the performance of the hybrid pixel detectors, which currently constitute the state-of-art
⁶¹ for large scale pixel detector, in particular by reducing the amount of material, power
⁶² consumption and pixel dimension. Indeed, while hybrid pixels are made by two parts, the
⁶³ sensor and the electronics, welded together through microconnections, the MAPS integrate
⁶⁴ them all on the same wafer.

⁶⁵ Experiments such as ALICE at LHC and STAR at RHIC have already introduced the
⁶⁶ CMOS MAPS technology in their detectors. ALICE Tracking System (ITS2), upgraded
⁶⁷ during the LHC long shut down in 2019-20, was the first large-area ($\sim 10 \text{ m}^2$) silicon vertex
⁶⁸ detector based on CMOS MAPS. Thanks to the reduction of the material budget, ITS2,
⁶⁹ which uses the ALPIDE chip developed by ALICE collaboration, obtained an amazing im-
⁷⁰ provement both in the position measurement and in the momentum resolution, improving
⁷¹ the efficiency of track reconstruction for particle with very low transverse momentum (by
⁷² a factor 6 at $p_T \sim 0.1 \text{ GeV}/c$). Further advancements in CMOS MAPS technology are
⁷³ being aggressively pursued for the ALICE ITS3 and the Belle II vertex detector upgrades
⁷⁴ (both foreseen around 2026-27), and by the R&D53 collaboration for the upgrade at HL-
⁷⁵ LHC, with the goals of further reducing the sensor thickness and improving the readout
⁷⁶ speed of the devices, while keeping power consumption at a minimum.

⁷⁷ Beside tracking, the development of pixel detectors is a very active field with many
⁷⁸ applications: a noteworthy example of detector originally used in particle physics and later
⁷⁹ employed for medical imaging, in space detectors and for art authentication, is Medipix,
⁸⁰ a hybrid system developed at CERN within the Medipix collaboration. Among medical
⁸¹ applications, a possible use of CMOS MAPS could be in dosimetry: in the last few years
⁸² the search of radiotherapy oncological treatments with high intensity beams (FLASH
⁸³ mode) is requiring new dosimeters, both for the therapies as well as new beam-monitors
⁸⁴ (especially for focused very high energy electron beams), which are capable of deal with

85 extreme dose rate (up to 40 Gy/s).

86 I have studied the characteristics of two ALPIDE-like CMOS MAPS chips and tested
87 them under different front end configuration. The first chip, the TJ-Monopix1 from the
88 Monopix series, is a TowerJazz MAPS fabricated in 180 nm CMOS technology with an
89 active area of $1 \times 2 \text{ cm}^2$ (448×224 pixels) and is one of the prototypes for the Belle II vertex
90 detector upgrade. The second chip, called Main Demonstrator-1, has an active area of
91 $1.28 \times 1.28 \text{ cm}^2$ (512×512 pixels) is produced by LFoundry in 110 nm CMOS technology
92 and designed by the ARCADIA (Advanced Readout CMOS Architectures with Depleted
93 Integrated sensor Arrays) group; it is intended to be a general purpose device with possible
94 use in medical scanners, space experiments, future lepton colliders and also possibly X-ray
95 applications with thick substrates. The main differences between the two chips are in the
96 output signal type and in the readout sequence of the matrix. Concerning the former,
97 TJ-Monopix1 returns an analog output information, that is the time over threshold of the
98 pulse, which can be related with the charge released by the particle in the sensor, while
99 MD1 returns only a digital information; regarding the latter, instead, TJ-Monopix1 has
100 a completely sequential readout, while MD1 roughly combines the information of the hits
101 before the readout in order to reduce the data transmission time.

102 I have set up the test systems for the two chips in the INFN clean laboratories and char-
103 acterized the devices electrically and with radioactive sources in terms of threshold, noise,
104 dead time and analog response. The mean minimum stable threshold evolved through
105 different generation of chips and nowadays it is less than 500 e^- , allowing thinner sensors
106 with smaller signals: TJ-Monopix1 has proven to be in agreement with this trend, having
107 a threshold of $\sim 400 \text{ e}^-$, to be compared with the 2000 e^- signal expected for a minimum
108 ionizing particle in an epitaxial layer of $25 \mu\text{m}$. Moreover, since one of the main challenges
109 of MAPS are the differences between pixels due to process parameters variation across
110 the wafer, which make the sensor response nonuniform, I have measured the threshold
111 and noise dispersion across the matrix, which I found to be 40 e^- and 2 e^- respectively. I
112 have also studied the response of the analog signal recorded by TJ-Monopix1, that is the
113 time over threshold, and performed a calibration of its absolute value using a Fe55 X-ray
114 source. All these measurements are important to verify the design parameters of the chip
115 and to validate the chip simulation.

116 As conclusion of the measurement campaign, we have tested TJ-Monopix1 at very
117 high intensity using the electron beam of the new ElectronFlash accelerator designed for
118 both medical research and R&D in FLASH-radiotherapy and recently installed at Santa
119 Chiara hospital in Pisa. I have participated in the design of the setup needed for testbeam
120 measurement and I am currently working on the analysis of the data collected.

₁₂₁ **Chapter 2**

₁₂₂ **Pixel detectors**

₁₂₃ Pixel detectors are semiconductor detectors which are segmented in two dimensions: this
₁₂₄ distinguish them from the strip detectors, such that a single plane of detector already
₁₂₅ provides both the coordinates of impact of the detected particle. Their operation is based
₁₂₆ on the p-n junction (fig. 2.1). A p-n junction is built by bringing in contact two n
₁₂₇ and p doped silicon crystals. At the boundary, recombination of both charge carriers
₁₂₈ occurs forming a region, the depletion zone, which is free of charge carriers. The charged
₁₂₉ donors⁺ and acceptor⁻, that remain ionised in the n-type and p-type regions, features a
₁₃₀ space charge and create an electric field across the junction, causing a drift current in the
₁₃₁ opposite direction to the diffusion one, through which the junction reaches an equilibrium
₁₃₂ state. Assuming a constant space change, the electric field is linear and reach a maximum
₁₃₃ at the boundary of the *p* and *n* layers.

₁₃₄ **2.1 Signal formation**

₁₃₅ When a charged particle passes through a pixel and loses energy by ionization only a
₁₃₆ part of that energy is used to generate electron-hole pairs, since another part is used for
₁₃₇ other processes, as lattice excitation. The average energy needed to create a pair at 300 K
₁₃₈ in silicon is $w_i = 3.65 \text{ eV}$, that is more than the mean ionization energy because of the
₁₃₉ interactions with phonon, since for a minimum ionizing particle (MIP) the most probable
₁₄₀ value (MPV) of charge released in the semiconductor is $0.28 \text{ keV}/\mu\text{m}$, hence the number
₁₄₁ of electrons-vacuum pairs is:

$$\langle \frac{dE}{dx} \rangle \frac{1}{w_i} \sim 80 \text{ e/h} \sim \frac{1.28 \cdot 10^{-2} fC}{\mu\text{m}} \quad (2.1)$$

₁₄₂ Because of the splitting of the energy depositon between the two different processes, the
₁₄₃ number $N_{e/h}$ of couples generated undergoes fluctuations that usually follow a Poisson
₁₄₄ distribution; thus the fluctuations of $N_{e/h}$ is equal to $\sigma_{e/h} = \sqrt{N_{e/h}}$. Under the constraint
₁₄₅ of complete absorption of a particle, the energy resolution improves of a factor \sqrt{F} , where
₁₄₆ F is called the Fano factor and determines the ultimate limit of energy resolution for
₁₄₇ semiconductors. F is a function of the material and temperature and for silicon is equal
₁₄₈ to ~ 0.115 .

₁₄₉ In order to avoid a loss signal, it is fundamental that pairs e/h are produced in the
₁₅₀ depleted region of the semiconductor, where the probability of recombination with charge
₁₅₁ carriers is low. For this reason pixel detectors are commonly reverse biased: a positive
₁₅₂ bias is given to the *n* electrode and a negative to the *p* in order to grow the depletion zone

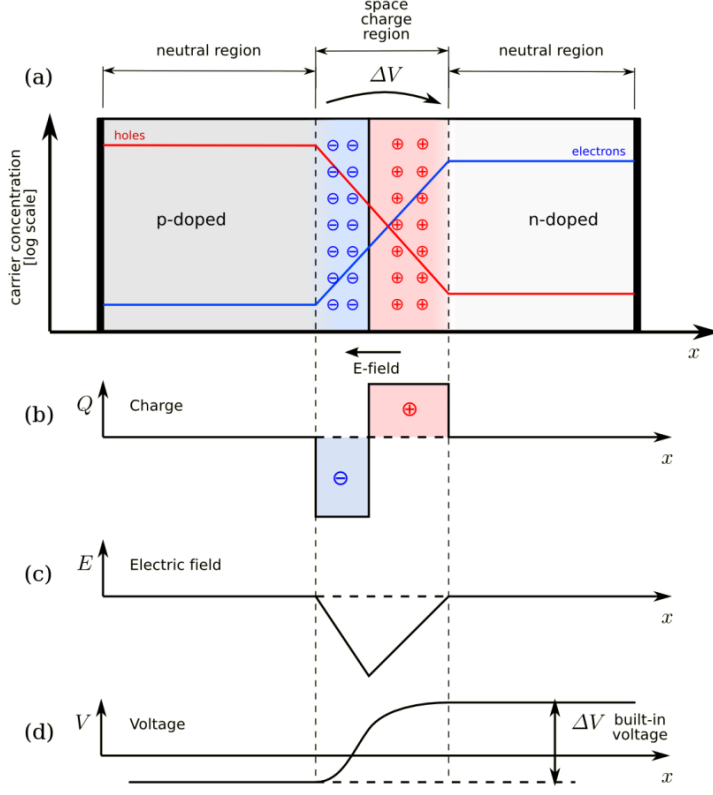


Figure 2.1: The structure of a p-n junction. (a) structure, (b) space charge density, (c) electric field distribution and (d) potential distribution.

in the epitaxial layer within the bulk. The width of the depletion region depends on the external bias V_{ext} , the resistivity ρ and also with the dopant:

$$d_n \sim 0.55 \sqrt{\frac{\rho}{\Omega cm} \frac{V_{ext}}{V}} \mu m \quad d_p \sim 0.32 \sqrt{\frac{\rho}{\Omega cm} \frac{V_{ext}}{V}} \mu m \quad (2.2)$$

Thus, high resistivity wafers ($100 \Omega cm - k\Omega cm$) are typically preferred because they allow bigger depletion zone with smaller voltage bias.

The charges created within the sensor are separated by an electric field and collected at their respective electrodes (p for holes and n for electrons)¹; by the drift of these charges, a signal i_e is generated on the electrode e as stated by the Shockley-Ramo's theorem:

$$i_e(t) = -q v(t) E_{WF,e} \quad (2.3)$$

where $v(t)$ is the instantaneous velocity of the charge q and E_{WF} is the weighting field, that is the field obtained biasing the electrode e with 1V and all the others with 0V. The drift velocity of the charge depends on the electric field and on the mobility of the particle:

$$v = \mu(E) E \quad (2.4)$$

where $\mu(E)$ is a function of the electric field and is linear in E only for small E : at higher values the probability of interactions with optical phonons increases, the mobility drops

¹Even if in principle both the electrode can be used to read the signal, for pixel detectors, where the number of channel and the complexity of readout are high, only one is actually used. In strip and pad detectors, instead, is more common a dual-side readout

and this leads to a saturation of the velocity (fig. 2.2). Typical values for electrons and holes mobility in silicon at room temperature are $\mu_n \sim 1450 \text{ cm}^2/\text{Vs}$, $\mu_h = 500$.

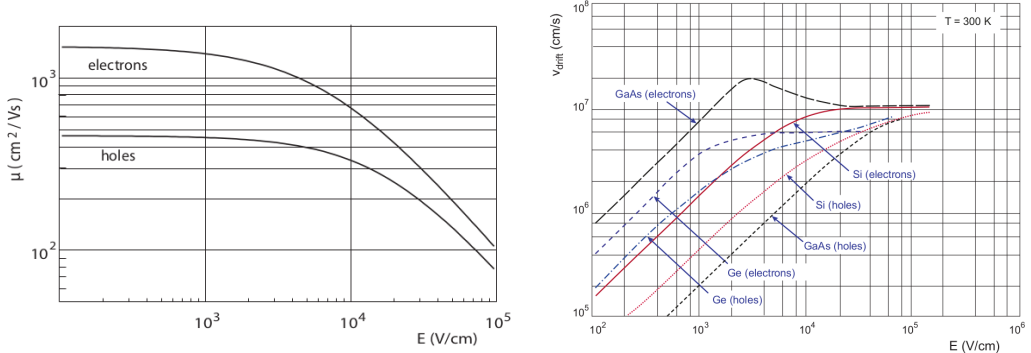


Figure 2.2: (a) Dependence of the mobility on the electric field. (b) Drift velocity at room temperature in different semiconductors

2.2 Charge Coupled Devices

In CCDs the charge is created in a very thin active epitaxial layer (typically 10 μm , maximally about 30 μm) and then locally stored in a potential minimum which is created by a MOS structure. The size of the CCD cells is typically in the range 10 μm to 20 μm such that spatial resolutions are of the order of a few micrometres. The collected charges are moved stepwise from electrode to electrode (thus so called 'bucket chain') by applying a potential with a clock with frequency of \sim MHz; despite of such high frequency, the readout chain is completely sequential and this makes the entire process comparatively slow (tens of ms). A particular type of CCD, the pnCCDs, are typically used to detect low energy (<10 keV) x-ray photons for their homogeneous spatial detection efficiency of photons. The pnCCDs have a sideward depletion similar to silicon drift chambers that makes the electric field stronger, compared with the normal CCDs. The pnCCDs designed for photon imaging are often fabricated with high Z materials, to increase absorption efficacy.

2.3 Hybrid pixels

Hybrid pixels, which currently are the state-of-art technology for large scale pixel detectors in most particle physics experiments, are made of two parts welded together through microconnection (bump bond): the sensor and the electronics (fig. 2.3a). They provide a practical system where the sensor and the ASIC (application specific integrated circuit) can be optimized separately, which makes them really fast, capable of handling with rate up to GHz. However a disadvantage of hybrid pixels is that they must be connected before testing. For reasons related with the historical development, the n⁺-in-n sensors were the first to be used; they demanded double-sided processing which guarantees the detector functionality both before and after the type inversion of the n⁻ doped bulk into p-type after high quantity of radiation. The pn-diode is initially on the unstructured backside of the sensor, while after, the depletion zone grows from the electrode side into the bulk. This ensures that the signal can be sensed on the pixels even if the substrate is no longer fully depleted, even though the bias voltage required for a sufficient depletion increases,

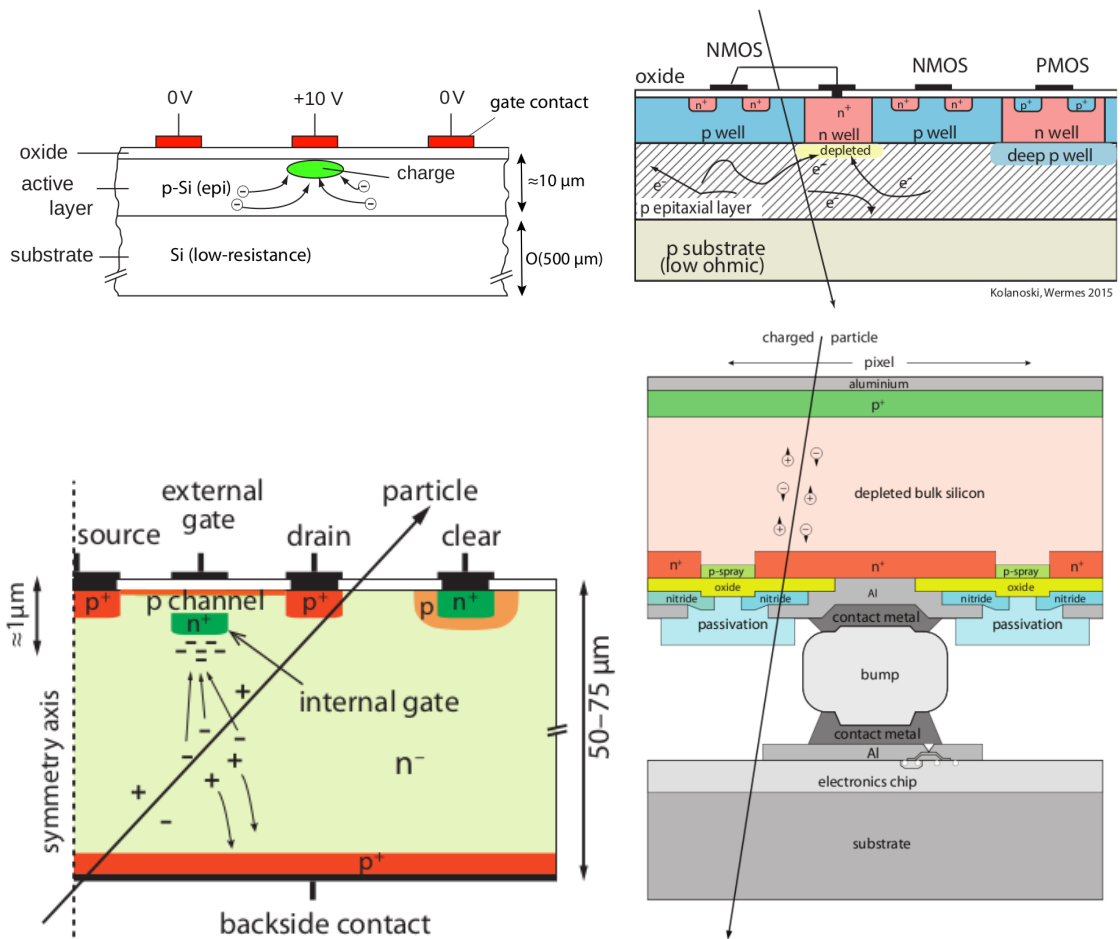


Figure 2.3: Concept cross-section of hybrid pixel (a) and of a DEPFET (b)

194 liming the detector lifetime up to a few years. With the availability of high quality p-
195 substrate material ($\gtrsim 2 \text{ k}\Omega\text{cm}$) the fabrication of n-in-p type sensors, which does not invert
196 anymore, became the preferred choise leading also a huge advance in cost reduction due
197 to no more need of double sided. However, the particular and sophisticated procedure to
198 bond sensor and ASIC makes them difficult to produce, delicate (especially when exposed
199 to high levels of radiation) and also expensive.

200 DEPFET are the first attempt towards the integration of the front end (FE) on the
201 sensor bulk: they are typically mounted on a hybrid structure but the sensor also in-
202 tegrates the first amplification stage. Each pixel implements a MOSFET (metal-oxide-
203 semiconductor field-effect transistor) transistor (a p-channel in fig. 2.3b): a hole current
204 flows from source to drain which is controlled by the external gate and the internal gate
205 together. The internal gate is made by a deep $n+$ implant towards which electrons drift
206 after being created in the depletion region; the accumulation of electrons in the region
207 underneath the n implant changes the gate potential and controls the transistor current;
208 the removal of the signal charge from the internal gate is called "Clear". DEPFET typ-
209 ically have a good S/N ratio: this is principally due to the amplification on-pixel, which
210 guarantees any charge losses, and to the large depletion region. They can be operated in-
211 dividually or integrated in the readout nodes of other detectors, as for example silicon drift
212 chambers, but they always need to be connected to an ASIC with a readout circuit on it.
213 In recent years, the sensor development was driven by an intensive R&D and prototyping
214 for x-ray imagers and the ILC vertex detector.

215 2.4 CMOS MAPS and DMPAS

216 Monolithic active pixels accommodate on the same wafer both the sensor and the FE
217 electronics, with the second one implanted on top within a depth of about $1 \mu\text{m}$ below
218 the surface. MAPS have been first proposed and realized in the 1990s and their practical
219 usage has been enabled by the development of the electronic sector, which guarantees the
220 halving of CMOS transistors dimension at least every two years, as stated by the Moore's
221 law. As a matter of fact the dimension of components, their organization on the pixel
222 area and logic density are important issues for the design and for the layout. Compared
223 to CCDs, the readout time is dramatically reduced by the in-pixel amplification and
224 discrimination, typically followed by a sparsified readout not requiring the signal to be
225 transported anymore over thousands of pixels; as aside effect, the radiation tolerance is
226 also greatly increased by sensing the signal charge directly within its own pixel.

227 A critical parameter for accelerator experiments is the material budget, which repre-
228 sents the main limit factor for momentum measurement resolution in a magnetic field;
229 since hybrid pixels are thicker (\sim hundreds of μm) than monolithic ones (even less than
230 $100 \mu\text{m}$). Using the latter the material budget can be down by a third: typical values for
231 hybrid pixels is $1.5 \% X_0$ per layer, while for monolithic $0.5 \% X_0$. Compared to MAPS,
232 among other disadvantages of hybrid pixels there is the bigger power consumption, that
233 requires also a bigger cooling system, leading to a futher increase of material.

234 Monolithic active pixel can be distinguished between two main categories: MAPS and
235 depleted MAPS (DMAPS). MAPS (figure a ??) have typically an epitaxial layer in a from
236 range $1 \mu\text{m}$ to $20 \mu\text{m}$ and, since they are not depleted, the charge is mainly collected by
237 diffusion rather than by drift. This makes the path of charges created in the bulk longer
238 than usual, making them slow (of order of 100 ns). Moreover, the collection can be partial,

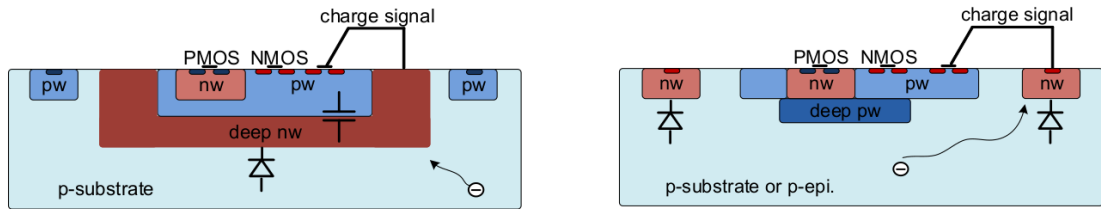


Figure 2.4: Concept cross-section with large and small fill factor

especially after irradiation of the detector (look at A for radiation damages), when the trapping probability becomes higher. In figure ?? it is shown as example of CMOS MAPS: the sensor implements an n well as collection diode; to prevent the others n wells (which contain PMOS transistor) of the electronic circuit competing in charge collection and to shield the CMOS circuit from the substrate, additional underlying deep p well are needed. DMAPS are instead MAPS depleted with d typically in $\sim 25 \mu\text{m}$ to $150 \mu\text{m}$ (eq. 2.2) which extends from the diode to the deep p-well, and sometimes also to the backside (in this case if one wants to collect the signal also on this electrode, additional process must be done).

2.4.1 DMAPS: large and small fill factor

There are two different sensor-design approaches (figure 2.4) to DMAPS:

- large fill factor: a large collection electrode that is a large deep n-well and that host the embedded electronics
- small fill factor: a small n-well is used as charge collection node

To implement a uniform and stronger electric field, DMAPS often uses large electrode design that requires multiple wells (typically four including deep n and p wells); with this layout the total capacity of the sensor increases because of the addition of a new term (fig. 2.5), which contributes to the total amplifier input capacity ($\sim 100 \text{ fF}$). In addition to the capacity between pixels (C_{pp}) and between the pixel and the backside (C_b), a non-negligible contribution comes from the capacities between wells (C_{SW} and C_{WW}) needed to shield the embedded electronics. These capacities affect the thermal and $1/f$ noise of the charge amplifier and the τ_{CSA} too:

$$ENC_{thermal}^2 \propto \frac{4}{3} \frac{kT}{g_m} \frac{C_D^2}{\tau_{sh}} \quad \tau_{CSA} \propto \frac{1}{g_m} \frac{C_D}{C_f} \quad (2.5)$$

where g_m is the transconductance, τ_{sh} is the shaping time. Among the disadvantages coming from this large input capacity there is a coupling between the sensor and the electronics resulting in cross talk noise on neighbouring electrodes; indeed, since digital switching in the FE electronics does a lot of oscillations, this problem is especially connected with the intra wells capacities. So, larger charge collection electrode sensors provide a uniform electric field in the bulk that results in short drift path and so in good collection properties, especially after irradiation, when trapping probability can become an issue.

The small fill-factor variant, instead, benefits from a small capacity (5 fF to 20 fF), but suffers from a non uniform electric field and from all the issue related to that (slowness and high trapping probability). As we'll see these two different types of sensor require

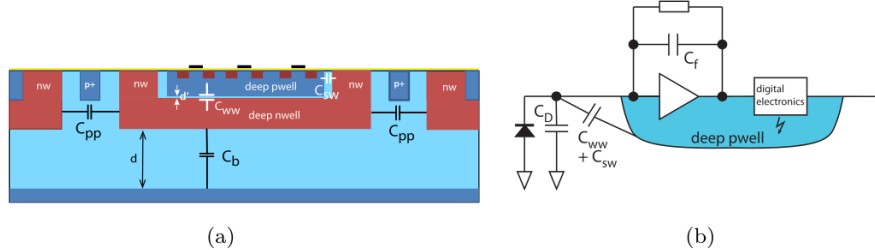


Figure 2.5: C_{pp} , C_b , C_{WW} , C_{SW}

	small fill factor	large fill factor
small sensor C	✓ (< 5 fF)	✗ (~ 100 200 fF)
low noise	✓	✗
low cross talk	✓	✗
velocity performances	✓	✗ (~ 100 ns)
short drift paths	✗	✓
radiation hard	✗	✓

Table 2.1: Small and large fill factor DMAPS characteristics

271 different amplifier: the large electrode one is coupled with a charge sensitive amplifier,
272 while the small one with a voltage amplifier (sec 2.5.1).

273 2.4.2 A modified sensor

274 A process modification, developed by CERN in collaboration with the foundries, which
275 has become the standard solution to combine the characteristics of a small fill factor
276 sensor (small input amplifier capacity) and of a large fill factor sensor (uniform electric
277 field), is the one carried out for ALICE upgrade about ten years [1]. A compromise
278 between the two sensors could also be making smaller pixels, but this solution requires
279 reducing the electronic circuit area, so a completely new pixel layout should be though.
280 The modification consists in inserting a low dose implant under the electrode and one of
281 its advantage lies in its versatility: in fact, both standard and modified sensor are often
282 produced for testing.

283 Before the process modification, the depletion region extends below the diode towards
284 the substrate, and it does not extend much laterally, even if a high bias is applied to the
285 sensor (fig. 2.6). After the modification, two distinct pn junctions are built: one between
286 the deep p well and the n⁻ layer, and the other between the n⁻ and the p⁻ epitaxial
287 layer, extending to the whole area of the sensor. Since deep p well and the p-substrate are
288 separated by the depletion region, the two p electrodes can be biased separately² and this
289 is beneficial to enhance the vertical electric field component. The doping concentration is
290 a trimmer parameter: it must be high enough to be greater than in the epitaxial layer in
291 order to prevent the punchthrough between p-well and the substrate, but it must also be
292 low enough to allow the depletion for reasonable bias values.

²This is true in general, but it can be denied if other doping characteristics are implemented, and we will see that this is the case of TJ-Monopix1

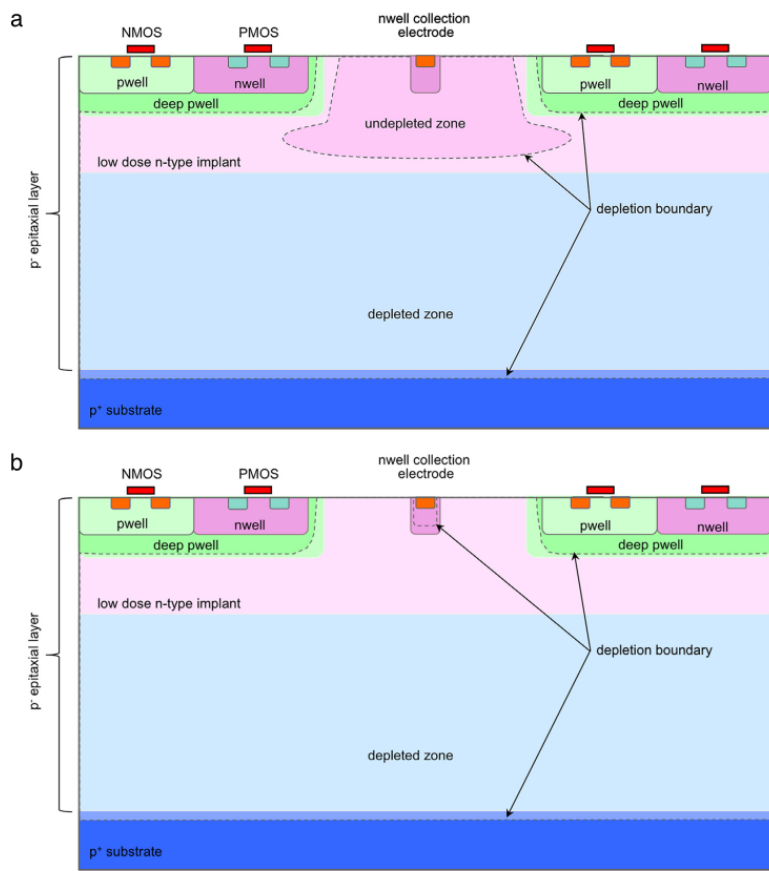


Figure 2.6: A modified process for ALICE tracker detector: a low dose n implant is used to create a planar junction. In (a) the depletion is partial, while in (b) the pixel is fully depleted.

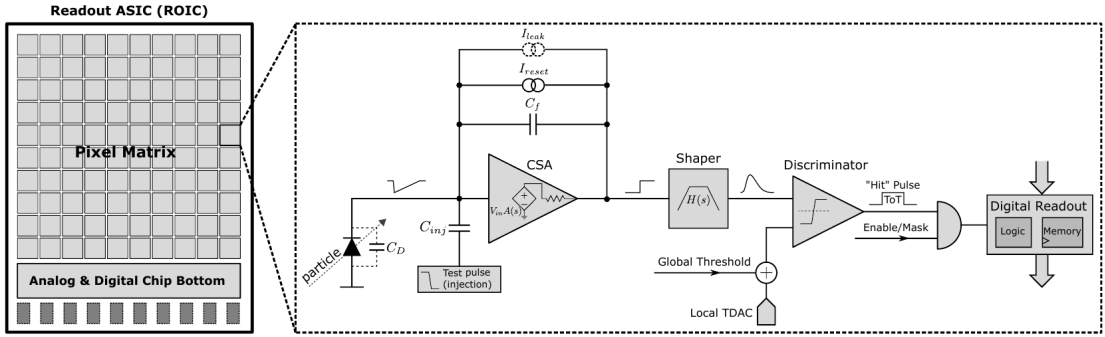


Figure 2.7: Readout FE scheme: in this example the preamplifier is a charge sensitive one (CSA) but changing the capacitive feedback into a resistive one, this can be converted in a voltage or current amplifier.

2.5 Analog front end

After the creation of a signal on the electrode, the signal enters the front end circuit (fig.2.7), ready to be molded and transmitted out of chip. Low noise amplification, fast hit discrimination and an efficient, high-speed readout architecture, consuming as low power as possible, are the goal of the readout integrated electronics (ROIC). The main parts of the analog front end chain are a preamplifier (that often is the only amplification stage) with a reset to the baseline mechanism and a leakage current compensation, a shaper (a band-pass filter) and finally a discriminator. The whole chain must be optimized and tuned to improve the S/N ratio. It is very important both not to have a large noise before the amplification stage in order to not multiply that noise, and chose a reasonable threshold of the discriminator to cut noise-hits much as possible.

2.5.1 Preamplifier

Even if circuits on the silicon crystal are only constructed by CMOS, a preamplifier can be processed as an operational amplifier (OpAmp) where the gain is determined by the input and feedback impedance (first step in figure 2.7):

$$G = \frac{v_{out}}{v_{in}} = \frac{Z_f}{Z_{in}} \quad (2.6)$$

Depending on whether a capacity or a resistance is used as feedback, respectively a charge or a voltage amplifier is used: if the voltage input signal is large enough and has a sharp rise time, the voltage sensitive preamplifier is preferred. Consequently, this flavor doesn't suit to large fill factor MAPS whose signal is already high enough: $v_{in} = Q/C_D \approx 3 \text{ fC}/100 \text{ pF} = 0.03 \text{ mV}$, but it's fine for the small fill factor ones: $v_{in} = Q/C_D \approx 3 \text{ fC}/3 \text{ pF} = 1 \text{ mV}$.

In the case of a resistor feedback, if the signal duration is longer than the discharge time ($\tau = R_S C_D$) of the detector the system works as current amplifier, as the signal is immediately transmitted to the amplifier; in the complementary case (signal duration longer than the discharge time) the system integrates the current on the C_D and operates as a voltage amplifier.

319 2.6 Readout logic

320 The readout logic includes the part of the circuit which takes the FE output signal, pro-
 321 cesses it and then transmit it out of pixel and/or out of chip; depending on the situation
 322 of usage different readout characteristics must be provided. To store the analogical in-
 323 formation (i.e. charge collected, evolution of signal in time, ...) big buffers and a large
 324 bandwidth are needed; the problem that doesn't occur, or better occur only with really
 325 high rate, if one wants record only digital data (if one pixel is hit 1 is recorded, and if not
 326 0 is recorded).

327 A common compromise is to store the time over threshold (ToT) of the pulse in clock
 328 cycle counts; this needs of relatively coarse requirement as the ToT can be trimmed down
 329 to use only a dozen bits but, being correlated (and hopefully linear) with the deposited
 330 charge, it provides a sufficient information. The ToT digitalization usually takes advantage
 331 of the distribution of a clock (namely BCID, bunch crossing identification) on the pixels'
 332 matrix. The required timing precision is better than ~ 25 ns, that corresponds to the period
 333 between bunch collisions at LHC; for such reason a reasonable BCID-clock frequency for
 pixels detector is 40 MHz.

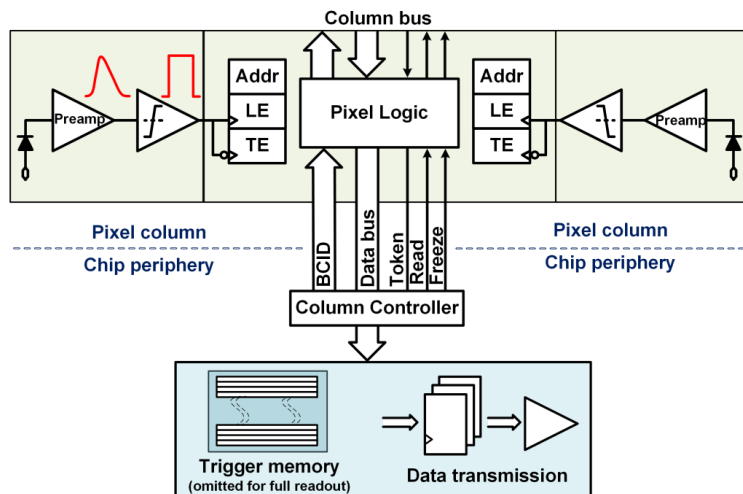


Figure 2.8: Column drain R/O scheme where ToT is saved

334 Moreover, the readout architecture can be full, if every hit is read, or triggered, if a
 335 trigger system decides if the hit must be stored or not. On one hand the triggered-readout
 336 needs buffers and storage memories, on the other the full readout, because there is no
 337 need to store hit data on chip, needs an high enough bandwidth. A triggered readout is
 338 fundamental in accelerator experiments where the quantity of data to store is very large
 339 and some selection has to be applied by the trigger: to give an order of magnitude, at LHC
 340 more than 100 TBit/s of data are produced, but the storage limit is about 100 MBit/s
 341 [2](pag. 797). Typically, the trigger signal is processed in a few μs , so the pixel gets it
 342 only after a hundred clock cycles from the hit arrival time: the buffer depth must be able
 343 to handle such high trigger latency.

344 After having taken out the data from the pixel, it has to be transmitted to the end
 345 of column (EoC) where a serializer delivers it out of chip, typically to an FPGA. There
 346 are several ways of transmitting data from a pixel to the EoC: one of the most famous
 347 is the column-drain read out, developed for CMS and ATLAS experiments [3]. All the

349 pixels in a double-column share a data bus and only one pixel at a time, according to
 350 a priority chain, can be read. The reading order circuit is implemented by shift register
 351 (SR): when a hit arrives, the corresponding data, which can be made of timestamp and
 352 ToT, is temporarily stored on a RAM until the SR allows the access to memory by data
 353 bus. Even if many readout architectures are based on the column-drain one, it doesn't suit
 354 for large size matrices. The problem is the increasing number of pixels on a column would
 355 also raise the number of pixels in the priority chain, which would result in a slowdown of
 356 the readout.

357 If there isn't any storage memory, the double-column behaves as a single server queue
 358 and the probability for a pixel of waiting a time T greater than t , with an input hit rate
 359 on the column μ and an output bandwidth B_W is [4]:

$$P(T > t) = \frac{\mu}{B_W} e^{-(B_W - \mu)t} \quad (2.7)$$

360 To avoid hit loss (let's neglect the contribution to the inefficiency of the dead time τ due
 361 to the AFE), for example imposing $P_T > t \sim 0.001$, one obtains $(B_W - \mu) t_t \sim 6$, where
 362 t_t is the time needed to transfer the hit; since t_t is small, one must have $B_W \gg \mu$, that
 means a high bandwidth [4].

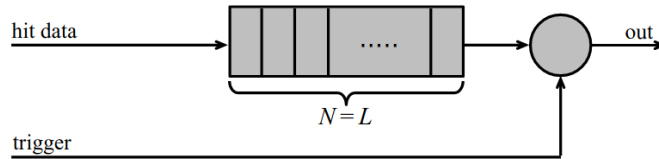


Figure 2.9: Block diagram of a pipeline buffer: N is the dimension of memory buffer and L is the trigger latency expressed in BCID cycles

363 Eq.2.7 is actually an approximation, since each pixel sees a different bandwidth de-
 364 pending on the position on the queue: the first one sees the full bandwidth, while the next
 365 sees a smaller one because it can be occasionally blocked by the previous pixel. Then,
 366 the bandwidth seen by the pixel i is $B_i = B - \sum_j \mu_j$, where μ_j is the hit rate of the j th
 367 pixel. The efficiency requirement on the bandwidth and the hit rate becomes: $B_{W,i} > \mu_i$,
 368 where the index i means that the constraint is for a single pixel; if all the N pixels on a
 369 column have the same rate $\mu = N\mu_i$, the condition reduces to $B_W > \mu$. The bandwidth
 370 must be chosen such that the mean time between hits of the last pixel in the readout chain
 371 is bigger than that. In order to reduce the bandwidth, a readout with zero suppression
 372 on pixel is typically employed; this means that only information from channels where the
 373 signal exceeds the discriminator threshold are stored.

375 If, instead, the signal is locally stored until a trigger signal arrives, the input rate to
 376 column bus μ' is reduced compared to the hit rate μ as: $\mu' = \mu \times r \times t$, where r is the
 377 trigger rate and t is the bunch crossing period. In this situation there is a more relaxed
 378 constraint on the bandwidth, but the limiting factor is the buffer depth: the amount of
 379 memory designed depends both on the expected rate μ and on the trigger latency t as
 380 $\propto \mu \times t$, which means that the higher the trigger latency the lower the hit rate to cope
 381 with.

382 In order to have an efficient usage of memory on pixels' area it's convenient grouping
 383 pixels into regions with shared storage. Let's compare two different situations: in the first
 384 one a buffer is located on each pixel area, while in the second one a core of four pixels

385 share a common buffer (this architecture is commonly called FE-I4).

Consider a 50 kHz single pixel hits rate and a trigger latency of 5 μ s, the probability of

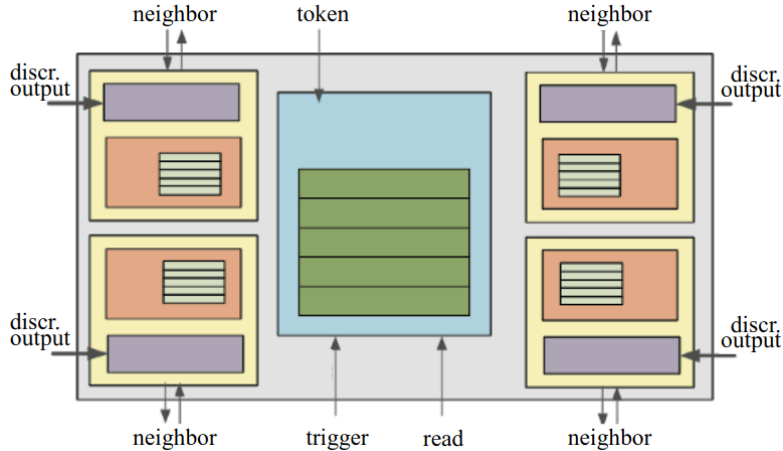


Figure 2.10: Block diagram of the FE-I4 R/O. Read and memory management section is highlighted in light blue; latency counters and trigger management section are highlighted in green; hit processing blocks are highlighted in purple; ToT counters and ToT management units are highlighted in orange

386

387 losing hits is:

$$P(N > 1|\nu) = 1 - P(N = 0|\nu) - P(N = 1|\nu) = 1 - e^{-\nu}(1 + \nu) \approx 2.6\% \quad (2.8)$$

388 where I have assumed a Poissonian distribution with mean $\nu = 0.25$ to describe the counts
389 N.

390 To get an efficiency ϵ greater than 99.9 % a 3 hit depth buffer is needed:

$$P(N > 3|\nu) = 1 - \sum_{i=0}^3 P(N = i|\nu) < 0.1\% \quad (2.9)$$

391 Consider the second situation: if the average single pixel rate is still 50 kHz, grouping four
392 pixels the mean number of hits per trigger latency is $\nu = 0.25 \times 4 = 1$. To get an efficiency
393 of 99.9% (eq. 2.9) a buffer depth of 5 hits in the four-pixels region, instead of 3 per pixels,
394 is needed.

395 **Chapter 3**

396 **Use of pixel detectors**

397 The relation between the development of cameras and that of pixel detectors dates back
398 to 1969, when the idea of CCDs, for which Boyle and Smith were awarded the Nobel Prize
399 in Physics in 2009, revolutionized photography allowing light to be captured electronically
400 instead of on film. Even though the CMOS technology already existed at the time the
401 CCDs spread, the costs of productions were too high to allow the diffusion of these sensors
402 for the following 20 years. From that moment on, the fast diffusion of CMOS was mainly
403 due to the less cost than CCD, and the less power supply required. Nowadays CCDs
404 are still preferred over MAPS in astronomy, where the astronomical sources' rate are low
405 enough to cope with slow readout time (tens of ms). 0

406 The principal use cases of pixel detectors are particle tracking and imaging: in the
407 former case individual charged particles have to be identified, in the latter instead an
408 image is obtained by the usually un-triggered accumulation of the impinging radiation.
409 Also the demands on detectors performance depends on their usage, in particular tracking
410 requires high spatial resolution, fast readout and radiation hardness.

411 **3.1 Tracking in HEP**

412 At first the physics world overlooked the CCDs, and all pixel in general, as against the
413 gaseous detector for tracking: there was no need to replace these ones which had a sufficient
414 good resolution ($100\text{ }\mu\text{m}$). Since 1974, with the measurement of the invariant mass of the
415 J/Psi and the affirmation of the quark model, all experiments start to look for better
416 spatial resolutions in order to achieve the possibility of reconstructing short lived particle.

417 Historically, the first pixel detector employed in particle physics was a CCD: it was
418 installed in the spectrometer at the CERN's Super Proton Synchrotron (SPS) by the
419 ACCMOR Collaboration (Amsterdam, CERN, Cracow, Munich, Oxford, RAL) at mid
420 1980s, with the purpose of studying the (at the time) recently-discovered charm particles.
421 The second famous usage of CCDs took place at SLAC in the Large Detector (SLD) during
422 the two years 1996-98, where the CCD technology was adopted instead of the microstrip
423 detectors for their excellent spatial resolution (cell size $22\times 22\text{ }\mu\text{m}^2$ giving a resolution of
424 $\sim 5\text{ }\mu\text{m}$) thanks to the sufficient time for readout between two successive collisions (160 ms).

425 From that period on particle tracking in experiments have been transformed radically:
426 it was mandatory for HEP experiments to build an inner vertex detector, where the general
427 tasks are:

- 428 • pattern recognition with the identification of particle tracks at large backgrounds and

429 pile-up

- 430 • measurement of vertices (primary and secondary)
- 431 • multi-track and vertex separation in the core of jets
- 432 • measurement of specific ionization
- 433 • momentum measurement combining with other detectors informations

434 In 1991, the more demanding environments led to the development of hybrid pixel
435 detectors: a dedicated collaboration, RD19, was established at CERN with the specific goal
436 of defining a semiconductor micropattern detector with an incorporated signal processing
437 at a microscopic level. In those years a wide set of prototypes of hybrid pixel has been
438 manufactured; among the greatest productions a mention goes to the huge ATLAS and
439 CMS vertex detectors. From the middle of 2013 a second collaboration, RD53, has been
440 established with the new goal of finding a pixel detector suitable for phase II future
441 upgrades of those experiments. Even if the collaboration is specifically focused on design
442 of hybrid pixel readout chips (aiming to 65 nm tecnique so that the electronics fits within
443 the pixel area), also other options have been taken in account and many test have been done
444 on MAPS. Requirements imposed by HL-LHC will become tigher in time: for example, a
445 dose and radiation of 5 Mrad and 10^{16} NIEL are exepected after 5 years of operation. Time
446 resolution, material budget and power consumption are also issues for the upgrade: to
447 distinguish different events from different bunches a time resolution better than 25 ns for
448 a bunch crossing frequency of 40 MHz is required, and also a material budget lower than
449 2% and a power consuption lower than 500 mW/cm² are required.

450 Amidst the solutions proposed 3D silicon detector, invented by Sherwood Parker in
451 1995, and MAPS are the most promising. In 3D sensors the electrode is a narrow column
452 of n-type implanted vertically across the bulk instead of being implanted on the wafer's
453 surface. The charge produced by the impinging particle is then drifted transversally within
454 the pixel, and, as the mean path between two electrode can be soufficent low, the trap
455 probability is not an issue. Even if 3D detector are adequately radiation hard and are a
456 strong contender for hybrid pixel modules, especially in the innermost pixel detector layer,
457 the fabrication process is currently low volume, making them unlikely to cover large areas.

458 3.1.1 Hybrid pixels at LHC and at SuperKEKB

459 **ATLAS**

460 With CMS, ATLAS is one of two general-purpose detectors at the LHC and has the largest
461 volume detector ever constructed for a particle collider (46 m long and 25 m in diameter).
462 The Inner Tracker (ITk) consists of three different systems all immersed in a magnetic
463 field parallel to the beam axis whose main components are: the pixel, the micro-strips and
464 transition radiation trackers. Concerning the pixel detector, they installed a 3-layer hybrid
465 pixel detector in 2007 and an additional one inserted within the original detector envelope
466 and therefore called insertable B-layer (IBL) in 2014. 92 million pixels are divided in 4
467 barrel layers and 3 disks in each end-cap region, covering a total area of 1.9 m² and having
468 a 15 kW of power consumption.

469 As stated by the ATLAS collaboration the pixel detector is exposed by an extreme
 470 particle flux: "By the end of Run 3¹, the number of particles that will have hit the
 471 innermost pixel layers will be comparable to the number it would receive if it were placed
 472 only a few kilometres from the Sun during a solar flare". Considering that the particle
 473 density will increase even more with HL-LHC, radiation hardness is definitively target to
 474 achieve. The most ambitious goal is employ a MAPS-based detector for the inner-layer
 475 barrels, and for this reason the RD53 collaboration is designing many MAPS prototypes
 476 (as for example TJ-Monopix1, which I will talk about in chapter 4) and performing test.
 477 Up to now this possibility will be eventually implemented during the second phase of the
 478 HL-LHC era, as at the start of high-luminosity operation the selected option is the hybrid
 479 one. The sensor will be bonded with ITkPix, the first full-scale 65 nm hybrid pixel-readout
 480 chip developed by the RD53 collaboration. Regarding the sensor, a valuable option is
 481 using 3D pixels, which have already proved themselves in ATLAS, for the IBL, where they
 482 were introduced in a limited acceptance range and introduced a new readout integrated
 483 circuit called FE-I4. Also the complexity of the readout will be raised, as the number of
 484 pixels will be increased of a factor about 7, passing from 92 millions to 6 billion.

485 CMS

486 The CMS hybrid pixel detector has been upgraded in 2017, when, with the replacement
 487 of a piece of the beam pipe, a layer has been added to the detector at 3 cm from it.
 488 124 million pixels are divided between the barrel pixel detector (BPIX) and the forward
 489 disks (FPIX), with sensors which are different from each other and produced by different
 490 foundries. The sensors have an area equal to 100 μm by 150 μm and have been produced
 491 on 285 μm to 300 μm thick wafers.

492 The time resolution is 25 ns, and the information coming from the detector are stored on
 493 chip for the Level-1 trigger latency ($\sim 4 \mu\text{s}$). The upgrade baseline ROIC was redesigned for
 494 the outer 3 layers, replacing analog signal readout with on-chip ADCs and digital readout
 495 at higher rate. reads out the pulse height information for each pixel.

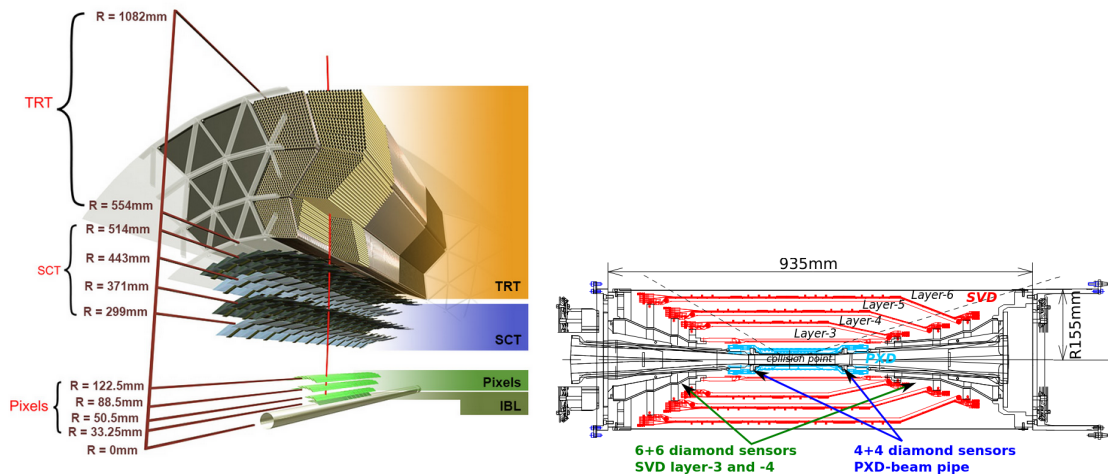


Figure 3.1: (a), (b) Since an accidental beam background enhancement can damage the VXD, diamond detectors are installed in order to monitor it.

¹Run 3 start in June 2022

496 **LHCb**

497 LHCb is a dedicated heavy-flavour physics experiment that exploits pp interactions at
498 14 TeV at LHC. It was the last experiment to upgrade the vertex detector, the Vertex
499 Locator (VELO), replacing the silicon-strip with 26 plane pixel detector (beacause of the
500 fixed target geometry) in May 2022. As the instantaneous luminosity in Run3 is increased
501 by a factor $\lesssim 10$, much of the readout electronics and of the trigger system have been
502 developed in order to cope with the large interaction rate. To place the detector as close as
503 possible to the beampipe and reach a better track reconstruction efficiency and resolution,
504 the VELO has a surprising feature: during the injection of LHC protons it is parket at
505 3 cm from the beams and only when the stability is reach it is moved at ~ 5 mm. Readout
506 speed is a priority for the detector that use a triggerless readout at 40 MHz collision rate,
507 producing 20 Gbps per ROIC. The Velopix, which is the hybrid system designed for LHCb,
508 is made bonding sensors, each measuring 55×55 micrometers, 200 μm -thick to a 200 μm -
509 thick ASIC specially developed for LHCb and coming from the Medipix family (sec. ??),
510 which can handles hit rates up to 900 MHz per chip. Since the detector is operated under
511 vacuum near the beam pipe, the heat removal is particularly difficult and evaporative CO₂
512 microchannel cooling are used.

513 **BelleII**

514 Due to the high background level coming from the nanobeam used at SuperKEKB in order
515 to achieve a such high luminosity ($4.7 \times 10^{34} \text{1/cm}^2/\text{s}$), silicon strip cannot be used in the
516 inner layer of the tracker. The occupancy is too high to allow the usage of strips up to
517 40 mm from the beam pipe. Moreover for a precise reconstruction of B-decay vertices, the
518 usage of thin detector is mandatory at the low energy (4 GeV to 7 GeV) of the beam, in
519 order to minimize the multiple scattering of particles.

520 The current vertex detector of BelleII, VXD, is made of a pixel detector (PXD), fab-
521 ricated with 2 layers of DEPFET-based pixels, and 4 layers of a double-sided silicon strip
522 detectors (SVD)[5]. Due to the small capacitance of the collection node, DEPFET presents
523 a high signal-to-noise ratio (in 30-50) thanks to the low instrinsic noise and to the large
524 signal achieved with he fully depleted bulk: pixels are thinned to 75 μm in the active
525 region, then a MIP is supposed to create a signal of $\sim 6000 e^-$, while the typical noise of
526 DEPFET is around 200 e^- . The ASIC read out is still based on a rolling shutter logic,
527 with an integration time of 20 μs . In order to reduce the data-storage memory PXD hits
528 are only used to improve spatial resolution of tracks: the SVD informations are used by
529 the High Level Trigger (HLT) to look for regions of interest in the pixel ladders just by
530 extrapolating back the tracks found in the tracker detector, and this method allows to
531 store only data belonging to these areas; the PXD hits are then used in offline track fit to
532 improve the vertex resolution.

533 MAPS have been proposed for the replacement of VXD during the Long Shut Down
534 2 (LSD2) foreseen around 2026-27; the new vertex detector, VTX, should be made of 5
535 layers fabricated by the optimized Belle II pixel sensor (OBELIX), a detector based on
536 TJ-Monopix have been selected (look at chapter ??). The main advantages VTX should
537 bring are a obvious improving in the track and vertex resolution (14 μm before upgrade,
538 $\lesssim 10 \mu\text{m}$ expected after upgrade) and a reduction in the X_0 (da.. a..), a higher background
539 tolerance because of the smaller sensor than strips dimension and a low bandwidth due to
540 the on-chip sparsification.

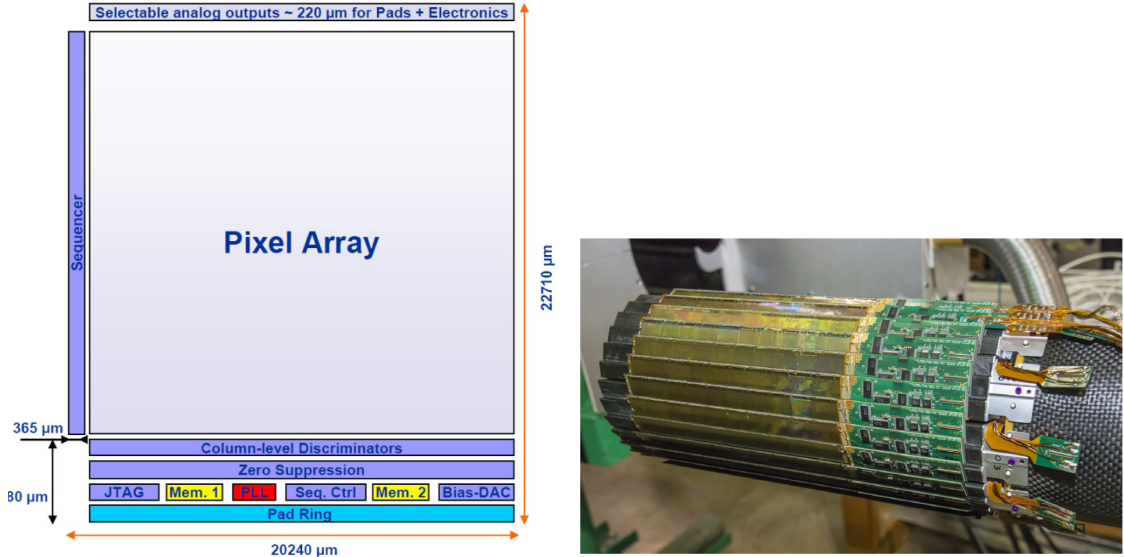


Figure 3.2: (a) The HFT PXL detector; (b) Block-diagram of the ULTIMATE-2 sensor

541 3.1.2 First attempts to MAPS

542 MIMOSA at EUDET and STAR

543 MIMOSA [6][7] (standing for Minimum Ionizing MOS Active pixel sensor), designed in
 544 2008, prefigured the architecture of MAPS for coming vertex detector being the first large
 545 scale sensor to be employed as detector. MIMOSA-26 equiped the final version of EUDET
 546 high resolution beam telescope both at CERN-SPS and at DESY while the MIMOSA-
 547 28 devices are used for the first MAPS-based vertex detector at the STAR experiment.
 548 MIMOSA-26 is fabricated in a 350 nm, and a module features 1152 columns, split into
 549 18 indipendent groups, and 576 rows, with square pixels having a side of 18.4 μm lenght;
 550 the epitaxyal layer is not fully depleted and the charge collection is mostly by diffusion,
 551 resulting in charge sharing between pixels and collection time bigger than 100 ns.

552 The readout is done in a rolling shutter mode and it is the first MAPS integrating on
 553 chip the zero supresion: the chip is an Active Pixels (APS) and therefore it incorporates
 554 the amplification on pixel, while the signal discrimination and zero-suppression logic are
 555 placed at the EoC, where is also placed a memory. The chip is an Active Pixels (APS)
 556 and therefore it incorporates the amplification on pixel, while the signal discrimination
 557 and zero-suppression logic are placed at the EoC: the readout is done in a rolling shutter
 558 mode with a frame integration time that can be lowered down to 85 ms, and a memory
 559 allowing to store up to six hits is.

560 The EUDET telescope, equipped with six sensor planes, requires highly granular and
 561 thin pixel detectors in order to achieve an excellent track resolution (around 2 μm) even at
 562 the rather low particle energies of up to 6 GeV. The STAR experiment at the Relativistic
 563 Heavy Ion Collide (RHIC) accelerator at the Brookhaven National Laboratory (BNL) is
 564 the first to include MAPS in the vertex detector[8]. The main tracking detector in STAR is
 565 a TPC with radii 60-190 cm embedded in a 0.5 T solenoidal magnetic field, that provides
 566 a pointing resolution of approximately 1 mm. The pixel detector, PXL, is a part of a
 567 3-detector system, Heavy Flavor Tracker (HFT), that has been added to the pre-existing
 568 STAR apparatus just before the 2014 Run in order to improve the impact parameter

resolution and to enable the direct reconstruction of hadronic decays of heavy flavor mesons and baryons. The Heavy Flavor Tracker (HFT) is composed by the Silicon Strip Detector (SSD), the Intermediate Silicon Tracker (IST) and the Pixel Detector (PXL); the first one is placed at 22 cm from the beam pipe and consists of double sided strips with 95 μm inter-strip pitch, the second one, placed at 14 cm, is made of single sided silicon pads with 600 $\mu\text{m} \times 6$ mm pitch and the last one made by two layers is placed at 2.8 cm and 8 cm fabricated with ULTIMATE2 (also known as MIMOSA-28), a successor of MIMOSA-26 sensor, with pitch 20.7 μm and thinned down to 50 μm . An area of 0.16 m^2 are covered by 400 MAPS sensor, corresponding to 356 millions of pixels divided into array size of 928 \times 960. Each pixel includes circuitry for readout, amplification, and Correlated Double Sampling (CDS) for signal extraction and noise subtraction and the frame integration time is 185.6 μs ; after the subtraction the signal to noise ratio is ~ 30 , with a noise between 10-12 electrons and a signal of 1000 e^- . Thanks to the HFT system and the PXL, STAR achieved a track pointing resolution 46 μm for 750 MeV/c kaons, and better than 30 μm for particle momenta bigger than 1 GeV/c: this performance enabled the study of D-meson production with a high significance signal.

585 ALPIDE at ALICE

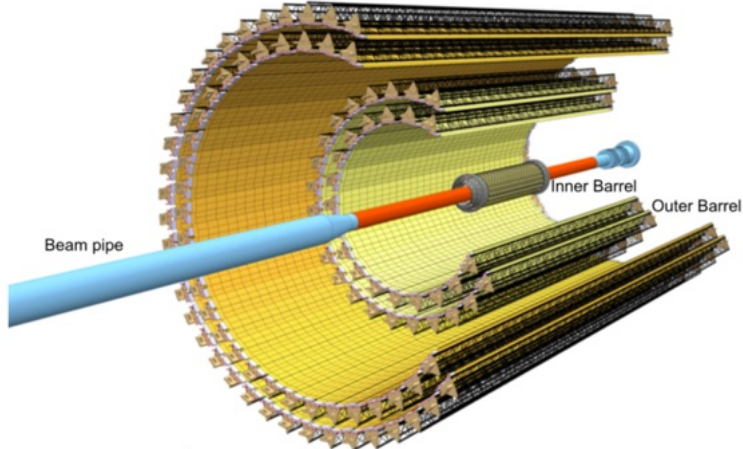


Figure 3.3

586 ALICE (A Large Ion Collider Experiment) is a detector dedicated to heavy-ion physics
 587 at the LHC. The tracking detector consists of the Inner Tracking System (ITS), the gaseous
 588 Time Projection Chamber (TPC) and the Transition Radiation Detector (TRD), and all
 589 those are embedded in a magnetic field of 0.5 T. The ITS is made by six layers of detectors,
 590 two for each type, from the interaction point outwards: Silicon Pixel Detector (SPD),
 591 Silicon Drift Detector (SDD) and Silicon Strip Detector (SSD). Contrary to the others
 592 LHC experiments, ALICE tracker is placed in a quite different environments: the expected
 593 dose is smaller by two order of magnitude and the rate of interactions is few MHz instead
 594 of 40 MHz, but the number of particles comes out of each interaction is higher (the SPS is
 595 invested by a density of particles of $\sim 100 \text{ cm}^{-2}$). The reconstruction of very complicated
 596 events with a large number of particles is a challenge, hence to segment and to minimize
 597 the amount of material, which may cause secondary interaction complicating further the
 598 event topology, is considered a viable strategy.

599 ITS2, upgraded during the LHC long shut down in 2019-20, was the first large-area
600 ($\sim 10 \text{ m}^2$ covered by 2.5 Gpixels) silicon vertex detector based on CMOS MAPS. The
601 detector employes the ALPIDE chip, developed by ALICE collaboration, fabricated in the
602 180 nm CMOS Imaging Sensor process of TowerJazz, whose design takes full advantage
603 of process feature which allows full circuitry within the pixel matrix. Thanks to the
604 reduction of the material budget, ITS2 obtained an amazing improvement both in the
605 position measurement and in the momentum resolution, improving the efficiency of track
606 reconstruction for particle with very low transverse momentum (by a factor 6 at $pT \sim$
607 0.1 GeV/c). Further advancements in CMOS MAPS technology are being aggressively
608 pursued for the ALICE ITS3 vertex detector upgrades (foreseen around 2026-27), with
609 the goals of further reducing the sensor thickness and improving the readout speed (which
610 now is completely asynchronous) of the devices, while keeping power consumption at a
611 minimum.

612 3.2 Other applications

613 Historically for imaging purpose the CCDs were the favoured device: they can be used as
614 single photon counter or integrating and collecting the charge released by more impinging
615 particles. The utilisation in the first case is similar to the tracking one, except that the
616 requirements are less tight, so much that two noteworthy of microchips originally meant
617 for detectors in particle physics at the LHC, and later employed in other fields are Medipix
618 and Timepix. They are read-out chips developed by the Medipix Collaborations since early
619 1990s. For two decades, different Medipix generations have been produced, having a rough
620 correlation with the feature size used: Medipix2 (1999) used 250 nm feature size CMOS
621 while Medipix3 (2005) 130 nm. For photons imaging other materials with higher atomic
622 charge than silicon could be prefered, as a high photon absorption efficiency is needed: it
623 was for this reason that Medipix2 was bump bonded to identically segmented sensors of
624 both silicon and GaAs.

625 The applications in scientific imaging vary from astrophysics and medical imaging and
626 dosimetry to more exotic domains as studies of protein dynamics, material science, art
627 authentication and archaeology. One of the most important employment of Medipix is as
628 X-ray single photon counting in industrial and medical radiography and in 3D computed
629 tomography². Thanks to a New-Zealand company, the MARS Bioimaging detector has
630 been fabricated, which is capable of resolving the photons energy and produce 3D coloured
631 images. Besides tracking in HEP (I have already cited the use of Timepix3 is in the beam
632 telescope of the LHCb VELO), an important use of Timepix is in dosimetry. **Timepix**
633 **Detector for Imaging in Ion Beam Radiotherapy- articolo e qualche info.** A small-Timepix
634 detector with the dimension of a USB can also be found at the International Space Station,
635 where it is exploited for radiation, principally made of heavy-ion, monitoring.

636 3.2.1 Applicability to FLASH radiotherapy

637 A possible new application of pixels detector is dosimetry or beam monitoring of charge
638 particles in high intensity radiography. Recently³ a promising method for RT at ultra high

²The analysis of the direction dependence of X-ray absorption is performed, for example, in order to obtain an image in Computed Tomography (CT)

³The first evidences have been observed on mice experiments in 1966 and in 2014 by the group of Favaudon and Vozenin. After this, many tests on cats and pigs have been performed, and also there has

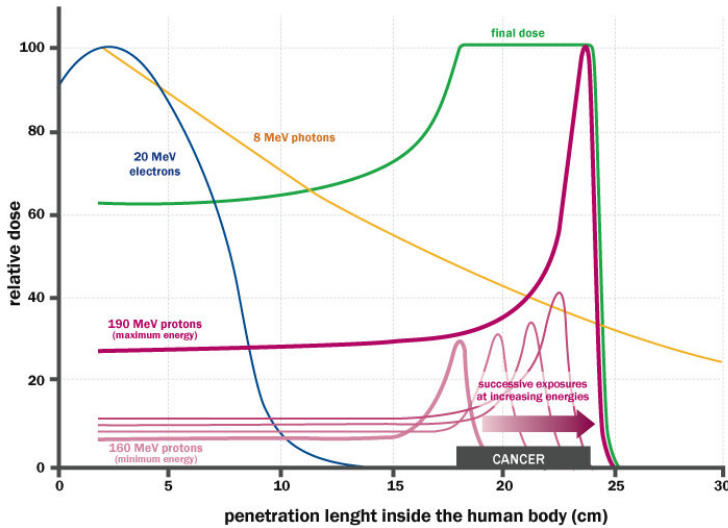


Figure 3.4: The Spread Out Bragg Peak (SOBP) curve (green), which is a constant dose distribution, is obtained from the superposition of many Bragg peak of hadrons with different energy.

639 dose rate (at least 40 Gy/s) and for this reason called FLASH-RT[9], instead of CONV-RT
 640 (0.03 Gy/s), came out. However, finding dosimeters suitable at ultra high dose rate is still
 641 an open issue since almost all standard online dosimeters have shown saturation problems.

642 Radiotherapy

643 The radiological treatment is a common method used in 60% of tumors both as palliative
 644 care and as treatment. It can be given before, after or during a surgery, (Intra operative
 645 radiation therapy-IORT) and many different types of radiations (photons, electrons,
 646 protons and ions, which mainly are hydrogen and carbon) can be used to irradiate the
 647 affected tissues. Exploiting the ionizing energy loss, that can be parametrized by the
 648 Linear Energy Transfer (LET), a biological damage can be delivered to the tissue: while α
 649 and β particles are high LET radiations with values in $100 \text{ keV}/\mu\text{m}$ to $200 \text{ keV}/\mu\text{m}$, x-rays
 650 and gamma-rays are low LET radiations with values in range $0.2 \text{ keV}/\mu\text{m}$ to $2 \text{ keV}/\mu\text{m}$. If
 651 x-ray photons, with energy in 4 MeV to 25 MeV are used, the ionization is caused by the
 652 Compton electrons and is more in the superficial layers of the tissue due to the exponential
 653 attenuation of the beam. The hadrons energy loss, instead, is strongly localized in
 654 the last region of the track, that is the Bragg peak, such as the the treatment typically
 655 requires the scanning of the target. The Relative Biological Effectiveness (RBE) of ions
 656 near the Bragg peak depends on their mass, and in particular it increases with the ion's
 657 mass; even though, too heavy ions generally increases the damage produced also in the
 658 entrance region. Carbon is considered the optimum between the two trends.

659 Electrons, instead, of energy in range of a dozen of MeV tend to spread out on a
 660 bigger region of a few centimeters in both the diameter and thickness. Using Very High
 661 Energy Electrons (VHEE) has been taken into account for irradiation of deeper tissues,
 662 however, to date, the FLASH effect has been tested and demonstrated only using low-energy

been a clinical trial on a cutaneous tumor-patient

	CONV-RT	FLASH-RT
Dose rate	0.03 Gy/s	40 Gy/s
Intra pulse dose rate	100 Gy/s	106 Gy/s
Treatment duration	~minutes	$\lesssim 500$ ms
Dose Per Pulse	0.3 mGy	1 Gy to 10 Gy
Pulse width	3 μ s	$\sim 2 \mu$ s

Table 3.1: Typical value of treatment parameters

663 electrons.

664 FLASH effect

665 This treatment takes advantages of biological differences between tumors and healthy
 666 tissues: it is characterized by reducing normal tissue toxicity and maintaining equivalent
 667 tumor damage. The response to dose can be described by the survival fraction probability,
 668 describing the fraction of surviving cell as a function of the dose:

$$S(D) = S(0) e^{-(\alpha D + \beta D^2)} \quad (3.1)$$

669 where α and β respectively represents the rate of cell killing by single ionizing events and
 670 by double hits. Hence, at high doses the density of damages increases and the cells repair
 671 becomes more difficult. Even if the FLASH effect is not yet completely understood and
 672 the underlying mechanisms are not clear, it looks like there are two different recipes which
 673 are involved:

- 674 • **The dose rate:** higher dose rate produce bigger damages (fig. 3.5(a)) since this
 675 prevent cells from sparing.
- 676 • **The presence or absence of oxygen:** while hypoxic cells are very resistant to radi-
 677 ation, normal oxygenated cells are highly radiosensitive. This is because if molecules
 678 containing O_2 break due to the impinging radiation, then the oxygen can build Re-
 679 active Oxygen Species (ROS) (fig.3.5(b))

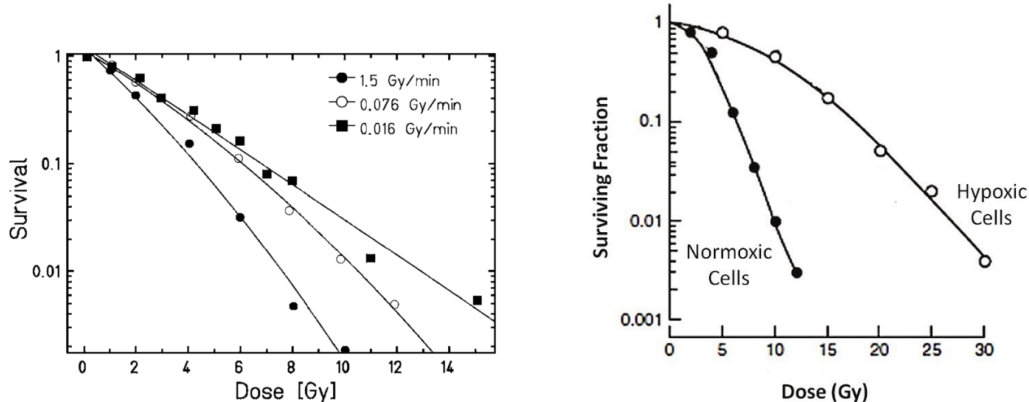


Figure 3.5: (a) Survival curve for different dose rate and (b) for different oxygen cell content

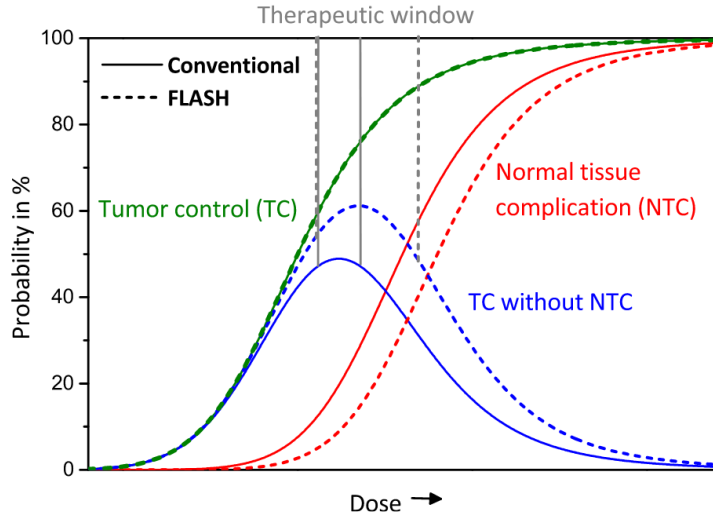


Figure 3.6: Illustration of dependence of TCP, NTCP and therapeutic window on dose, for CONV-RT ad FLASH-RT.

680 The Tumor Control Probability (TCP) and the Normal Tissue Complication (NTC) functions
 681 parametrize respectively the efficiency of damaging on the tumor after having released
 682 a certain dose and the probability of not affecting the healthy tissues. The intermediate
 683 zone between the increase of the TC and of the NTC is called therapeutic window, and
 684 the wider it is and the more effective the treatment is.

685 Dosimetric problems

686 Up to now, all online dosimeters have shown saturation problems at high DDP, differently
 687 from radiochromic films, which are the standard passive dosimeters and have shown a
 688 dose-rate independence up to 109 Gy/s. Even though the linear response in wide dynamic
 689 range, they do not provide any online dosimetric informations, since the time required to
 690 extract the physical value from the reading is not instantaneous⁴.

691 Ionization Chambers (ICs), which are the online reference dosimeter also according to
 692 law, at high level of radiation (already at dose per pulse two orders of magnitude lower
 693 than the ones used for FLASH-RT) show both problems of saturation and recombination.
 694 When a high density of ions and electrons is produced in the gas, a high counter electric
 695 field opposed to the drift one might be generated; if a neutral region build up, both the
 696 recombination of i/e pairs, with a subsequent photoemission and abrupt discharge can
 697 happen⁵. For low level of radiation a correction factors, k_{sat} , can be introduced and a
 698 dose measurement can still be done: with Dose Per Pulse (DDP) lower than 1 mGy the
 699 correction factor is <5%. Non sono sicurissima di aver capito davvero il punto per quanto
 700 riguarda i semiconduttori e gli scintillatori

701 In reference [10] are presented some results related with saturation problems at high
 702 DDP of different types of detectors. The dosimeters tested and their value at which satura-
 703 tion becomes are reported in table 3.2, while in figure 3.7 are reported the measurements.
 704 The DrR is then defined as the ratio between the signal response of each dosimeters at a

⁴COSA sono e più o meno come funzionano

⁵This is called Raether-Meek condition

Commercial detector	Detector type	saturation [Gy/p]
PTW TW34045 Advanced Markus EC	ionization chamber	0.3
PTW TM60017 Dosimetry Diode E	silicon diode	0.15
PTW TW60019 microDiamond	diamond	0.15
DoseVue DoseWireTM Series 100	scintillator fiber	11-26

Table 3.2: Results obtain in [10]

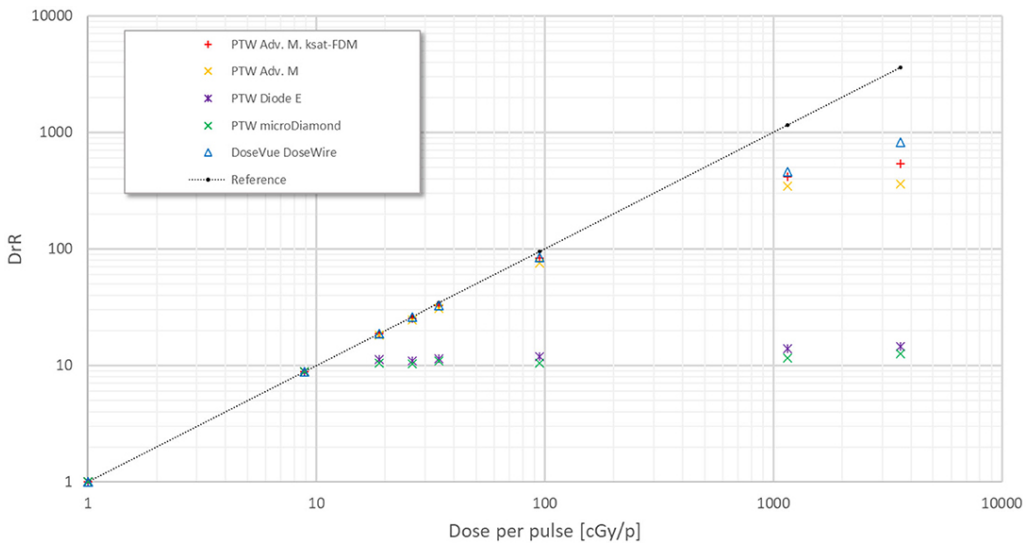


Figure 3.7: Saturation problems underlyed in [10].

705 fixed DDP of 1 cGy/p and is called dosimeter reading ratio (DrR):

$$DrR = \frac{R}{R|_{Dp=1cGy/p}} = \frac{R}{R_{ref}} \quad (3.2)$$

706 Then, for a saturation not affected by saturation problems DrR should be a straight line
 707 with a slope equal to 1; since the reference measurements of dose has been performed with
 708 radiochromic films (GAFCHROMIC EBT-XD), whose dose indipendence has been tested⁶
 709 in range from 0 Gy to 15 Gy, the dotted black line in figure 3.7 represents the reference
 710 measurement done with it.

711 Besides the linearity of the response, two other important requirements for beam mon-
 712 itoring in radiotherapy are both high temporal and space resolutions. Concerning time
 713 resolution I recall that MAPS could handle with rate up to hundreds of MHz, so the pos-
 714 sibility application of these detectors probably strictly depends on their particular usage.
 715 However MAPS might be well suited given that their spatial resolution and their thinness
 716 (they can be thinned down to about 50 μm), which is an obvious requirement for beam
 717 monitor.

⁶The radiochromic films calibration has been obtained by irradiating the films with dose values in range from 0 Gy to 15 Gy, by positioning the films in a polymethylmethacrylate (PMMA) phantom at R₁₀₀ depth, corresponding to 10 cm

⁷¹⁸ **Chapter 4**

⁷¹⁹ **TJ-Monopix1**

⁷²⁰ TJ-Monopix1 is a small electrode DMAPS with fast R/O capability, fabricated by Tow-
⁷²¹ erJazz foundry in 180 nm CMOS imaging process. It is part, together with prototypes
⁷²² from other series such as TJ-MALTA, of the ongoing R&D efforts aimed at developing
⁷²³ DMAPS in commercial CMOS processes, that could cope with the requirements at ac-
⁷²⁴ celerator experiments. Both TJ-Monopix and TJ-MALTA series [11], produced with the
⁷²⁵ same technology by TowerJazz (the timeline of the foundry products is shown in figure
⁷²⁶ 4.1), are small electrode demonstrators and principally differ in the readout design: while
⁷²⁷ Monopix implements a column-drain R/O, an asynchronous R/O without any distribution
⁷²⁸ of BCID has been used by TJ-Malta in order to reduce power consumption.



Figure 4.1: Timeline in TowerJazz productions in 180 nm CMOS imaging process

⁷²⁹ Another Monopix series, but in 150 nm CMOS technology, has been produced by
⁷³⁰ LFoundry [12]. The main differences between the LF-Monopix1 and the TJ-Monopix1
⁷³¹ (summarized in table 4.2), lay in the sensor rather than in the readout architecture, as
⁷³² both chips implements a fast column drain R/O with ToT capability [13][14]. Concerning
⁷³³ the sensors, either are based on a p-type substrate, but with slightly different resistivities;
⁷³⁴ in addition LFoundry pixels are larger, thicker and have a large fill factor (the very deep n-
⁷³⁵ well covers ~55% of the pixel area). The primary consequence is that LF-Monopix1 pixels
⁷³⁶ have a higher capacity resulting in higher consumption and noise. As I discussed in section
⁷³⁷ 2.4.1, the fact that LF-Monopix has a large fill factor electrode is expected to improve its
⁷³⁸ radiation hardness. Indeed, a comparison of the performance of the two chips showed that
⁷³⁹ TJ-Monopix suffers a comparatively larger degradation of efficiency after irradiation, due
⁷⁴⁰ to the low electric field in the pixel corner; on the other hand, a drawback of the large fill
⁷⁴¹ factor in LF-Monopix is a significant cross-talk.

	LF-Monopix1	TJ-Monopix1
Resistivity	$>2 \text{ k}\Omega\text{cm}$	$>1 \text{ k}\Omega\text{cm}$
Pixel size	$50 \times 250 \mu\text{m}^2$	$36 \times 40 \mu\text{m}^2$
Depth	$100\text{-}750 \mu\text{m}$	$25 \mu\text{m}$
Capacity	$\sim 400 \text{ fF}$	$\sim 3 \text{ fF}$
Preamplifier	charge	voltage
Threshold trimming	on pixel (4-bit DAC)	global threshold
ToT	8 bits	6 bits
Consumption	$\sim 300 \text{ mW/cm}^2$	$\sim 120 \text{ mW/cm}^2$
Threshold	$1500 e^-$	$\sim 270 e^-$
ENC	$100 e^-$	$\sim 30 e^-$

Table 4.1: Main characteristics of Monopix1 produced by TowerJazz and LFoundry [13][14]

742 The TJ-Monopix1 chip contains, apart from the pixels matrix, all the required support
 743 blocks used for configuration and testing:

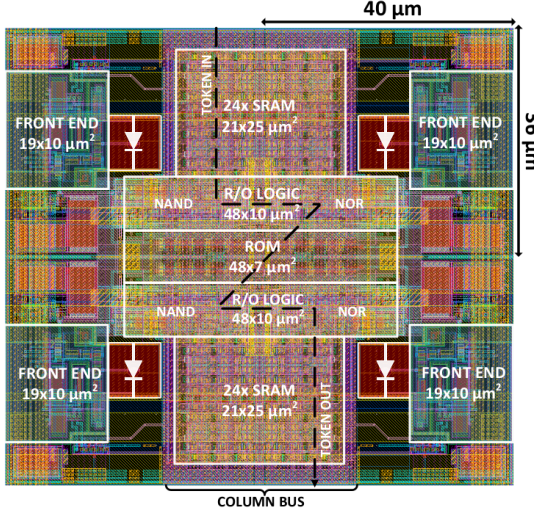
- 744 • the whole matrix contains 224×448 pixels, yielding a total active area approximately
 745 equal to 145 mm^2 over a total area of $1 \times 2 \text{ cm}^2$;
- 746 • at the chip periphery are placed some 7-bit Digital to Analog Converter (DAC), used
 747 to generate the analog bias voltage and current levels and to configuire the FE;
- 748 • at the EoC is placed a serializer to transferred datas immediately, indeed no trigger
 749 memory is implemented in this prototypes;
- 750 • the matrix power pads are distributed at the sides
- 751 • four pixels which have analog output and which can be monitored with an oscillo-
 752 scope, and therefore used for testing

753 Pixels are grouped in 2×2 cores (fig. 4.2a): this layout allows to separate the analog
 754 and the digital electronics area in order to reduce the possible interference between the
 755 two parts. In addition it semplifies the routing of data as pixels on double column share
 756 the same column-bus to EoC. Therefore pixels can be addressed through the physical
 757 column/row or through the logical column/row, as shown in fig. 4.2b: in figure is also
 758 highlighted the token propagaion path, whose I will discuss later.

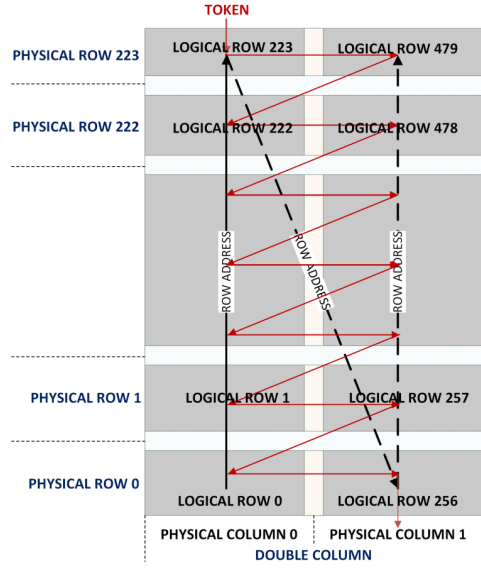
759 Concerning the integration7.7 of the chip in a readout path, TJ-Monopix1 chips have
 760 been wire-bonded on a dedicated carrier board , the Printed Circuit Board (PCB). Two
 761 other board between the DAQ and the chip: the General Purpose Analog Card (GPAC),
 762 which provides power supply channels, current/voltage bias sources and I/O buffer, and
 763 the MIO3 FPGA, which strictly interacts with the DAQ.

764 4.1 The sensor

765 As already anticipated, TJ-Monopix1 has a p-type epitaxial layer and a n doped small
 766 collection electrode ($2 \mu\text{m}$ in diameter); to avoid the n-wells housing the PMOS transistors
 767 competing for the charge collection, a deep p-well substrate, common to all the pixel FE



(a) Layout of a core containing 4 pixels. The analog FE and the digital part are separated in order to reduce cross-talk be



(b)

Parameter	Value
Matrix size	$1 \times 2 \text{ cm}^2$
Pixel size	$36 \times 40 \mu\text{m}^2$
Depth	$25 \mu\text{m}$
Electrode size	$2 \mu\text{m}$
BCID	40 MHz
ToT-bit	6
Power consumption	$\sim 120 \text{ mW/cm}^2$

Table 4.2

area, is used. TJ-Monopix1 adopts the modification described in section 2.4.2 that allows to achieve a planar depletion region near the electrode applying a relatively small reverse bias voltage. This modification improves the efficiency of the detector, especially after irradiation, however a simulation of the electric field in the sensor, made with the software TCAD (Technology Computer Aided Design), shows that a nonuniform field is still produced in the lateral regions of the pixel compromising the efficiency at the corner. Two variations to the process have been proposed in order to further enhance the transversal component of electric field at the pixel borders: on a sample of chip, which includes the one in Pisa, a portion of low dose implant has been removed, creating a step discontinuity in the deep p-well corner (fig. 4.3); the second solution proposed[MOUSTAKAS THESY, PAG 58] consists in adding an extra deep p-well near the pixel edge. A side effect of the alteration in the low dose implant is that the separation between the deep p-well and the p-substrate becomes weak to the point that they cannot be biased separately to prevent the punchthrough.

Moreover, to investigate the charge collection properties, pixels within the matrix are split between bottom top half and bottom half and feature a variation in the coverage of the deep p-well: the electronics area can be fully covered or not. In particular the pixels

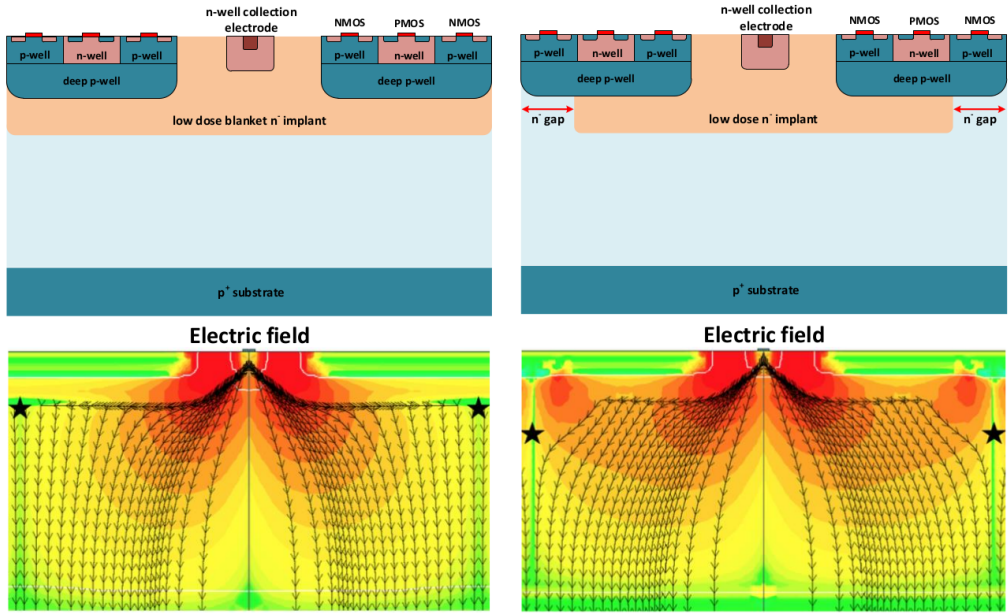


Figure 4.3: (a) The cross-section of a monolithic pixel in the TJ-Monopix with modified process; additionally in (b) a gap in the low dose implant is created to improve the collection of charge due to a bigger lateral component of the electric field. this point in figure is indicated by a star . transversal component of the electric field drops at the pixel corner

785 belonging to rows from 0 to 111 are fully covered (FDPW) and pixels belonging to rows
 786 from 112 to 223 have a reduced p-well (RDPW), resulting in a enhancement of the lateral
 787 component of the electric field.

788 4.2 Front end

789 One of the main advantage of this chip is the small collection electrode, which results in a
 790 small capacitance ($C_{in}=3\text{ fF}$) allowing for high input signal amplitude and single stage of
 791 amplification, which obviously improves the signal to noise ratio performance of the FE.
 792 Assuming a fully depleted epitaxial layer of $25\text{ }\mu\text{m}$, which corresponds approximately to
 793 a $20\text{ }\mu\text{m}$ of deep sensing volume, a MIP should produce $\sim 1600\text{ e}^-$, then:

$$V_{in} = \frac{1600\text{ e}^- \times 1.6 \cdot 10^{-19}\text{ C}}{3\text{ fF}} = 85\text{ mV} \quad (4.1)$$

794 Secondly, a reset mechanism which slowly discharges the detector capacitance must be
 795 included in the circuit:

$$V_{in} = \frac{Q_s}{C_{in}} e^{-t/R_b C_{in}} \quad (4.2)$$

796 where R_b is the equivalent reset element. The general constraint which must be satisfied
 797 is that the discharge time $\tau = R_b C_{in}$ must be slower than the characteristic time of
 798 the amplifier, otherwise a signal loss could occurs. Traditionally the reset can be
 799 implemented in two different way: with a forward biased diode, that might be implemented
 800 by a simple p+ diffusion inside the well of the collection electrode n, or with a PMOS
 801 transistor. Despite of the semplicity of the diode reset, since it is a non-linear element,
 802 the discharge would depend on the quantity of charge Q generated on the n electrode,

803 prejudicing the linearity of the analog output (Q-ToT). To solve the issue, a PMOS reset
 804 is the method preferred in design such TJ-Monopix1 with analog output; the PMOS
 805 transistor, indeed, can acts as a constant current source and then used to discharge the
 806 sensor. Although the PMOS reset is capable of providing a constant current, it has to be
 807 manually re-tuned every time in order to restore the input DC baseline voltage; to do that
 808 a low-frequency feedback is used.

809 The matrix is split in four sections, each one corresponding to a different flavor of the
 810 FE, implemented in order to test more options.

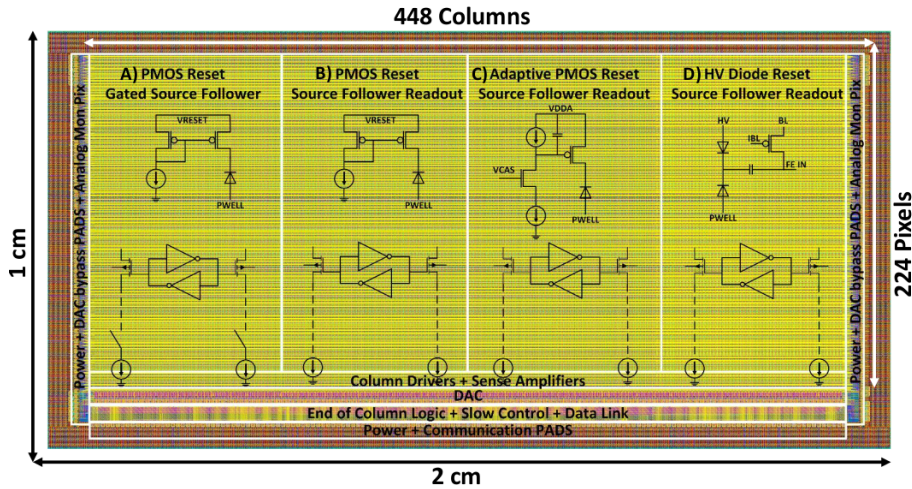


Figure 4.4: TJ-Monopix1 has been developed in four different flavor. The flavor PMOS reset (B) is considered as the reference one.

810
 811 All the flavors implement a source-follower double-column bus readout: the standard
 812 variation is the flavor B, that features a PMOS input reset (refered as "PMOS reset").
 813 Flavor A is identical to flavor B except for the realization of the source follower (it is a
 814 gated one): in the circuit of the gated versione there is a transistor more that operates on
 815 the baseline and on the feedback mechanism; this aim to reduce the power consumption
 816 and results in a higher signal baseline, and then in a lower effective threshold. C instead
 817 implements a novel leakage compensation circuit, with a PMOS reset configuration. More-
 818 over the collection electrode can be either DC-coupled to the readout electronics, as in
 819 flavors A, B, C, or AC-coupled through a metal-oxide-metal (MOM) capacitor, as in D
 820 is AC-coupled. The latter one allows applying a high bias voltage to the electrode n and
 821 for this reason the flavor D is also called "HV flavor". Unfortunately the "HV" suffer
 822 from a signal loss, which can achieve even the 50%, due to the additional parasitic capac-
 823 ity introduced at the input node. The HV voltage above which the breakdown begins is
 824 ~ 50 V; however at values bigger than 20 V, the gain does not increase anymore, since the
 825 depletion zone is already fully depleted.

826 4.2.1 ALPIDE-like

827 ALPIDE chips, developed by the ALICE collaboration, implemented a standard FE to the
 828 point that many CMOS MAPS detectors used a similar FE and are called "ALIPDE-like".
 829 Considering that both TJ-Monopix1 and ARCADIA-MD1 have an ALPIDE-like FE, I am
 830 going to explain the broad principles of the early FE stage. The general idea is of the
 831 amplification to transfer the charge from a bigger capacity[15], C_{source} , to a smaller one,

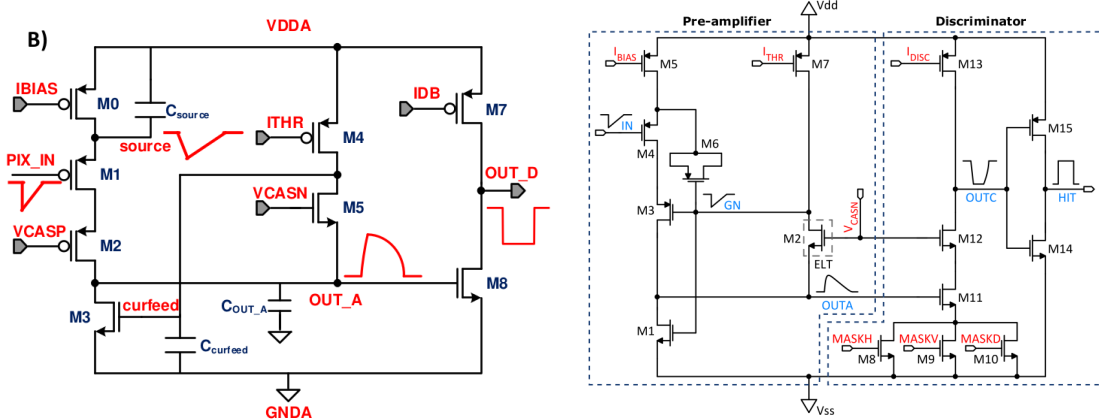


Figure 4.5

⁸³² C_{out} : the input transistor M1 with current source IBIAS acts as a source follower and this
⁸³³ forces the source of M1 to be equal to the gate input $\Delta V_{PIX_IN} = Q_{IN}/C_{IN}$.

$$Q_{source} = C_{source} \Delta V_{PIX_IN} \quad (4.3)$$

The current in M2 and the charge accumulates on C_{out} is fixed by the one on C_{source} :

$$\Delta V_{OUT_A} = \frac{Q_{source}}{C_{OUT_A}} = \frac{C_{source}\Delta V_{PIX_IN}}{C_{OUT_A}} = \frac{C_{Source}}{C_{OUT_A}} \frac{Q_{IN}}{C_{IN}} \quad (4.4)$$

835 A second branch (M4, M5) is used to generate a low frequency feedback, where VCASN
 836 and ITHR set the baseline value of the signal on C_{OUT_A} and the velocity to goes down
 837 to the baseline. **IL RUOLO DI CURVFEED NON L'HO CAPITO.** Finally IDB defines
 838 the charge threshold with which the signal OUT_A must be compared: depending on if
 839 the signal is higher than the threshold or not, the OUT_D is high or low respectively.

The actual circuit implemented in TJ-Monopix1 is shown in figure 4.5: the principal difference lays in the addition of disableing pixels' readout. This possibility is uttermost important in order to reduce the hit rate and to avoid saturating the bandwidth due to the noisy pixels, which typically are those with manufacturing defects. In the circuit transistors M8, M9 and M10 have the function of disabling registers with coordinates MASKH, MASKV and MASKD (respectively vertical, orizontal and diagonal) from readout: if all three transistors-signals are low, the pixel's discriminator is disabled. Compared with a configurable masking register which would allow disableing pixels individually, to use a triple redundancy reduces the sensistivity to SEU but also gives amount of intentionally masked ("ghost") pixels. This approach is suitable only for extremely small number N of pixel has to be masked: if two coordinate projection scheme had been implemented, the number of ghost pixels would have scale with N^2 , if instead three coordinates are used, the N's exponential is lower than 2 (fig. 4.6)

Foto dell'oscilloscopio per far vedere cosa fanno i parametri

854 4.3 Readout logic

TJ-Monopix1 has a triggerless, fast and with ToT capability R/O which is based on a column-drain architecture. On the pixel are located two Random Access Memory (RAM) cells to store the 6-bit LE and 6-bit TE of the pulse, and a Read-Only Memory (ROM)

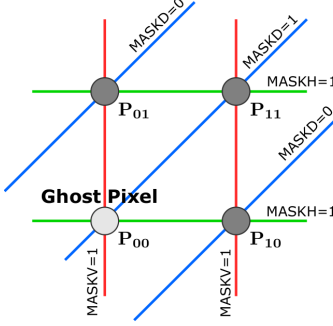


Figure 4.6

Parameter	Meaning	
IBIAS	mainly controls the rise time	yes
IDB	sets the discriminator threshold	yes
ITHR	sets the velocity of the return to the baseline	yes
ICASN	sets the baseline of the signal	yes
VRESET	sets the gain of the preamplifier	yes
IRESET	sets the gain of the preamplifier	no

Table 4.3: FE parameters which must be setted through the DAQ. "Function" means that higher parameter implies higher value

858 containing the 9-bit pixel address. Excluded these memories, TJ-Monopix1 hasn't any
 859 other buffer: if a hit arrives while the pixel is already storing a previous one, the new
 860 data get lost. After being read, the data packet is sent to the EoC periphery of the
 861 matrix, where a serializer transfers it off-chip to an FPGA (4.7). There a FIFO is used
 862 to temporarily stored the data, which is transmitted to a computer through an ethernet
 863 cable in a later time.

864 The access to the pixels' memory and the transmission of the data to the EoC, following
 865 a priority chain, is managed by control signals and is based on a Finite State Machine
 866 (FSM) composed by four state: no-operation (NOP), freeze (FRZ), read (RD) and data
 867 transfer (DTA). The readout sequence (??) starts with the TE of a pulse: the pixel
 868 immediately tries to grab the column-bus turning up a hit flag signal called *token*. The
 869 token is used to control the priority chain and propagates across the column indicating
 870 what pixel that must be read. To start the readout and avoid that the arrival of new hits
 871 disrupt the priority logic, a *freeze* signal is activated, and then a *read* signal controls the
 872 readout and the access to memory. During the freeze, the state of the token for all pixels
 873 on the matrix remains settled: this does not forbid new hits on other pixels from being
 874 recorded, but forbids pixels hit from turning on the token until the freeze is ended. The
 875 freeze stays on until the token covers the whole priority chain and gets the EoC: during
 876 that time new token cannot be turned on, and all hits arrived during a freeze will turn
 877 on their token at the end of the previous freeze. Since the start of the token is used to
 878 assign a timestamp to the hit, the token time has a direct impact on the time resolution
 879 measurement; this could be a problem coping with high hits rate.

880 The analog FE circuit and the pixel control logic are connected by an edge detector
 881 which is used to determine the LE and the TE of the hit pulse(fig. 4.9): when the TE

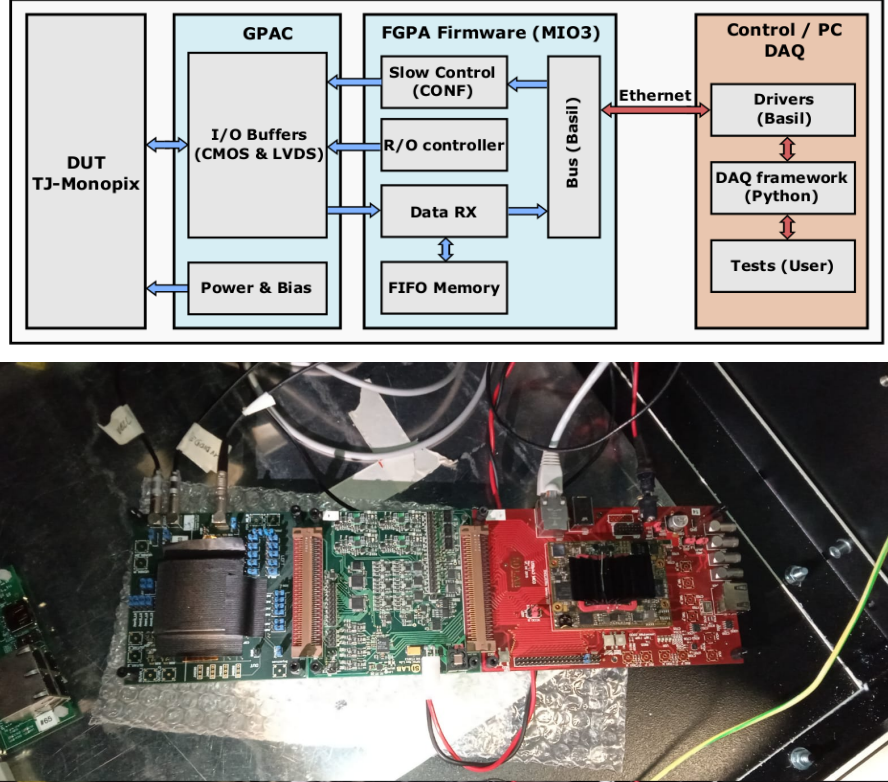
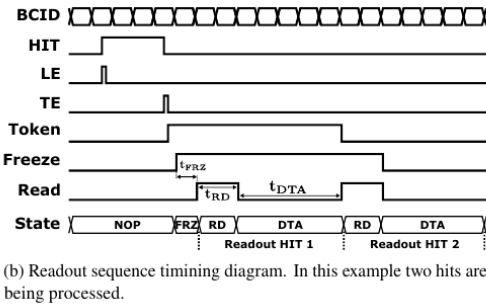


Figure 4.7: Main caption



(b) Readout sequence timing diagram. In this example two hits are being processed.

Figure 4.8: Readout timing diagram: in this example two hits are being processed

is stored in the first latch the edge detector is disabled and, if the **FREEZE** signal is not set yet, the readout starts. At this point the **HIT** flag is set in a second latch and a **Token** signal is produced and depending on the value of **Token** in the pixel can be read or must wait until the **Token in** is off. In figure an OR is used to manage the token propagation, but since a native OR logic port cannot be implemented with CMOS logic, a sum of a NOR and of an inverter is actually used; this construct significantly increases the propagation delay (the timing dispersion along a column of 0.1-0.2 ns) of the token and to speed up the circuit optimized solution are often implemented. When the pixel become the next to be read in the queue, and at the rising edge of the **READ** signal, the state of the pixel is stored in a D-latch and the pixel is allowed to use the data bus; the **TE** and the **HIT** flag latches are reset and a **READINT** signal that enable access of the RAM and ROM cells is produced.

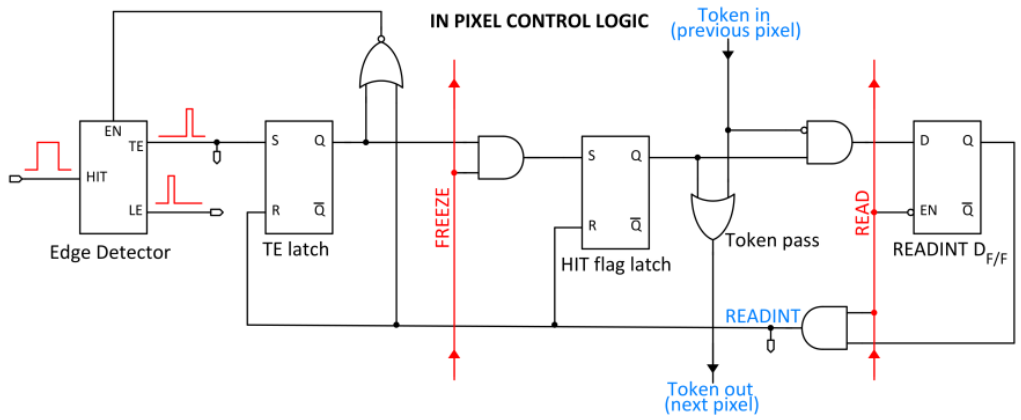


Figure 4.9

894 The final data must provide all the hits' information: the pixel address, the ToT and
 895 the timestamp. All those parts are assigned and appended at different time during the
 896 R/O chain:

- 897 • **Pixel address:** while the double column address (6-bit) is appended by the EoC
 898 circuit, the row address (8-bits for each flavor) and the physical column in the doublet
 899 (1-bit) are assigned by the in-pixel logic
- 900 • **ToT:** is obtained offline from the difference of 6-bits TE and 6-bits LE, stored by
 901 the edge detector in-pixel; since a 40 MHz BCID is distributed across the matrix,
 902 the ToT value is range 0-64 clock cycle which corresponds to 0-1.6 μ s
- 903 • **Timestamp:** The timestamp of the hit correspond to the time when the pixel set
 904 up the token; it is assigned by the FPGA, that uses the LE, TE and a 640 MHz
 905 clock to derive it. For all those hits which arrived while the matrix is frozen, the
 906 timestamp is no more correlated with the time of arrival of the particle

907 When the bits are joined up together the complete hit data packet is 27-bit.

908 **Chapter 5**

909 **Arcadia-MD1**

910 [16] [17]

911 Breve introduzione analoga a Monopix1 in cui descrivo brevemente la "timeline" da
912 SEED Matisse a Md1 e Md2

913 Tutti i minid, siano essi v1 o v2, sono Alpide like. Prima SEED si occupa di stu-
914 diare le prestazioni: concept study with small-scale test structure (SEED), dopo arcadia:
915 technology demonstration with large area sensors Small scale demo SEED(sensor with em-
916 bedded electronic developement) Quanto spazio dato all'elettronica sopra il pwell e quanto
917 al diodo. ..

918 **5.1 The sensor**

919 ARCADIA-MD1 is an LFoundry chip which implements the technology 110 nm CMOS
920 node with six metal layer ??. The standard p-type substrate was replaced with an n-type
921 floating zone material, that is a tecnique to produce purified silicon crystal. (pag 299
922 K.W.).

923 Tra i wafer fabbricati finora ci sono 3 valori di spessore attivo nominale (lo spessore
924 effettivo può variare di qualche micron ripetto a quello nominale): 48um, 100um e 200um.
925 In allegato un'immagine con le cross section.

926 Wafer thinning and backside lithography were necessary to introduce a junction at the
927 bottom surface, used to bias the substrate to full depletion while maintaining a low voltage
928 at the front side.

929 C'è un deep pwell per - priority chain separare l'elettronica dal sensore; per controllare il
930 punchthought è stato aggiunto un n doped epitaxial layer having a resistivity lower than
931 the substrate. It is part of the cathegory of DMAPS Small electrode to enhance the signal

Parameter	Value
Matrix size	$\times \text{ cm}^2$
Pixel size	$25 \times 25 \mu\text{m}^2$
Depth	? μm
Electrode size	$9 \times 9 \mu\text{m}^2$
Power consumption	$\sim \text{mW/cm}^2$

Table 5.1

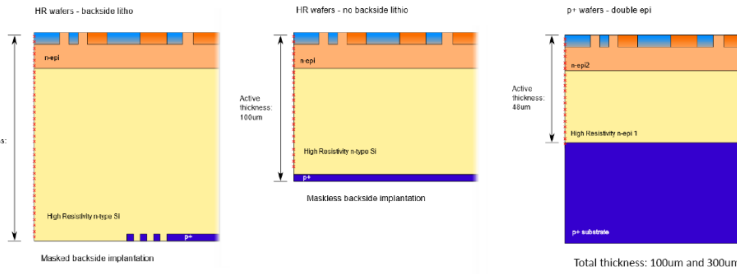


Figure 5.1

to noise ratio. It is operated in full depletion with fast charge collection by drift.

5.1.1 Two different FE flavor

Le differenze tra Alpide e bulk driven sono un po' più complesse di quanto hai scritto. Si tratta proprio di due architetture diverse. Il primo amplifica il segnale attraverso il trasferimento di carica tra due capacità. Nel bulk driven invece il guadagno è dato dal rapporto tra due transconduttanze. Inoltre ci sono altre differenze, il bulk driven è più sensibile alle cadute di tensione sul ground (che ahimè è esattamente ciò che accade nei dimostratori che abbiamo ora, a causa dell'anomalo consumo di corrente dal digitale, altro baco che abbiamo corretto nella terza sottomissione). Anche i livelli di tensione nei nodi interni dei due front-end differiscono e il meccanismo di clipping che funzionava per l'Alpide non è applicabile al bulk driven. Di conseguenza abbiamo un bias in più (ICLIP) nel secondo flavour per controllare il clipping. Nell'Alpide il clipping c'è, ma l'architettura usata permette di non aver bisogno di un bias esterno, anche se in una versione di Alpide di ALICE hanno scelto di controllare comunque la corrente di clip esternamente, per una maggiore flessibilità. Infine alcuni bias che hanno lo stesso nome nei due flavour, perché svolgono la stessa funzione, differiscono nel valore di configurazione didefault.

5.2 Readout logic and data structure

In order to achieve the lowest possible power consumption, the matrix is clockless, no free-running clock, and to save as much area as possible, it will not buffer any hits, and its readout will thus be triggerless.

The Periphery has both an analog part, segmented per Section, and a digital part, which is instead shared. The analog part hosts the bias cells for the AFE dei pixel, mentre la parte digitale che è unica per tutti riprocesso le hit che vengono dalle sezioni e 8b10b encode le parole per data transmission.

5.2.1 Matrix division and data-packets

The matrix is divided into an internal physical and logical hierarchy: The 512 columns are divided in 16 section: 512×32 pixels, each section has different voltage-bias + serializzatori. Each section is devided 512×2 column, and in 32×2 core: in modo che in ogni doppia colonna ci siano 1Pacchetto dei dati 6 cores. ricordati dei serializzatori: sono 16 ma possono essere ridotti ad uno in modalità spazio Ed infine regioni da 4×2 . The readout design must be capable of addressing the following matters Enough bus bandwidth for a

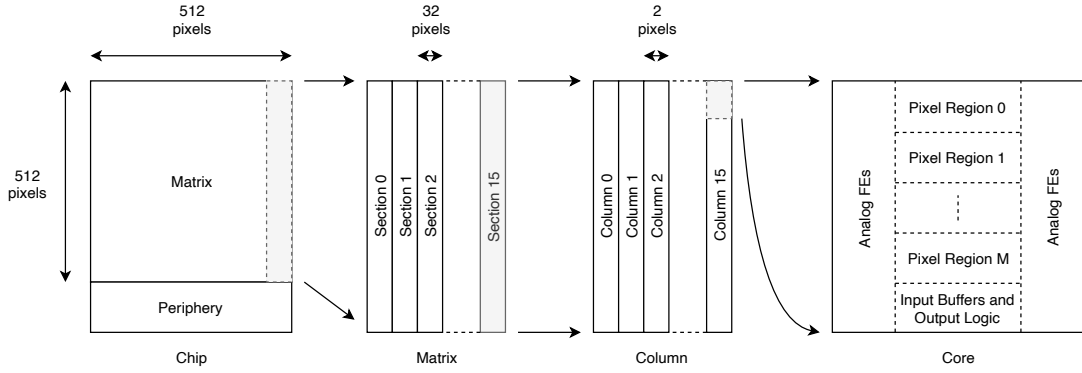


Figure 5.2

hit rate of 100 MHz/cm². Design decisions: Try and send as much data as possible to the periphery (bandwidth) Lowest amount of logic possible (more routability)

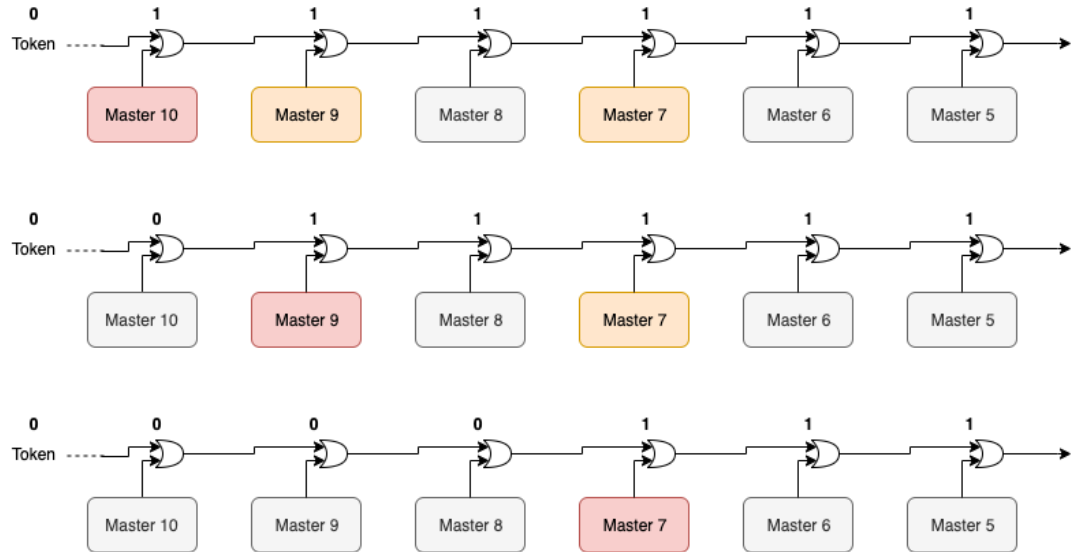


Figure 5.3

Questo divisione si rispecchia in come sono fatti i dati: scrivi da quanti bit un dato è fatto e le varie coordinate che ci si trovano dentro; devi dire che c'è un pixel hot e spieghi dopo a cosa serve, e devi accennare al timestamp

"A core is simply the smallest stepped and repeated instance of digital circuitry. A relatively large core allows one to take full advantage of digital synthesis tools to implement complex functionality in the pixel matrix, sharing resources among many pixels as needed.". pagina 28 della review.

972

973 TABELLA: con la gerarchia del chip Matrix (512x512 pixels) Section (512x32 pixels)
974 Column (512x2) Core (32x2) Region (4x2)

975 Nel chip trovi diverse padframe: cosa c'è nelle padframe e End of section.

976 "DC-balance avoids low frequencies by guaranteeing at least one transition every n
977 bits; for example 8b10b encoding n =5"

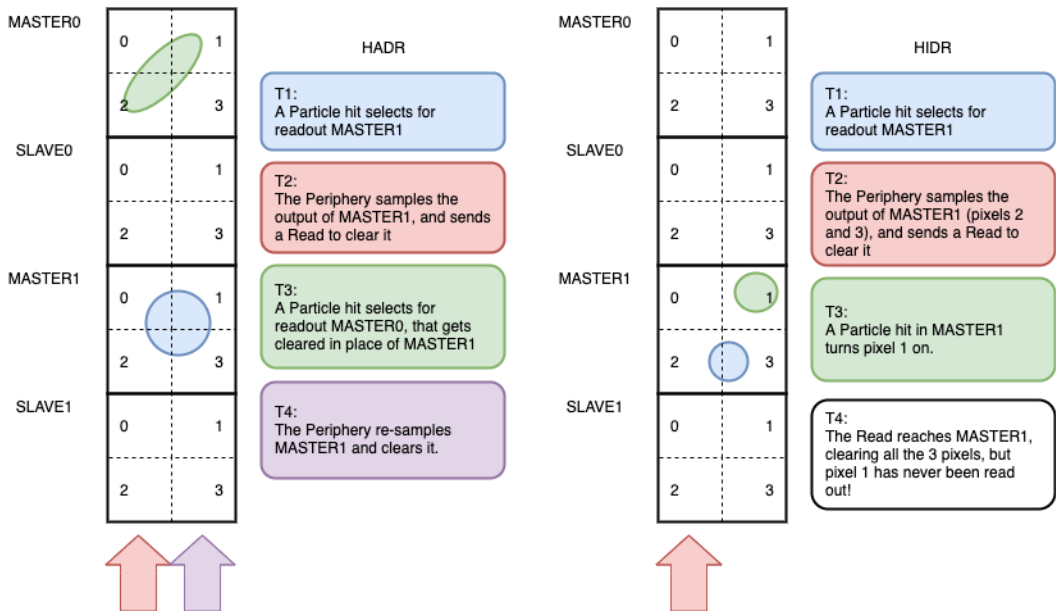


Figure 5.4

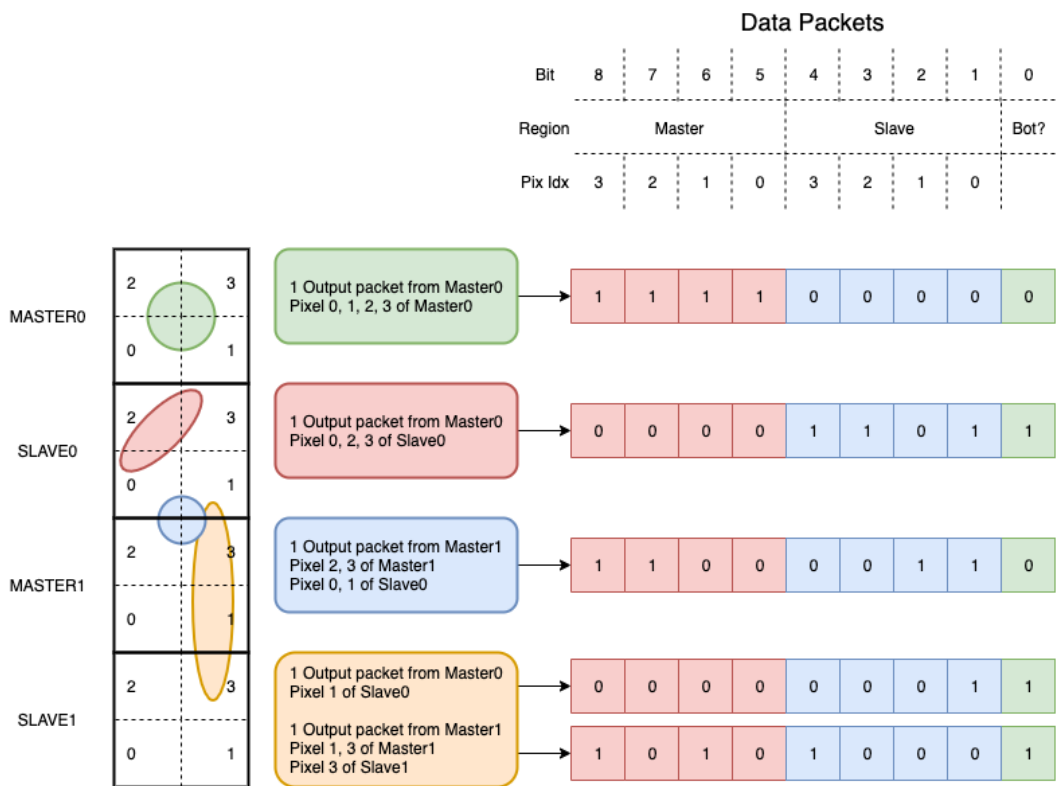


Figure 5.5

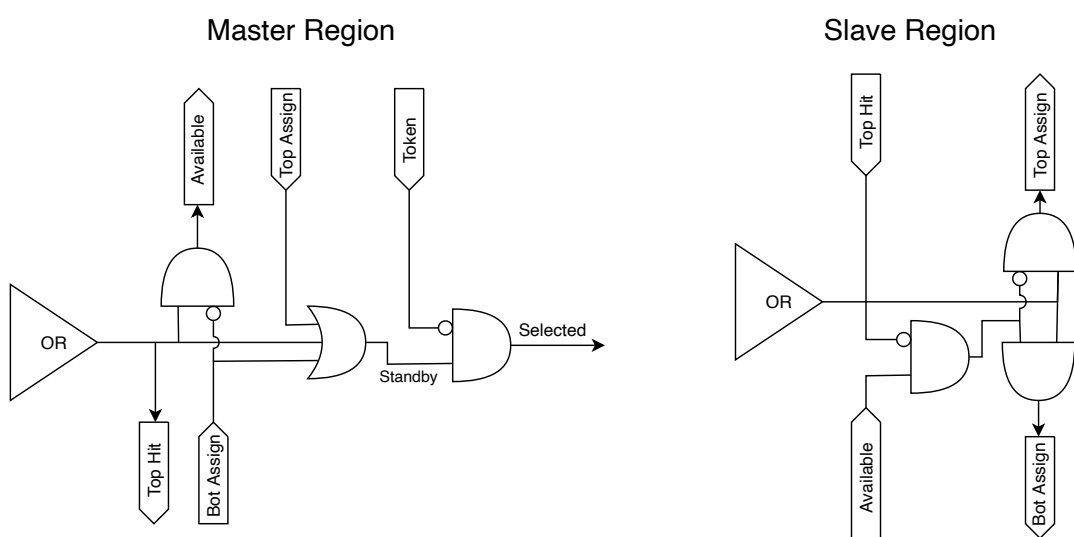


Figure 5.6

978 **Chapter 6**

979 **Characterization**

980

- 981 • rifai il conto della lunghezza di attenuazione. Ho trovato (presentazione Luciano
982 Mus) 29 um per ka e 37 um per kb.
- 983 • Con il PMOS la configurazione del FE di default è: e richiama i significati delle
984 variabili.
- 985 • parla dell HV

986 **6.1 TJ-Monopix1 characterization**

987 **6.1.1 Threshold and noise: figure of merit for pixel detectors**

988 A characterization of threshold and noise is typically necessary since these values have an
989 impact on the operating conditions and on the performance of the chips, so much that
990 the signal to threshold ratio may be considered as the figure of merit for pixel detectors
991 rather than the signal to noise ratio. The mean minimum stable threshold evolved through
992 different generation of chips: in the 1st generation it was around 2500 e^- while in the 3rd
993 (corresponding to nowadays chips) is less than 500 e^- . This allows in thinner sensors with
994 smaller signals: from $16\,000 \text{ e}^-$ produced in $200 \mu\text{m}$, the signal expected moved down to
995 2000 e^- produced in $25 \mu\text{m}$. According with this, the threshold of TJ-Monopix1 is around
996 500 e^- .

997 Obviously the threshold has to be located between the noise peak around the baseline
998 and the signal distribution, in particular it has to be low enough to mantain a high signal
999 efficiency, but also high enough to cut the noise: for a low threshold many pixels can fire
1000 at the same time and a positive feedback can set off a chain reaction eventually, causing
1001 all the other pixels to fire. Thus, the noise sets a lower bound to the threshold: if an
1002 occupancy $\leq 10^{-4}$ is required, for example, this correspond to the Gaussian 1-sided tail
1003 fraction for 3.7σ . In this case, if the noise is 100 e^- (resonable), the threshold must be
1004 higher than $3.7 \times 100 \text{ e}^-$. Typically this argument sets only a minimal bound to the
1005 threshold since the variation with time and from pixel to pixel have to be taken into
1006 account: the temperature, the annealing (for example, the radiation damages in the oxide
1007 layer causes shift of MOSFET threshold voltage) and the process parameters variation
1008 across the wafer (as for example process mismatch between transistors).

Given that the first stage of amplification is the most crucial, since in the following stages the signal amplitude is high compared to additional noise, the noise is valued at the preamplifier input node. Then, the noise is parameterized as Equivalent Noise Charge (ENC), which is defined as the ratio between the noise N at the output expressed in Volt and the out voltage signal S produced by 1 e⁻ entering in the preamplifier:

$$ENC = \frac{N_{out}[V]}{S_{out}[V/e^-]} = \frac{V_{noise}^{RMS}}{G} \quad (6.1)$$

with G expressed in V/e⁻; as the gain increases, the noise reduces . **Servirebbe una misura**
Considering the threshold dispersion a requirement for the ENC is:

$$ENC < \sqrt{(T/3.7)^2 - T_{RMS}^2(x) - T_{RMS}^2(t)} \quad (6.2)$$

where the T is the threshold setted, T_{RMS} is the threshold variation during time (t) and across the matrix (x); a typical reasonable value often chosen is 5 ENC.

Because of the changing of the 'real' threshold, the possibility of changing and adapting the setting parameters of the FE, both in time and in space is desiderable: these parameters are usually set by Digital to Analog Converter (DAC) with a number of bit in a typical range of 3-7. Unfortunately DAC elements require a lot of space that may be not enough on the pixel area; therefore, the FE parameters are typically global, which means that they are assigned for the whole chip, or they can be assigned for regions the matrix is divided into. The former case corresponds to TJ-Monopix1's design in which 7 bits are used for a total 127-DAC possible values, while the latter corresponds to the ARCADIA-MD1's one, **where quanti bit??**. An other possibility, for example implemented in TJ-Monopix2, is allocate the space on each pixel for a subset of bits, then combinig the global threshold with a fine tuning. If so, the threshold dispersion after tuning is expected to be inversely proportional to the tuning DAC number of bits and thus be improved a lot:

$$\sigma_{THR,tuned} = \frac{\sigma_{THR}}{2^{nbit}} \quad (6.3)$$

where σ_{thr} is the RMS of the threshold spread before tuning.

To measure the threshold and noise of pixels a possible way is to make a scan with different known injected charge: the threshold corresponds to the value where the efficiency of the signal exceeds the 50%, and the ENC is determined from the width of this edge. Following this path, I have used the injection circuit available on the chip to inject 100 pulses for each input charge for a fixed threshold. The injection comes on a capacity at the input of the FE circuit, whose mean value is 230 aF and from which the conversion factor from DAC units to electrons can be obtained: for the PMOS flavor, for example, since the DAC are biased at 1.8 V, the Least significant Bit (LSB) corresponds to a voltage of 14.7 mV from which the charge for LSB 1.43 e⁻/mV and the conversion factor therefore is 20.3 e⁻/DAC. While this value is equivalent for all the PMOS flavor, the HV flavor is expected to have a different conversion factor, ~ 33 e⁻/DAC, beacuse of the different input capacity.

Besides the charge, also the duration and the period of the injection pulse can be set; it is important to make the duration short enough to have the falling edge during the dead time of the pixel (in particular during the FREEZE signal) in order to avoid the undershoot, coming at high input charge, triggering the readout and reading spurious hits. Since the injection circuit is coupled in AC to the FE, if the falling edge of the pulse is sharp enought to produce ad undershoot, this can be seen as a signal.

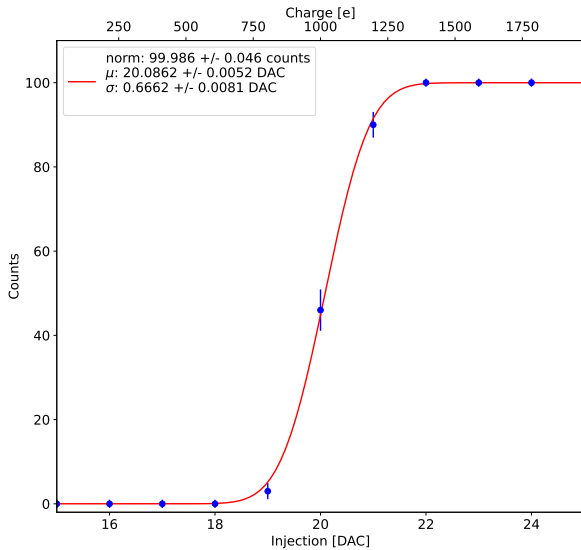


Figure 6.1: S-curve for pixel (10, 10) of the PMOS flavor (flavor 1) with IDB fixed at 40 DAC. The conversion of charge injected from DAC to electrons has been done assuming a conversion factor of 20 e⁻/DAC.

	PMOS A	PMOS B	PMOS C	HV
Threshold [e ⁻]				
Threshold dispersion [e ⁻]				
Noise [e ⁻]				
Noise dispersion [e ⁻]				

Table 6.1: Mean threshold and noise parameters for all flavor and their dispersion on the matrix.

Assuming a gaussian noise, the efficiency of detecting the signal can be described through a modification of the error function:

$$f(x, \mu, \sigma) = \frac{1}{2} \left(1 + \operatorname{erf} \left(\frac{x - \mu}{\sigma\sqrt{2}} \right) \right) \quad (6.4)$$

with: where the threshold and the ENC corresponds to the μ and σ . Therefore I perform a fit of the counts detected using the function in equation 6.4. In figure 6.1 there is an example with IDB equal to 40 DAC of fit for a pixel belonging to the flavor B, while in table ?? and figure ?? there are the histograms and the maps of the parameters of the scurve-fit. As expected, the flavor PMOS reset gated (A), thanks to the transistor which change the baseline value, has a lower threshold and noise

Small threshold variations has been observed in the first biasing section (columns from 0 to 14) with IDB=40 DAC; the same structure appears more evident at other different IDBs, as for example 100 DAC Plot of the average threshold per column al variare di IDB. The systematic threshold variation across the biasing group has not a known motivation, but one could certainly be the transistor mismatch of the biasing DAC registers IDB and ICASN, which both adjust the effective threshold (I recall that ICASN regulate the baseline, and in this measurements it was set to the minimin possible value).

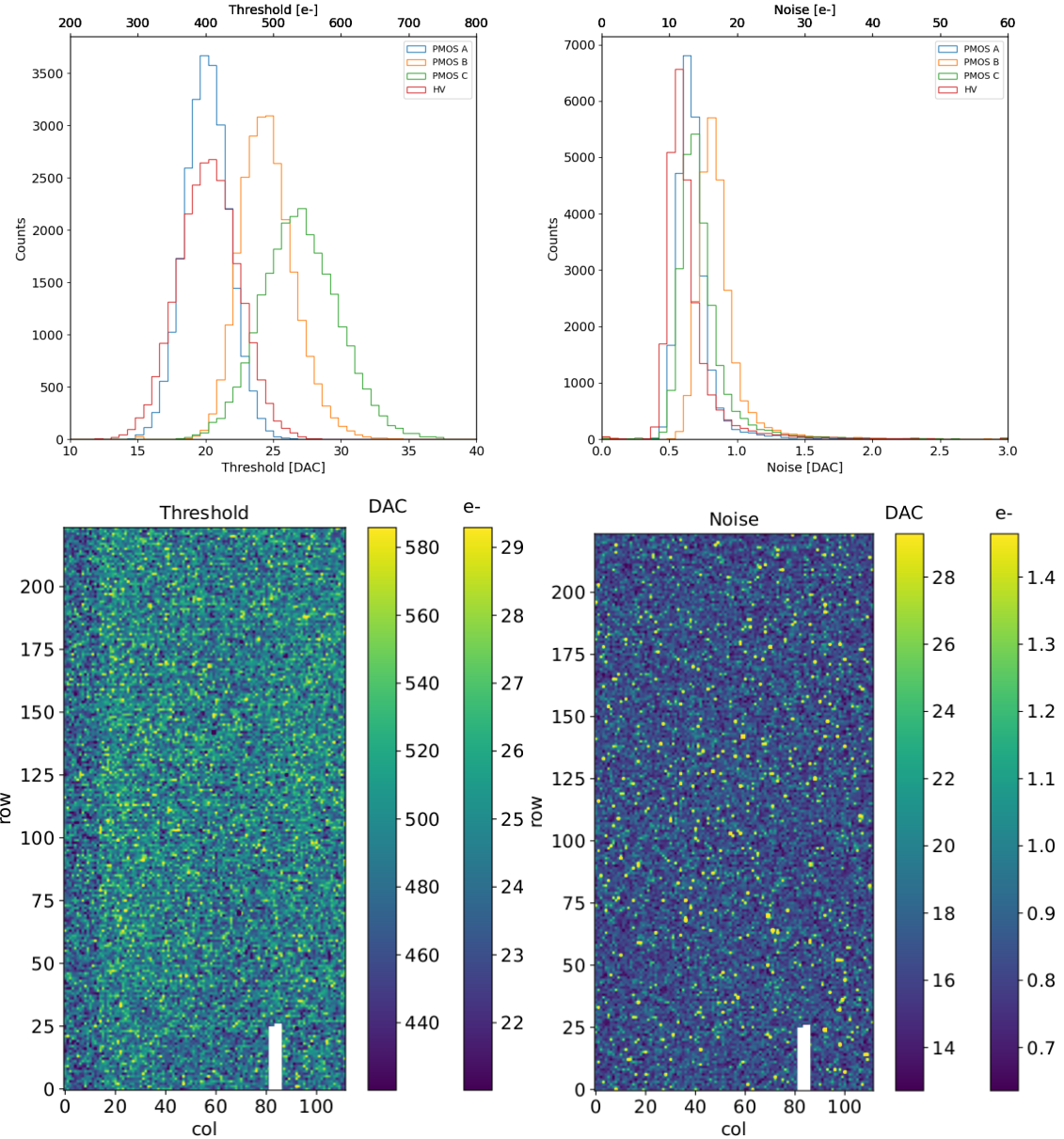


Figure 6.2: Histograms of the threshold (a) and the noise (b) found fitting the s-curve of all flavor with IDB fixed at 40 DAC. Below there are the maps of the threshold (a) and the noise (b), respectively, found fitting the s-curve with IDB fixed at 40 DAC for the PMOS flavor (B). The white pixels have the injection circuit broken.

1064 To verified the trend of the threshold as a function of the front end parameter IDB and
 1065 find its dynamic range, I have permormed different scans changing the IDB: I have injected
 1066 the whole matrix and found the means and the standard deviation of the distributions. The
 1067 results are shown in figure 6.3: the blue points are the mean threhsold found whithin the
 1068 matrix, while in green is shown the width of the threshold distribution, aka the threshold
 1069 dispersion. While the threshold increases, the ENC decreases of $\sim 4 \text{ e-}$,which is $\sim 1/3$ of
 1070 the noise at IDB=40 DAC.

1071 Then, to evaluet the operation and the occupancy of the chip at different threshold
 1072 I have made long acquisitions of noise at different IDB and check how the number of
 1073 pixel masked changes with the threshold. The masking algorithm I have used search for

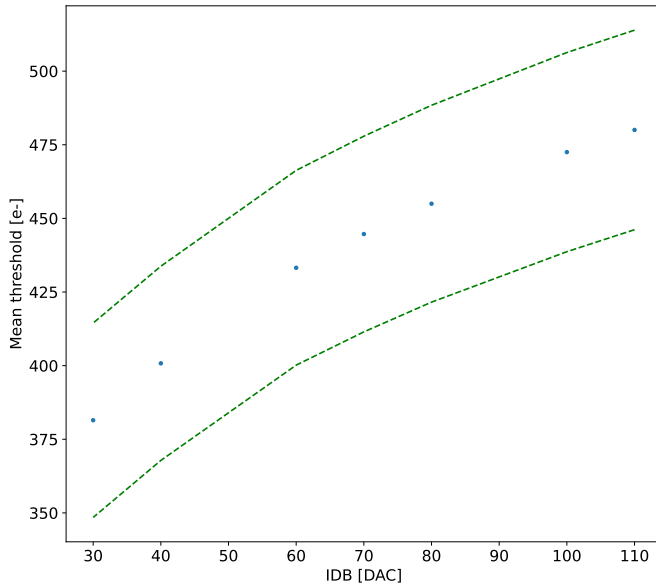


Figure 6.3: Flavor PMOS (B) with Psub-Pwell biased at -6 V. Threshold measured in electrons vs the register which sets the threshold, IDB.

1074 pixels with rate >10 Hz and mask them. With such algorithm, in our standard condition,
 1075 IDB=40 DAC, a very low noise hit rate is intentionally achieved masking only **dozen of**
 1076 **pixels?** of the whole flavor, and other **quanti** are unintentionally masked.

1077 6.1.2 Linearity of the ToT

1078 I have already said in chapter 4 that TJ-Monopix1 returns an output signal proportional to
 1079 the charge released by a particle in the epitaxial layer, which is the Time over Threshold;
 1080 the ToT is saved as a 6-bit variable and then has a dynamic range equal to 0-64, which
 1081 corresponds to 0 μ s to 1.6 μ s assuming a clock frequency of 40 MHz. When a pulse is longer
 1082 than 1.6 μ s the counter rolls back to zero and there is no way to distinguish that charge
 1083 from a lower one with the same ToT: that is the rollover of the ToT (??(a)).

1084 In order to associate the ToT (in range 0-64) to the charge, a calibration of the signal
 1085 is necessary. Assuming the linearity between ToT and the charge, Q can be found:

$$Q [DAC] = \frac{(ToT [au] - q [au])}{m [au/DAC]} \quad (6.5)$$

1086 where m and q are the fitted parameters of the calibration. It is important to keep in mind
 1087 that the main application target of TJ-Monopix1 is in the inner tracker detector of HEP
 1088 experiments, then the main feature is the efficiency, then a rough calibration of the signal
 1089 to charge is fine. The ToT information can be used both to better reconstruct the charge
 1090 deposition in cluster in order to improve the track resolution, and for particle identification,
 1091 especially for low momentum particles which do not reach the proper detectors.

1092 The study of the output signal is made possible via the injection: since the pulses are
 1093 triangular, the ToT is expected to be almost linear depending on the injection charge value.
 1094 To verify this statement and study the deviations from linearity I've fit the ToT versus the

charge injected for all pixel within the matrix. In figure ??(b) there is an example of fit for a pixel belonging to the flavor B, while in figure 6.5 there are the histograms and the maps of the parameters of the line-fit for all flavors with IDB fixed at 40 DAC. Here again a difference between biasing section appears: since the slope of the ToT is related with the gain of the preamplifier (increasing the gain also increases the ToT), the mismatch is probably due to the transistor contributing to the amplification stage.

Before performing the fit I have calculated the mean value of the ToT of the pulses recorded for each pulse amplitude and I used the mean ToT as value for the fit. The aim of the calibration obviously is finding a relation only in the range 0-64 without taking into account the rolling over hits: therefore, to prevent the rollover data from reducing the mean ToT introducing a bias in the mean value, I cut and I did not consider them. If a signal bigger than the 1.6 μ s is expected in the usage of the detector, the threshold must be raised or the gain reduced, making the expected output signal in range 0-64. In figure ??(b) are shown both the fits with a line (red) and with a second order polynomial (green): at the bounds of the ToT range values deviate from the line model. Since the deviation is low than 1% and it only interest the region near the 0 and the 64, in first approximation it is negligible.

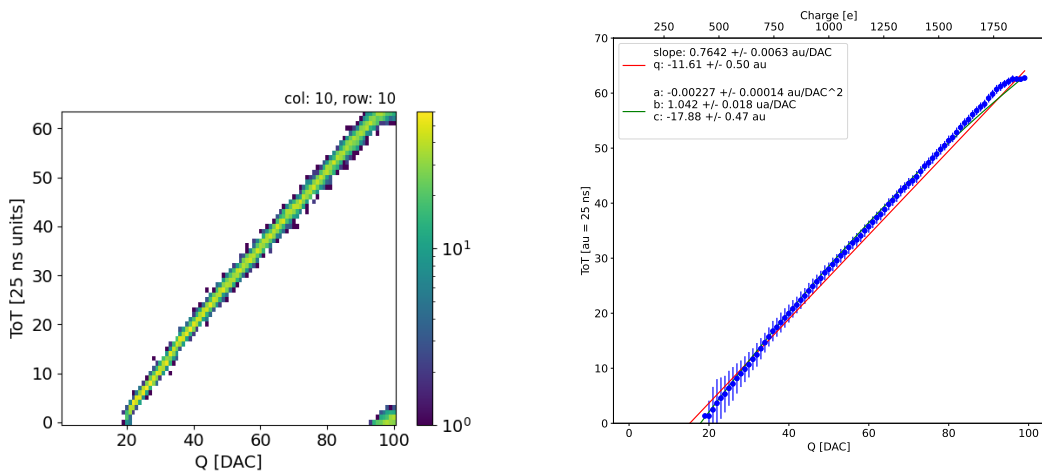


Figure 6.4: The figures refer to pixel (10,10) of the PMOS-reset flavor (1) with IDB fixed at 40 DAC for the PMOS flavor (B). (a) Histogram of the injection pulses: the ToT is in range 0-64 since it is represented by 6 bit, so when achieving the 64 it rolls over back to the zero. (b) Mean ToT vs the the charge: the mean has been calculated cutted the rolling hits.

6.1.3 Calibration of the ToT

Considering that the charge injected in the FE goes to fill capacitor which is different from pixel to pixel, the true charge injected does not correspond to what expected assuming C equal to 230 aF, the nominal value. Accordingly to that, a verification of the value provided and an absolute calibration of this capacity and of the conversion factor F is needed to have a correspondence of the signal in electrons; assuming C 230 aF, F is expected to be $20 \text{ e-}/\text{DAC}$, and is defined as:

$$F [\text{e-} / \text{DAC}] = \frac{1616 \text{ e-}}{Q [\text{DAC}]} \quad (6.6)$$

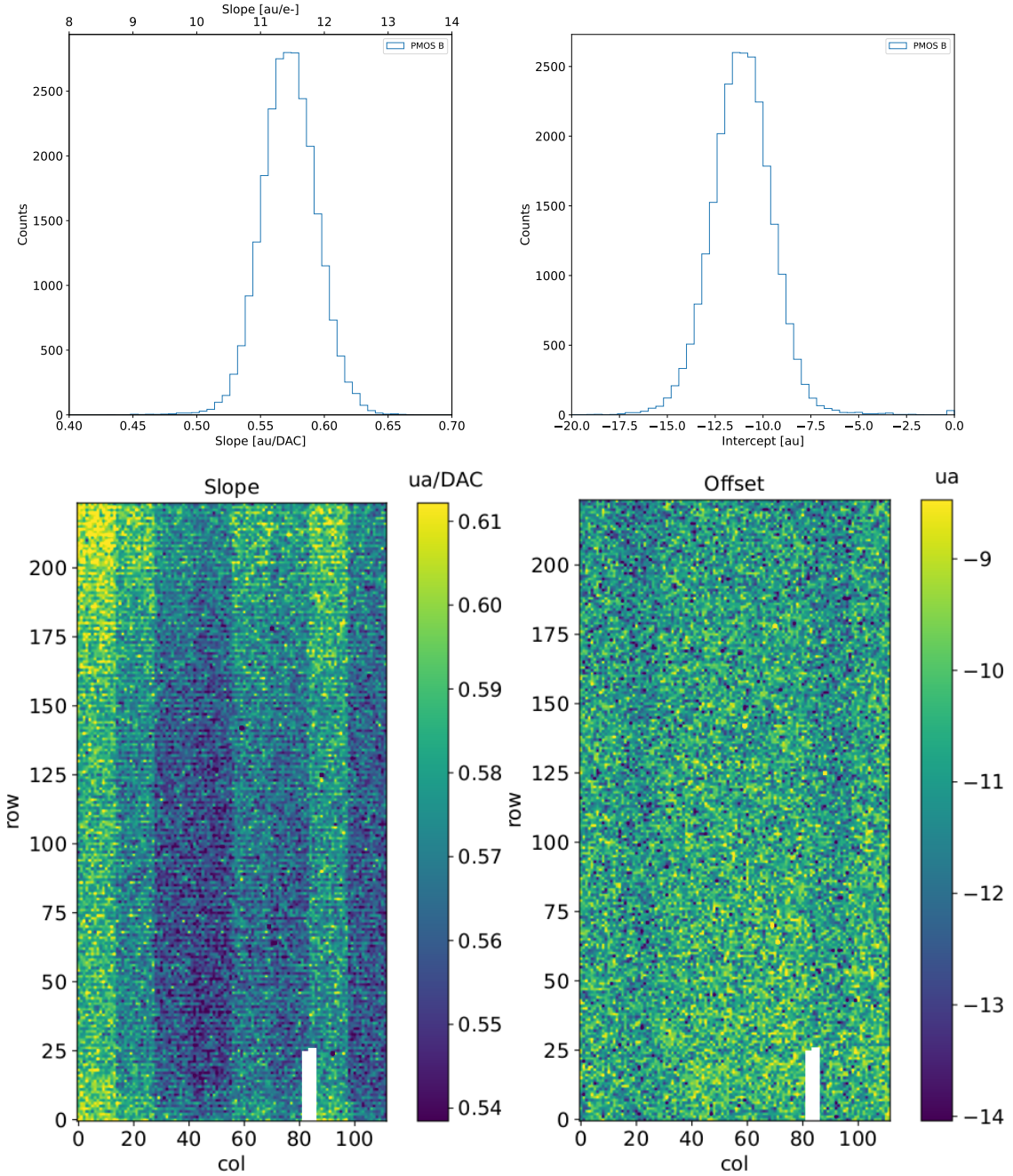


Figure 6.5: Histograms of the calibration parameters, slope (a) and offset (b), found fitting the ToT with a line, for all flavor and with IDB fixed at 40 DAC. Maps of the calibration parameters, slope (a) and offset (b), found fitting the ToT with a line, with IDB fixed at 40 DAC

1119 For this purpose a Fe55 radioactive source has been employed; the Fe55 is an extremely
 1120 important radionuclide in the calibration of X-ray spectrometers, proportional counter
 1121 and scintillator detector since it emits two X-photons during the electron capture
 1122 decay: the first one (K_{α}) at 5.9 keV and the second one (K_{β}) at 6.5 keV. The K_{α} photon,
 1123 which does photoelectric effect in the silicon, has an absorption length $\lambda = 7 \mu\text{m}$ to $8 \mu\text{m}$,
 1124 and the probability of being absorbed in the $25 \mu\text{m}$ thick epitaxial layer is ~ 0.95 . The
 1125 electron emitted has an energy equal to the photon one, so recalling that the mean energy

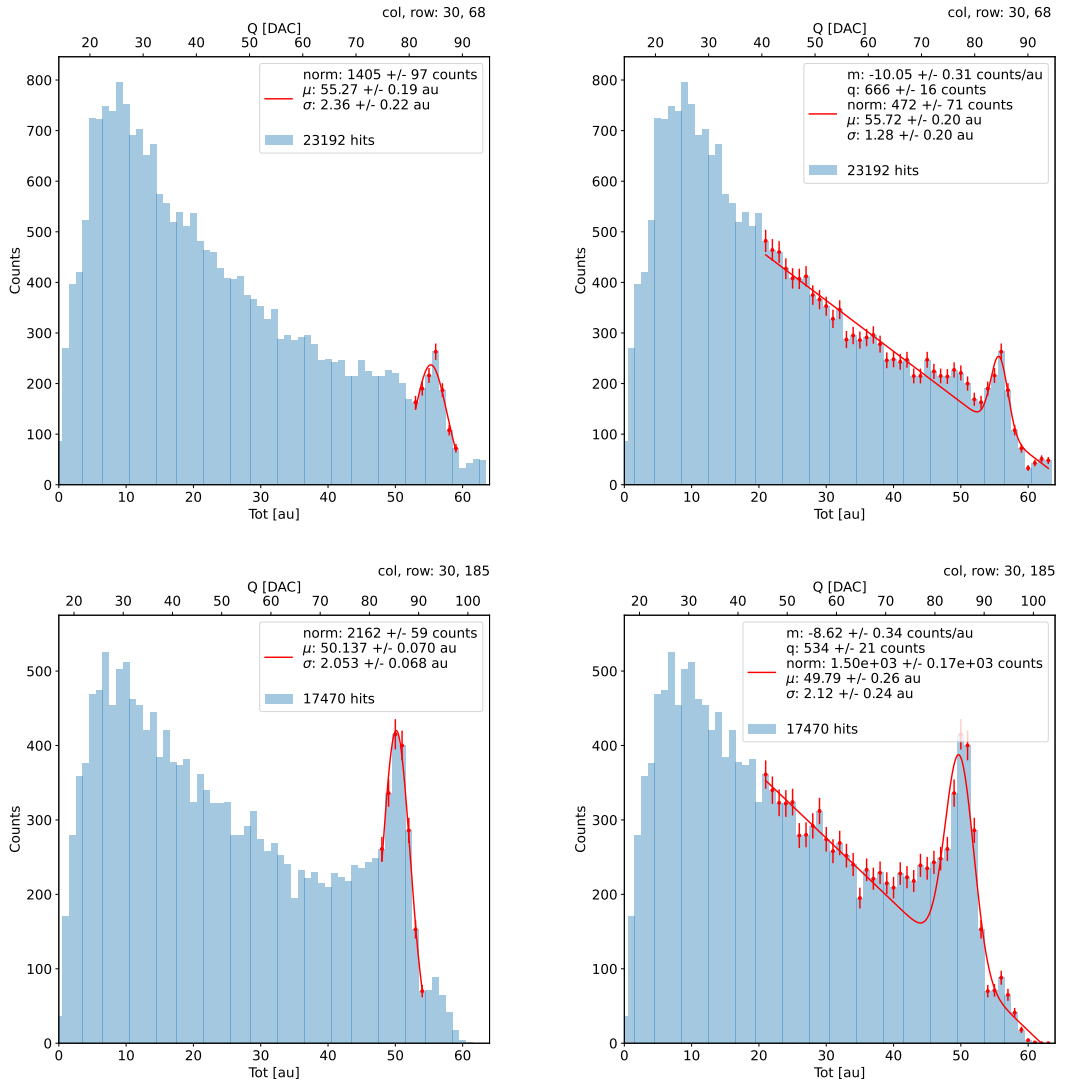


Figure 6.6: due pixel per far vedere la differenza tra i fit. Sottolinea che in rosso ci sono i bin fittati. La doppia scala utilizza le info trovate nel paragrafo precedente per il dato pixel in questione. Per avere una corrispondenza grezza in elettroni basta moltiplicare per 20 e- / dac.

needed to produce a couple electron-vacuum is 3.65 eV, the signal produced by the Fe55 source is expected to be 1616 e⁻. In figures ?? and ?? are shown two histograms of the ToT spectrum of the Fe55 source for two different pixels. The peak corresponds to the events with completely absorption of the charge produced in the depleted region, while the long tail on the left to all the events with partial absorption due to charge sharing among neighbors pixels. In order to reduce the charge sharing, the pixel dimension in TJ-Monopix2 has been reduced down to 30×30 μm². The events on the right side of the peak, instead, corresponds to the K_β photons. Looking at the histograms for pixel (30, 185) and (30,69) a significant difference in the peak to tail ratio leaps out. This difference in the efficiency of detecting the signal can be related with the position of the pixel in the matrix: in particular pixels in the upper part of the matrix (rows 112-224) have a more prominent peak, while in pixels in the lower part (rows 0-111) there is a higher partial absorption. I recall now that there is a slightly difference in the structure of the

1139 low dose-epi layer (??) among the rows in the matrix, in particular pixels in rows 112-224
 1140 are supposed to have a higher efficiency in the pixel corner.

1141 For the calibration I have need to establish the peak position; to do that I perform a
 1142 fit of the ToT histogram of each pixels. As fit functions I test both the solutions below:

$$f(x, N, \mu, \sigma) = \frac{N}{\sigma\sqrt{2\pi}} e^{-\frac{1}{2}(\frac{(x-\mu)}{\sigma})^2} \quad (6.7)$$

$$f(x, m, q, N, \mu, \sigma) = m x + q + \frac{N}{\sigma\sqrt{2\pi}} e^{-\frac{1}{2}(\frac{(x-\mu)}{\sigma})^2} \quad (6.8)$$

Nel primo caso ho fissato pochi pixel attorno a picco: il range è stato determinato ..

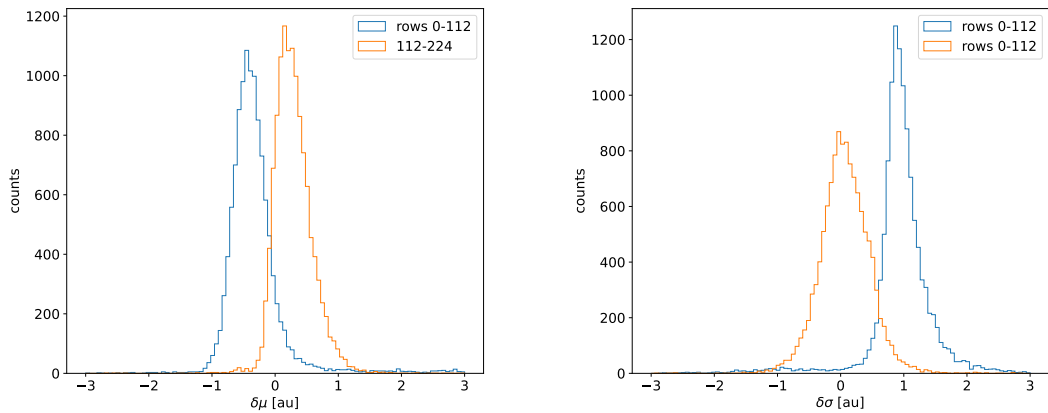


Figure 6.7: Here there are shown the defference between the parameters μ and σ fitted with only a gaussian and with a gaussia plus a line. When $\mu < 0$ the fit function 6.7 has given a worst peak (shifted on the left); when $\sigma < 0$, 6.8 has given a worst peak width (larger sigma)

1143
 1144 **controlla. Nel secondo caso invece il range è.. Controlla sullo script** Even if the difference
 1145 in the peak position between the two cases is not really relevant (6.7) being of the order
 1146 of 0.8-1.5 %, it still introduces a systematic effect moving the peak on the left because of
 1147 the contribution of the tail. Indeed, we know that the sharp edge on the right corresponds
 1148 to the complete absorption of the photon, so excluding the little bump on the right, the
 1149 more the fitted parameter is on the right, the better the fit is. Moreover, there is also
 1150 systematic effect on the peak width, infact the worst fit also gives an overestimation of
 1151 the peak width. Even looking at the χ^2 , the fit function 6.7 seems so be the better choise,
 1152 except for a sample of pixels on the lower part of the matrix, the one with lower efficiency.

1153 **Mappa del ferro da cui, come descritto enll'equazione si ricava la capacity. La struttura**
 1154 **a bande della capacità ha origine nel plot... e quindi nella calibrazione. Andando a vedere**
 1155 **gli istogrammi di queste due variabili si vedono dei picchi. C'è qualche struttura nella**
 1156 **matrice che condiziona il funzionamento delle righe? Larghezza della gaussiana: fai il**
 1157 **discorso a cosa contribuisce ad un picco così largo. è compatibile con quanto ti aspetti?**
 1158 The voltage fluctuation around the peak is caused by the number fluctuation of generated
 1159 carriers (Fano noise) and the noise introduced by the detector (sensor and front-end pre-
 1160 amplifier). The ENC can be estimated from the standard deviation of the Kalpha voltage
 1161 distribution. ENC = sqrt(sigma misurata- quella che ti aspetti dal fattore di Fano). E

1162 compatibile con quanto trovato? se non fosse compatibile rimaneggia questa frase: tra noise
is added from the system (test setup) at the analog monitoring pixel output.

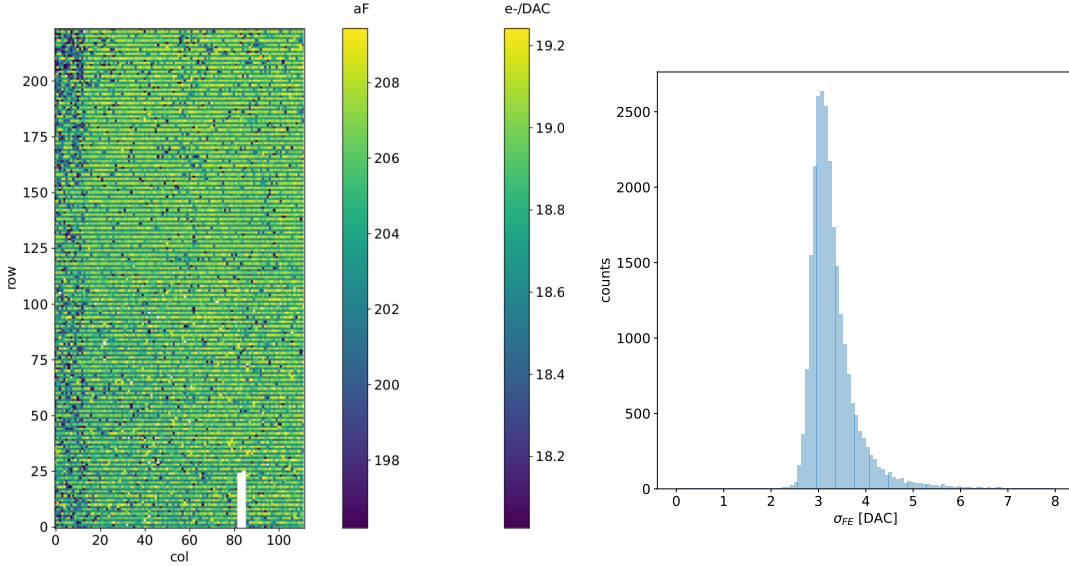


Figure 6.8

1163

1164 6.1.4 Changing the bias

1165 In order to study the behavior of the sensor changing the bias, I perform some injection
1166 scans in different configurations. The thickness of the depletion has to be considered
1167 indeed an important parameters for the efficiency of the signal, and in particular it affects
1168 the charge released by a particle which cross the sensor (since the signal is proportional to
1169 the thickness of the epitaxial layer). Given that the chip under examination has a gap in
1170 the low dose epi-layer (look at chapter 4.1) we were not able to change independently the
1171 bias of the substrate (PSUB) and of the p-well (PWELL), but they must be kept at the
1172 same value, differently from other chips, where on which some test has been performed, as
1173 reported in figure 6.9. A 2D map of the measured output voltage amplitude and resulting
gain in the case of the PMOS and HV are reported.

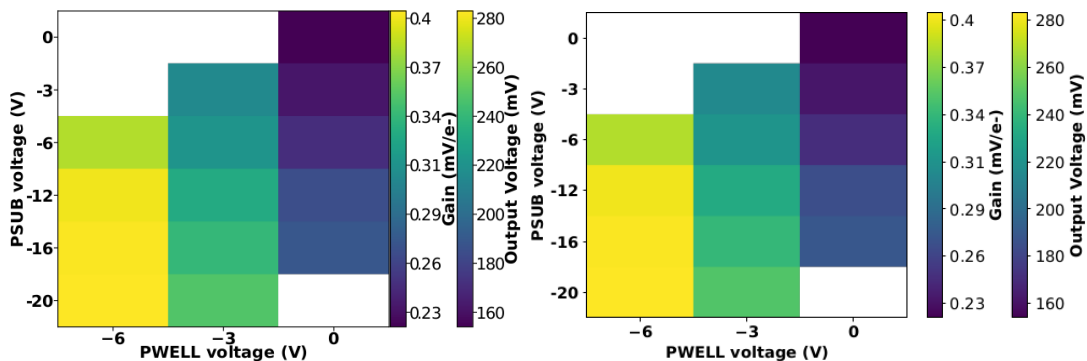


Figure 6.9: 2D map of the output voltage amplitude and gain with respect to the p-well
and p-substrate in the case of the PMOS reset front-end (B)

1174

1175 In order to test the behavior of the chip when not completely depleted, I have performed
1176 an injection scan with PSUB/PWELL bias at 0 V, -3 V and -6 V, and some acquisitions

	-6 V	-3 V	0 V
Threshold [DAC]	20.04 ± 1.6	21.0 ± 1.6	24.5 ± 1.8
Noise [DAC]	0.613 ± 0.075	0.625 ± 0.078	0.822 ± 0.098
Slope [au/DAC]	0.726 ± 0.027	0.707 ± 0.028	0.573 ± 0.021
Offset [au]	-10.8 ± 1.9	-11.2 ± 1.8	-11.1 ± 1.5

Table 6.2: The errors are the standard deviations of the corresponding distributions. The conversion factor from DAC to electrons is $\sim 20 \text{ e}^-/\text{DAC}$.

with the Fe55 source. The results of the measurements are reported in table 6.2 and in figure ???. Turning down the bias, the depletion region narrows and the efficiency reduces, in particular in the pixel corner; in particular the threshold increases of $\sim 1/4$, the noise of $\sim 1/3$ and the slope, which parameterizes the linearity of the analog output and strictly depends on the gain, decreases of $\sim 1/4$. In figure 6.10(b) are reported the values of the K_α peak position, the normalization of the events above the peak and the rate, everything has been normalized to the value at the reference condition, which is with PSUB/PWELL at -6 V. In order to evaluate the peak position and the normalization I have fit the spectrum in the region on the right with a gaussian. Looking at the spectrum, another characteristic seems to appear: at lower bias the peak width is bigger than in a full depletion mode. This could be due to a bigger capacity, which influence the noise.

6.1.5 Measurements with radioactive sources

In order to completely validate the operation of the whole sensor¹, I have made some acquisitions with radioactive source, in particular I have used Fe55, Sr90, which is a β^- emittitor with electron endpoint at 0.546 MeV, and cosmic rays, which are supposed to be mostly MIP. In the acquisitions with Sr90 and cosmic rays, I specifically focused on the events with charge sharing and with more hits than one per events, that are clusters.

The definition of cluster I chose is built only on the time of arrival of hit, in particular I established that all particles with the same timestamp belong to the same cluster. This obviously is a coarse requirement but it gave me the opportunity of using a simple and fast clustering algorithm, which is fine when the random coincidence probability is negligible. Defining R_1 and R_2 as the two events rate, and τ as the dead time of the detector, the random coincidence rate can be found:

$$R_{coinc} = R_1 \times R_2 \times \tau \quad (6.9)$$

As I am going to prove in the next section, the dead time strictly depends on the occupancy of the matrix, even though we can assume a dead time of $\sim 1 \mu\text{m}$, which corresponds to the mean dead time per pixel. However, if in an event a particle hit two different pixels producing a cluster, the total dead time simply doubles. Then, assuming a rate of noise of $\sim \text{Hz}$ on the whole matrix and being the mean rate of the , the random coincidence of two hits coming from Fe-noise, Sr-noise, CR-noise and noise-noise are respectively

In figure ?? I report the histograms of the number of pixels in the cluster and of the

¹As I will explained in chapter ?? these measurements are fundamental also to be compared with the spectrum seen at the testbeam

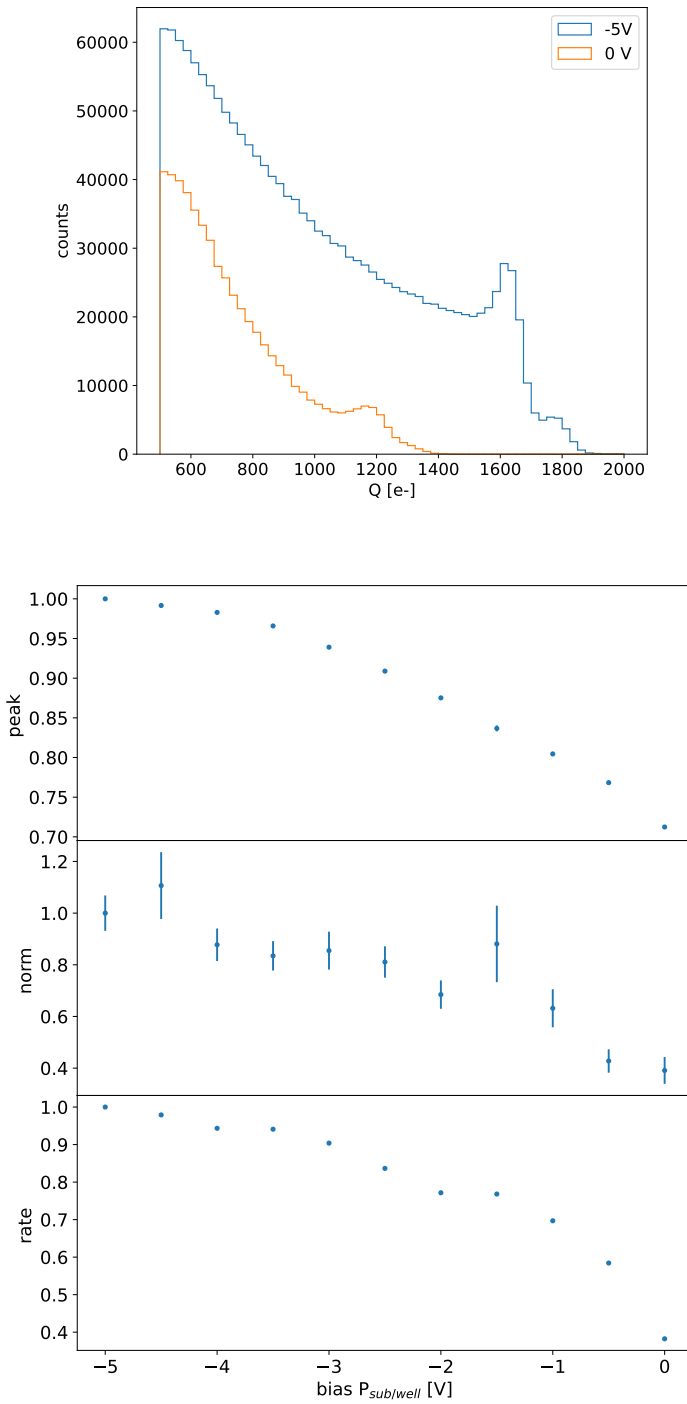


Figure 6.10: Two acquisition with the Fe55 source at different bias.

dimension of clusters, defined in terms of the max and min coordinates on the matrix as:

$$d = \sqrt{(y_{max} - y_{min})^2 + (x_{max} - x_{min})^2} \quad (6.10)$$

quello che si nota è che lo Sr fa cluster più grandi mediamente, che arrivano anche a 22 hit.

Below I have also attached a sample of hitmap of events produced by the three different sources.

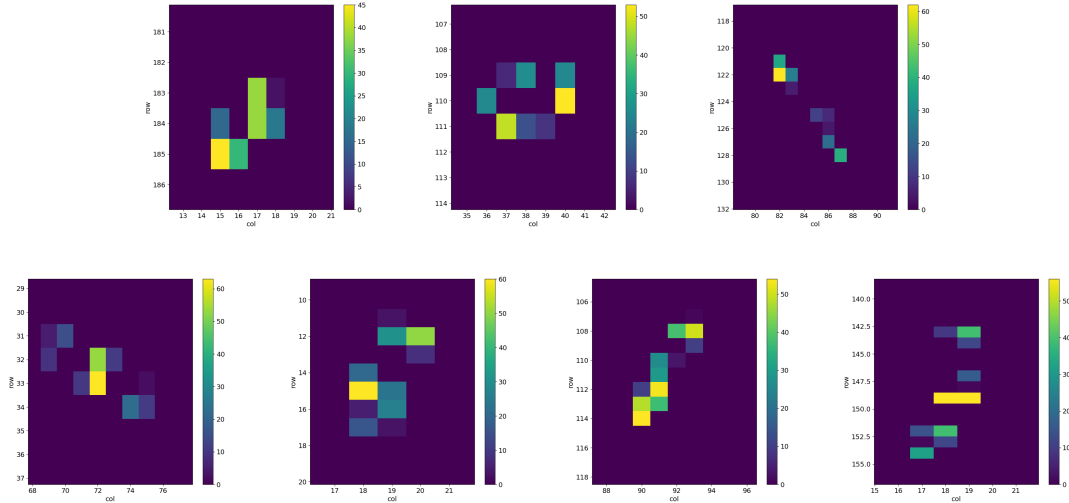


Figure 6.11

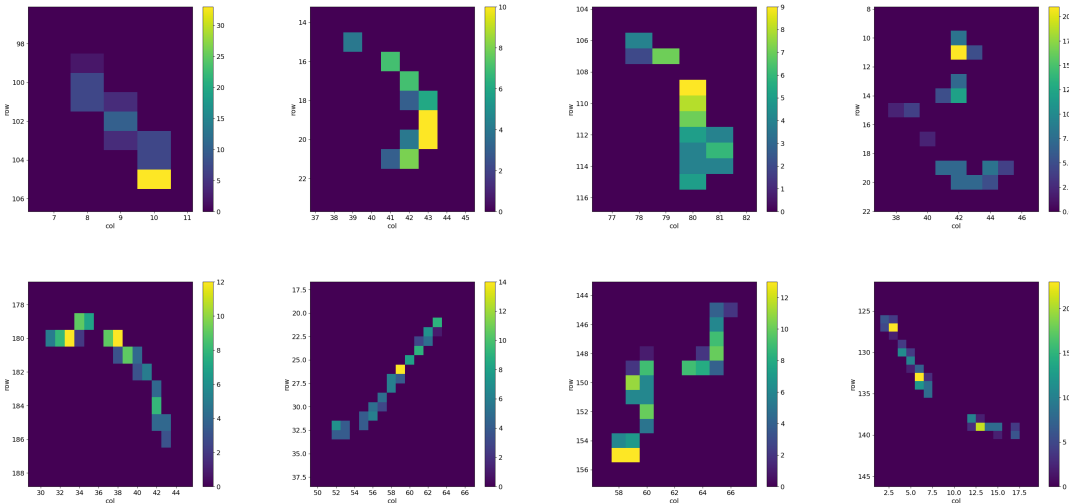


Figure 6.12

- 1212 • PLOT delle hit per cluster
- 1213 • esempio di heatmap di cluster
- 1214 • sostituisci in carica in un file del ferro, guarda somma dei cluster, stessa cosa per Sr
- 1215 • e MIP
- 1216 • Spiega che con il flavor HV abbiamo una perdita di segnale, fai vedere uno spettro
- 1217 • di delle misure dell'8 marzo.

1218 The signal generated by electrons is similar to the one generated by minimum ionizing
 1219 particle (MIPS) **dovrei mettere qualche conto per giustificare questa affermazione**, and the
 1220 spectrum is expected to follow a Langau-Gauss distribution. **nelle acquisizioni dei CR ho**
 1221 **selezionato solo i cluster, per tagliare via il rumore.**

1222 , looking at the cluster dimension and the cluster charge.

1223 **6.1.6 Dead time measurements**

1224 The hit loss is due to analog and digital pile up: the first one occurs when a new hit
 1225 arrives during the pre-amplifier response, the second instead when the hit arrives while
 1226 the information of the previous hit has not yet been transferred to the periphery. Since
 1227 the pre-amplifier response has a characteristic time \sim ToT, the dead time τ_a introduced by
 1228 it will be at most 1.6 μ s; using the IRESET and VRESET FE parameters the reset time
 1229 can be lowered down, but a **IRESET, puoi diminuire il tempo di scarica.** Regarding the
 1230 latter contribution instead, since only one hit at a time can be stored on the pixel's RAM,
 1231 until the data have completed the path to get out, the pixel is paralyzed. Moreover since
 1232 there is no storage memory included on TJ-Monopix1 prototypes, the digital dead time
 1233 τ_d almost corresponds to the time needed to transmit the data-packets off-chip.

1234 The exportation of data from pixel to the EoC occurs via a 21-bits data bus, therefore
 1235 only one clock cycle is needed and the dead time bottleneck is rather given by the
 1236 bandwidth of the serializer which transmits data off-chip from the EoC. In our setup the
 1237 serializer operates at 40 MHz, thus to transmit a data packet (27-bit considering the ad-
 1238 dition of 6 bits to identify the double-column at the EoC) at least 675 ns are needed. For
 1239 what we have said so far, the R/O is completely sequential and therefore is expected a
 1240 linear dependence of the reading time on the number of pixels to read:

$$\tau = 25 \text{ ns} \times (\alpha N + \beta) \quad (6.11)$$

1241 where α and β are parameters dependent on the readout chain setting.

1242 To test the linearity of the reading time with the number of pixels firing and to measure
 1243 it, I have used the injection circuit which allows me choosing a specific hit rate: I made
 1244 a scan injecting a fix number of pulses and each time changing the number of pixels
 1245 injected. Indeed the injection mode allows fixing not only the amplitude of the pulse,
 1246 which corresponds to the charge in DAC units, but also the time between two consecutive
 1247 pulses (DELAY) and the width (WIDTH). The hit rate then corresponds to :

$$R = \frac{25 \text{ ns}}{(DELAY + WIDTH)} \quad (6.12)$$

1248 where WIDTH is equal to 60 counts.

1249 Unfortunately a high random hit rate on the matrix cannot be simulated by the in-
 1250 jection because of the long time (\sim ms) needed to set the pixel registers of the injection;
 1251 then I was forced to specify at the start of the acquisition the pixels to inject on, and for
 1252 convenience I chose those on a same column. In figure 6.13 is shown the dependence of
 1253 the efficiency on the DELAY parameter in two different cases. For the 5 pixels example
 1254 the efficiency goes down the 90% at a DELAY of \sim 185 clock counts, which corresponds
 1255 to 6.125 μ s and to a rate of 160 kHz, while in the 10 pixels example, the efficiency goes
 1256 under the 100% at \sim 380 clock counts, which corresponds to 11 μ s and to a rate of 90 kHz.
 1257 **COME MAI SONO DIVERSE LE CURVE?** From the efficiency curves I have then looked
 1258 for the time when the efficiency decreases. In figure 6.14(a) is shown the dead time per
 1259 pixels as a function of N with different R/O parameters configuration, the meaning of
 1260 which is explained in chapter 4.3. The default value suggested by the designer of the chip
 1261 are reported in table 6.3; moving too much the readout parameters from the default ones,
 1262 the readout does not work properly, and no hits can be read at all. The problem probably
 1263 stays in the firmware setting of the readout which are specially fixed for our chip **Sul**

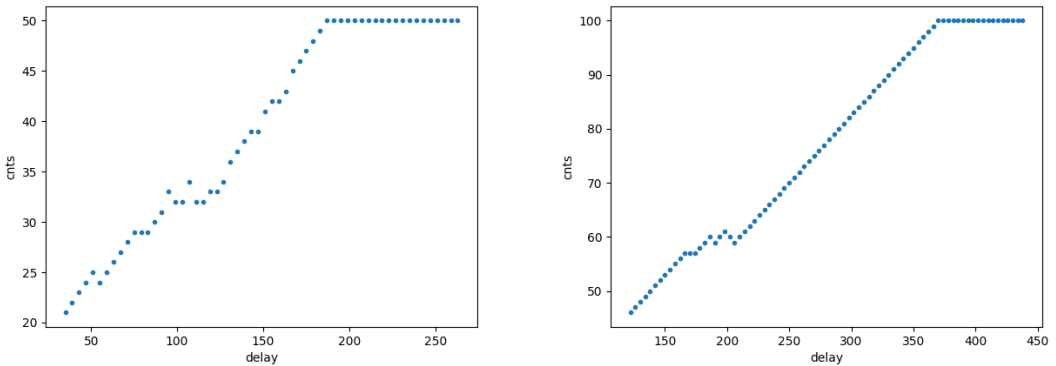


Figure 6.13: Efficiency vs the DELAY parameters. (a) I made a scan injecting 5 pixels with 50 pulses for each DELAY configuration and (b) 10 pixels with 100 pulses for each DELAY

Parameter	Value [DAC]	Value [μs]
START_FREEZE	64	1.6
STOP_FREEZE	100	2.5
START_READ	66	1.65
STOP_READ	68	1.7

Table 6.3: Default configuration of the R/O parameters

1264 repository, nei commenti ci sono altri valori possibili per il FREEZE, ma avevamo detto
 1265 che probabilmente sono relativi ai setting di altri chip. Despite the single pixel reading
 1266 time does not depend on the position on the pixel matrix, whithin a clock count which
 1267 is ~ 25 ns, and it is equal to 106 clock counts, since the τ_d critically depends on the pixel
 1268 position on the matrix: in particular the reading sequence goes from row 224 to row 0,
 1269 and from column 0 to column 112, making the pixel on the bottom right corner the one
 1270 with the longest dead time.

1271 Furthermore to test that there is no dependence of the digital readout time from the
 1272 charge of the pulse, I have try to change the amplitude of the pulse injected, but the
 1273 parameters found were consistent with the default configuration ones. No difference in the
 1274 α and β coefficients has been observed between the two case. In realtà non mi torna perchè
 1275 il FREEZE dovrebbe iniziare n cicli di clock dopo il TE, ed il TE dipende ovviamente dal
 1276 ToT, quindi mi sarei aspettata una differenza tra i due. Referring to eq.6.11, the factor
 1277 α is proportional to the difference (STOP_FREEZE - START_READ), while the offset β
 1278 lies between 5 and 15 clock counts.

1279 Per avere una misura veritiera del tempo morto e del hit loss si dovrebbe iniettare
 1280 casualmente input events are produced by a random hit generator with a specified hit
 1281 rate, hence following a Poisson distribution. Inoltre faccio notare che il tempo morto
 1282 è così lungo perchè c'è parallelizzazione e neppure un buffer (cosa tipicamente prevista
 1283 quando li si inserisce nei rivaltori). Ad esempio Obelix, per l'upgrade di Belle2 avrà un
 1284 buffer a fine matrice.

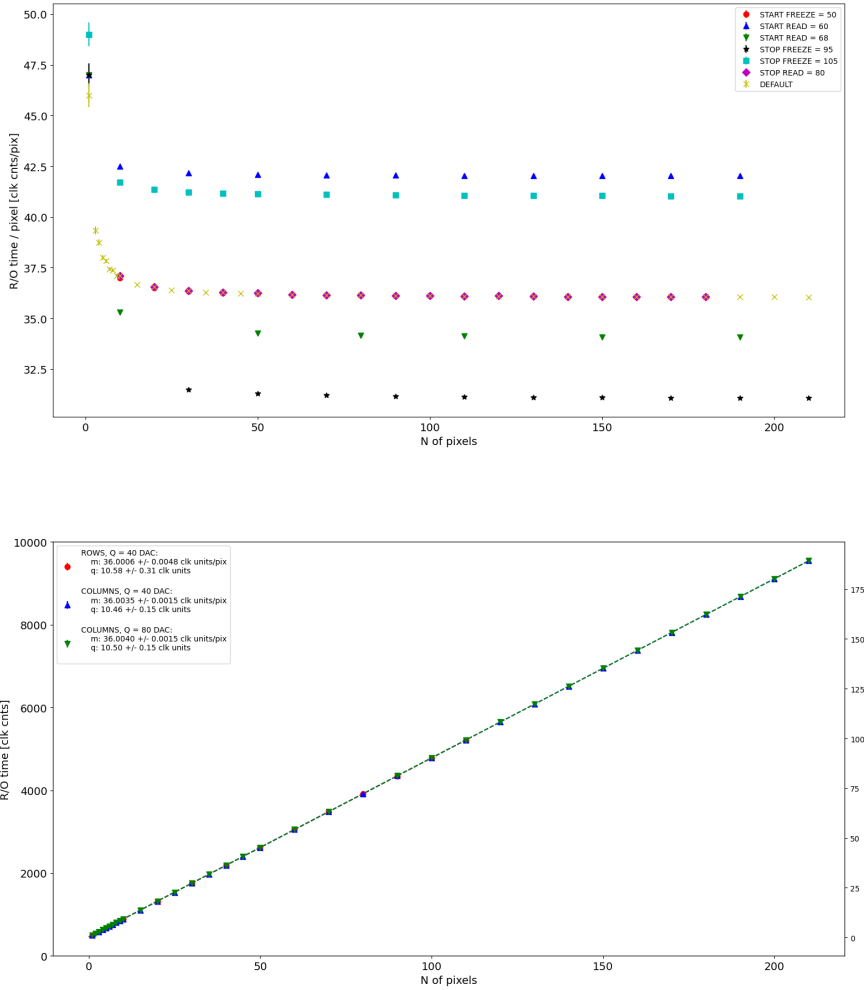


Figure 6.14: (a) Readout time per pixel as a function of the number of pixel injected obtained with different FE setup. (b) Readout time as a function of the number of pixels injected obtained injecting pulses with amplitude of 80 DAC (green), of 40 DAC on the same row (red) and on the same column (blue).

1285 6.2 ARCADIA-MD1 characterization

1286 Unfortunately we have found out that the chip we received was not completely functional,
 1287 then we have been able to make on it only a few electrical and software test. We have
 1288 then verified the communication of the chip with the DAQ, testing the operations of the
 1289 FPGA and the breakout board (BB). The problem occurs when the chip is biased, in
 1290 particular, when the HV voltage is lowered down 0 V, the sensor requires too much power
 1291 and a too high current draw sets. We have discussed the problem with the designers of
 1292 the chip whose helped us indentifying the motivation of the break: the chip has been
 1293 glued using too much conductive tape and hence have a short-circuit between the sides
 1294 and the back, which makes impossible the biasing. Unfortunately, since both the sensor
 1295 and the FE require at least -10 V to work properly, no measurement was possible except
 1296 the acquisition of the noise in the FE circuit.

1297 We received then another chip, a minid2, that is a "mini demonstrator" from the

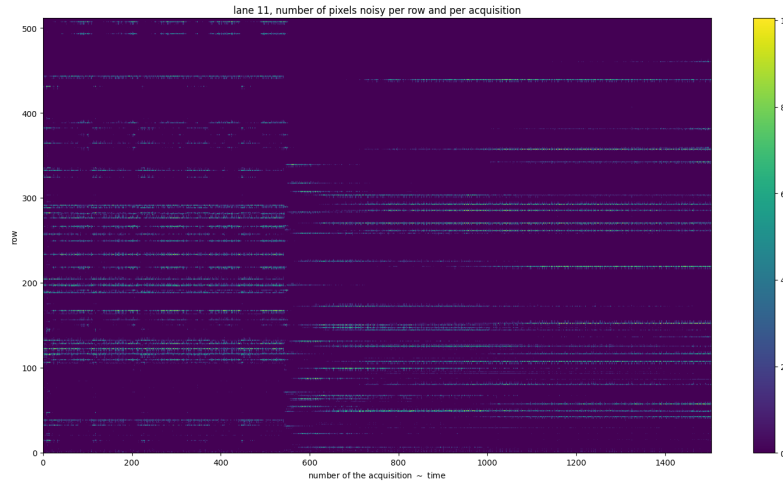


Figure 6.15: Noise in the front end circuit depending on the bias road across the matrix was recorded.

1298 second submission. The two chips have the same characteristics but the minid2 is smaller
 1299 than the MD1, in particular it only have 32×512 pixels, instead of 512×512 . **scrivi il**
 1300 **problema della prima sottomissione.**

1301 An exhaustive characterization and testing of the new chip have been going on in the
 1302 clean room on the INFN, and I am going to show here only some preliminary results. Up
 1303 to now we used the injection circuit in order to make a threshold scan on a few pixels:
 1304 differently from the TJ-Monopix1's charaterization where we performed a scan changing
 1305 the injection charge of the pulse, with the minid2 we have instead changed the threshold
 1306 (whose register is VCASN) keeping the charge of the pulse fixed. For each threshold we
 1307 inject 100 pulses of amplitude $10 \mu\text{s}$. The dependece of the efficiency on the threshold for
 two pixels is shown in figure 6.16.

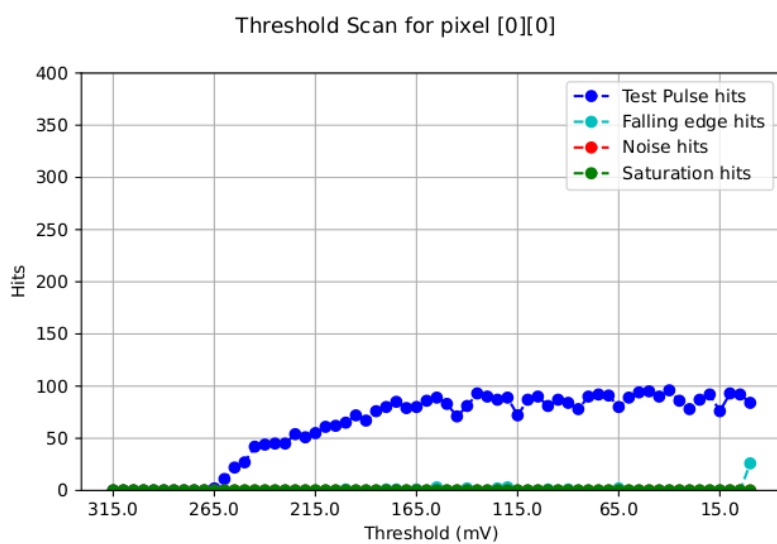


Figure 6.16

1308
 1309 Anche se il comportamento è globalmente ragionevole, con l'efficienza che sale quando

1310 si abbassa la soglia, viene il sospetto che non stiamo polarizzando bene il sensore e il
1311 FE dato che anche raggiunto i centi conteggi, si hanno delle fluttuazioni intorno a questo
1312 valore. Inoltre notiamo che abbassando ulteriormente la soglia si osserva un aumento delle
1313 hit, dovuto al fatto che si inizia a triggerare sul rumore.

1314 commenta sul fatto che non è stabile anche molto sopra la soglia. Forse è dovuto al
1315 bias? oppure l'impulso ha qualche problema (non abbiamo settato la durata ecc..)? Che
1316 valore ha in elettroni?

1317 Substantial differences have been observed in both the efficiency and the threshold
1318 among the sections, with VCASN=40 DAC; this suggests that with this particular FE
1319 configuration there is a big threshold dispersion on the matrix. The hitmap of an ac-
1320 quisition with the Fe55 source is shown in figure 6.17: the whole MD1 matrix with only
1321 the bottom region (32 rows) working is represented in (a), while in (b) there is a zoomed
1322 hitmap. The rate seen within the region 8 (green region in the figure (a)) is compatible
1323 with the rate of the same radioactive source measured with TJ-Monopix1, that it \sim 3.3 kHz.
Looking to the Sr90 acquisitions (fig.6.18) many clusters and tracks can be immidiately

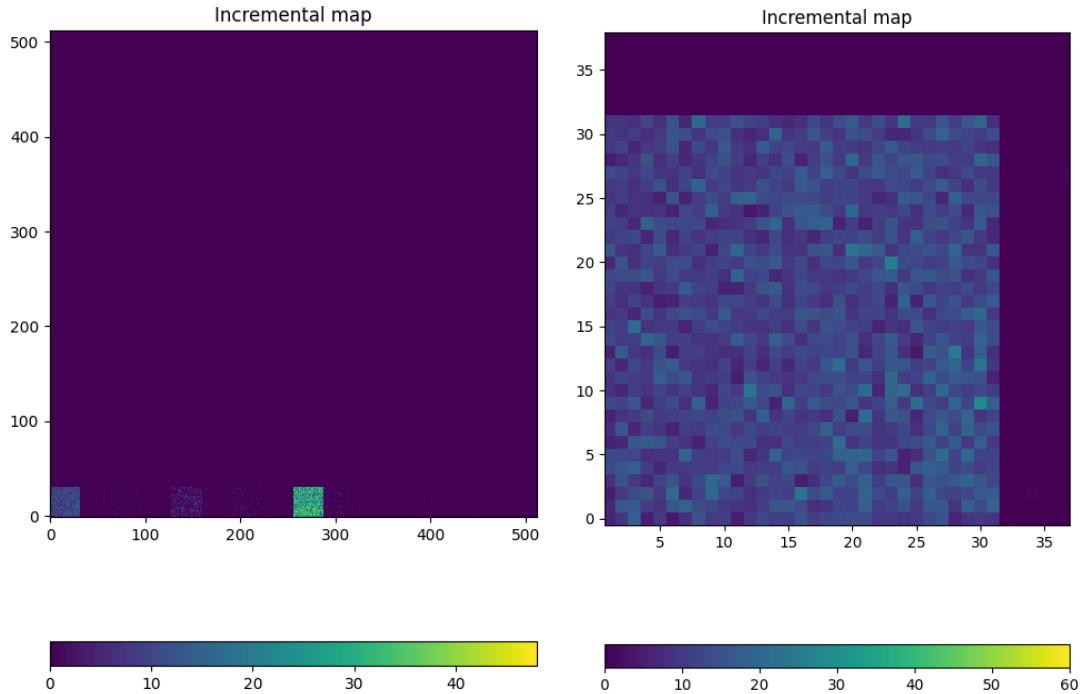


Figure 6.17: Fe55 acquisition with VCASN=40 DAC. (a) All the matrix 512×512 is plotted even if the minid2 has only the rows in range 0-32. (b) A zoom on the first section (col 0-32).

1324
1325 distiguished, confirming what observed with TJ-Monopix1.

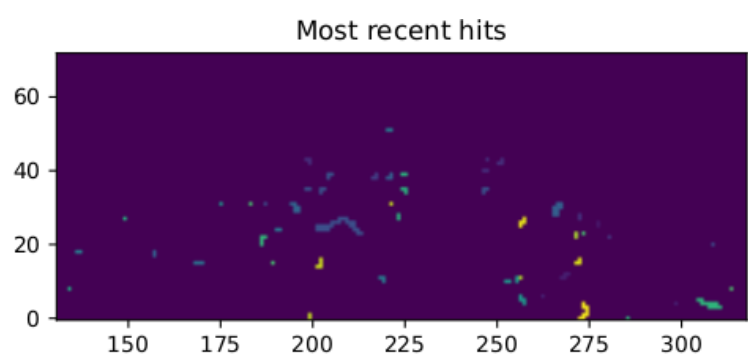


Figure 6.18: Sr90 acquisition with VCASN=40 DAC. The different colours are related with the time of arrival of the hits: in yellow the most recent hits, while in blue the old ones.

1326 **Chapter 7**

1327 **Test beam measurements**

1328 At PRF smaller than 100 Hz, all the dosimeters analyzed have a shorter signal collection
1329 time with respect to the repetition time of the pulses (maggiore uguale 10 ms), and,
1330 consequently, the saturation is influenced only by the dose-per-pulse (duration of the
1331 pulse is around 2.5 us)

1332 During August 2022 a testbeam took place in Santa Chiara hospital in Pisa, where a
1333 new accelerator designed for both medical research and R&D in FLASH-RT, and for this
1334 reason called "ElectronFlash", have been installed a few months ago.

1335 The motivation of the testbeam measurements were testing TJ-Mopopix1 in condition
1336 different from the one foreseen during the design and also testing the mechanical and the
1337 DAQ setup for other future measurement. TJ-Monopix1 is supposed to be employed for
1338 tracking in HEP experiments while our goal was testing the possibility of integrating the
1339 charge released by more particles at ultra high hit rate achievable with the accelerator.
1340 **Una frase di disclaimer sul fatto che non siamo riusciti a testare quello che volevamo.**

1341 In medical physics the dose is indeed the standard parameter to characterize the beam
1342 because of its obvious relation with the damage caused in the patient: firstly the oncolo-
1343 gists prescribe a certain dose taking into account the efficacy of the treatment and then
1344 the medical physicists, on the basis of simulations, decide the energy and the intensity of
1345 the beams to dispense the prescribed dose amount. By the point of view of the instrumen-
1346 tation and the testing on it, a more common and useful parameter is instead the rate or
1347 the fluence of particles. The conversion between the two quantity can be found thinking to
1348 the definition of dose: it is the concentration of energy deposited in tissue as a result of an
1349 exposure to ionizing radiation. Assuming total absorption of electrons in water, defined
1350 by law as the ordinary reference medium, the dose can be expressed as:

$$D[Gy] = \frac{NE[eV]}{\rho[g/cm^3]A[cm^2]x[cm]} \quad (7.1)$$

1351 After having applied the conversion of the energy from eV to J and noticed that $E/\rho x$
1352 roughly corresponds to the stopping power S of electrons in water, a simple estimation of
1353 the dose released in water is:

$$D[Gy] = 1.602 \cdot 10^{-10} N[cm^{-2}] S[MeV cm^2/g] \quad (7.2)$$

1354 **7.1 Apparatus description**

1355 The accelerator is placed in a bunker inside the hospital: to shield the outdoor from
1356 ionizing radiation the bunker has very thick walls of cementum and both the control units

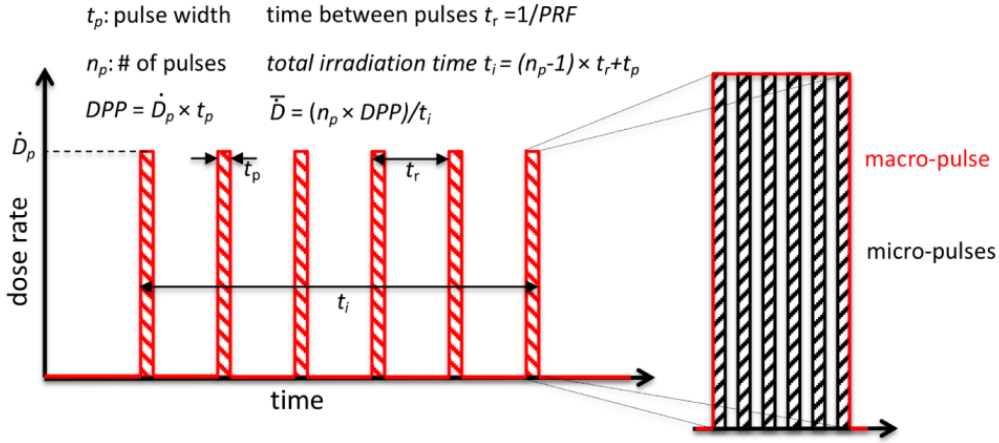


Figure 7.1: Typical beam structure of a beam with the standard characteristic quantity

\bar{D}	Dose rate (mean dose rate for a multi-pulse delivery)	0.005-10000 Gy/s
\dot{D}	Intra pulse dose rate (dose rate in a single pulse)	0.01-1 10^6 Gy/s
DDP	Dose in a single pulse	0.04-40 Gy
PRF	Pulse repetition frequency (number of pulses delivered per unit of time)	1-350 Hz
t_p	Pulse width	0.2-4 μ s
n	Number of pulses	single/pulse train

Table 7.1: The parameters that can actually be set by the control unit are the PRF, DDP, t_p and n (in particular singular irradiation or pulse train), while the other changes consequently.

1357 of the accelerator and of the detector were placed outside the bunker. For practicability
1358 reasons the power supply were the only device to be placed inside the bunker.

1359 7.1.1 Accelerator

1360 The ElectronFlash accelerator is an electron Linear Accelerator (LINAC) with two energy
1361 configurations, at 7 MeV and 9 MeV, and it can reach ultra high intensity (40 Gy/pulse)
1362 keeping the possibility of accessing many different beam parameters and changing them
1363 independently from each other. This characteristic is fundamental for research in FLASH-
1364 RT, both for the medical aspects and for the studies on detectors; for example is not really
1365 clear the dependence of the efficacy of the FLASH effect on the whole dose parameters.
1366 ElectronFlash is **almost the only one** in the world having this characteristic, **ricontrolla sulla**
1367 **review, c'era qualcosa che puoi dire.** The accelerator implements a standard beam struc-
1368 **ture for RT with electrons (fig. 7.1), that is a macro pulse divided in many micropulses;**
1369 **the parameters used to set the dose and their range of values settable by the control unit**
1370 **is reported in table 7.1.**

1371 The accelerator is provided of a set of triod cannons \sim 1.2 m long and with diameters
1372 from 1 cm to 12 cm and a collimator that can be used as beam shaper to produce a
1373 squircle shape. The triode, which is made by plexiglass, must be fix to the gun during the
1374 irradiation and is needed for producing an uniform dose profile (fig.7.2) which is desired
1375 for medical purpose via the scattering of electrons with the plexiglass.

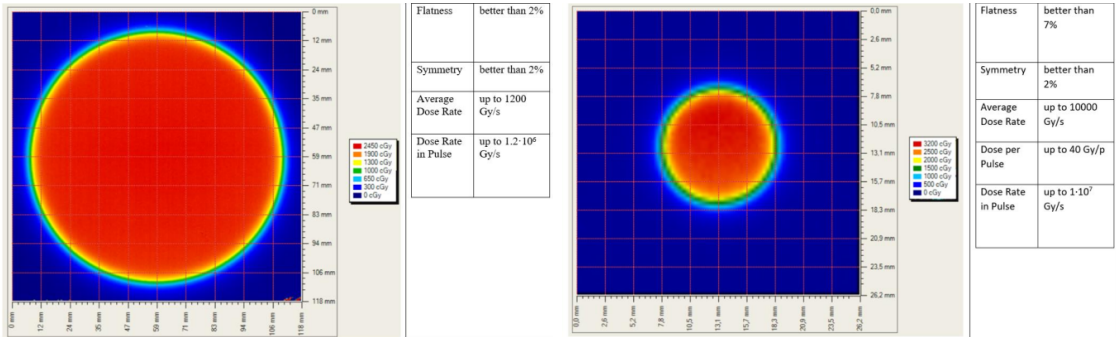


Figure 7.2: Two example of x-y isodose curves for two different triodes, 10 cm and 1 cm respectively, reported by the producer in the manual with the specific of the accelerator (S.I.T. - Sordina IORT Technologies S.p.A.). With the smaller collimator the dose rate in pulse is comparatively higher.

1376 7.1.2 Mechanical carriers

1377 The tested detector consists in one chip, the Device Under Test (DUT), mounted on a
 1378 board and connected to FPGA with same arrangement of figure 7.7. These have been
 1379 positioned vertically in front of the triode on a table specifically built for the testbeam.
 1380 The tree board have been enclosed in a box of alluminium with a window on the DUT
 1381 and with the required holes at the side to enable the biasing via cables and the connection
 1382 with the DAQ provided via ethernet cable. A trigger signal coming from the control unity
 1383 and syncronize with the pulses emitted from the beam has been also sent to the FPGA.
 1384 This signal cannot be considered a trigger signal, since being a prototypes TJ-Monopix1
 1385 has been designed to be triggerless, but the time of arrival of this signal, which is saved
 1386 by the FPGA, can allow the reconstruction of the of the arrival of the bunch during the
 1387 analysis.

1388 In order to shield the sensor from the whole particles emitted from the gun, two
 1389 alluminium collimators have been fabricated: one has been positioned at the triode exit
 1390 while the other in front of the DUT. The collimators are $t=32$ mm thick and have a
 1391 diameter d equal to 1 mm: assuming a beam divergence bigger than $d/t=1/32 = 1.8^\circ$,
 1392 which is the case, the collimator at the triode output was supposed to work as a point
 1393 source and to reduce the rate on the DUT of a factor at least $4 \cdot 10^{-4}$. The second one,
 1394 being near the DUT, was instead supposed to shield the sensor from the electrons which
 1395 have passed the first one, except for a region of 1 mm^2 configurable using **come si chiamano**
 1396 **quei cacciavitini per settare la posizione?**.

1397 7.2 Measurements

1398 Because of the dead time of TJ-Monopix1 it is not possible resolving the bunch sub-
 1399 structure and almost no one pixel can read more than a hit per bunch. I recall, indeed,
 1400 that the dead time per pixel depends on the location on the priority chain for the readout
 1401 and for each pixel $\lesssim 1 \mu\text{s}$ (fig. 7.7) are needed; therefore only a few pixels at the top of
 1402 the priority chain (at the upper left of the matrix) can fire a second time, since they in
 1403 principle can be read the first time before the end of the pulse (assuming a pulse duration
 1404 in $2 \mu\text{s}-4 \mu\text{s}$) and then can be hit again.

1405 Since resolving the single electron track is impossible, a way this sensor could be used

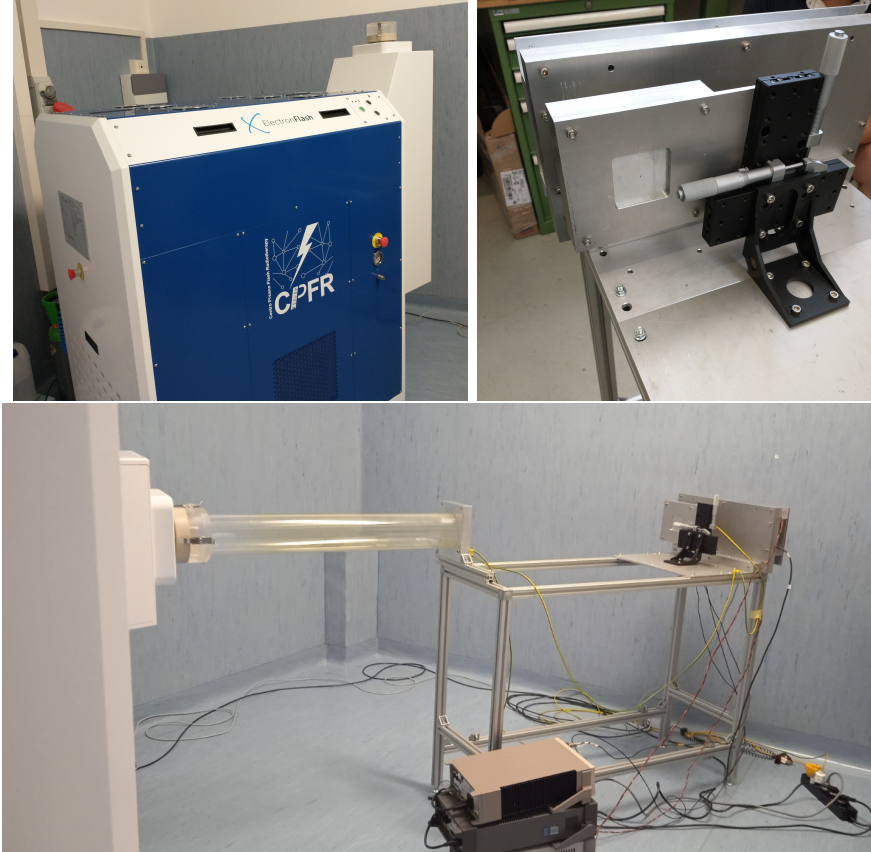


Figure 7.3: Experimental set up. (a) Electron flash accelerator: gantry rotante che consente un orientamento del fascio da 0° 90° (orizzontale / verticale) in tempo reale monitorato da un inclinometro integrato. the gun can be rotated from 90° to 0° (vertical/orizontal). (b) Collimator and DUT box. (c) Whole structure: we used the 10 cm diameter and 1.2 m long triode; the DUT which is in the box behind the two collimators is connected to the power supply units.

1406 in such context is reducing its efficiency and taking advantage of the analog pile up and
 1407 of the linearity of the analog output (ToT), in order to see a signal produced not by the
 1408 single particle but by more electrons. Reducing the efficiency and the sensibility of the
 1409 sensor is essential in order to decrease the high charge signal produced in the epitaxial
 1410 layer: if the sensor is completely depleted the collection efficiency is closer to 1% and if the
 1411 whole charges produced by a MIP, $80 \text{ e}^-/\mu\text{m}$ about, are collected, the saturation limit is
 1412 soon reach. Then a condition where there is a partial recombination of the center electron-
 1413 hole created in the bulk is desiderable. On the other hand, the smaller the output signal
 1414 value and the higher the rate the detector can cope with: indeed, the rollover constitutes
 1415 a limit for the usage of the analog output. With the standard configuration of the FE
 1416 parameters and the epitaxial layer completely depleted, a MIP produces a ToT out of
 1417 range of representation of 6-bit; so as to obtain smaller output signals one can operate
 1418 on the reduction of the gain of the preamplifier or on the pulse velocity of returnig to
 1419 the baseline. Recalling the results in section 6.1.4, I have shown that concerning the
 1420 PMOS flavor 1, reducing the bias from -6 V to 0 V brings a reduction of efficiency down
 1421 to 40 %, and a reduction in the gain of a factor $\sim 1/3$, while the reduction of the gain of
 1422 the preamplifier allows a reduction of **circa 10, ma da controllare**.

1423 In order to taking advantage of the analog pile up and integrating the charge, for
 1424 semplicity assume of two electrons, the second one must hit the pixel before the ToT goes
 1425 under the threshold. The general condition is then $\overline{\Delta T} < \overline{ToT}$, but if a high $P_\mu(n \geq 1)$ is
 1426 required, a lower $\overline{\Delta T}$ may be desired:

$$P(n \geq 1) = \sum_{n=1}^{\infty} \frac{e^{-\mu} \mu^n}{n!} = 1 - P(0) = 1 - e^{-\mu} \quad (7.3)$$

1427

$$\mu = \frac{\overline{ToT}}{\overline{\Delta T}} \quad (7.4)$$

1428 If a $P_\mu(n \geq 1) = 99\%$ then the $\overline{\Delta T}$ must be $\sim 0.22 \overline{ToT}$. The ToT is in range [0,64] but
 1429 since the rollover must be avoided, the \overline{ToT} must be lower than 32, and then the minimum
 1430 rate on the pixel must be 1.25 MHz.

1431

1432 During the testbeam many runs have been performed, spanning the energy, the dose
 1433 per pulse and the four possible configurations with/without the collimators. We have used
 1434 the PMOS flavor 1 in the standard configuration: we have biased the PWELL and PSUB
 1435 at -6 V and set the standard default FE parameters reported in table ???. During all the
 1436 acquisitions we have used pulses with t_p of 4 μm and with the smallest PRF settable, which
 1437 is 1 Hz, in order to start in the most conservative working point exluding the digital pile
 1438 up of events from different bunch: even if the whole matrix turns on and there are 25000
 1439 hits, the total readout time corresponding to 25 ms is still lower than the time between two
 1440 consecutive pulses. The readout starts with the trailing edge of the first pulse going down
 1441 the threshold, ~ 50 clk = 1.25 μs after this moment the FREEZE signal is sent to the whole
 1442 matrix, and the trasmittion of the data to the EoC begins. The hits read are the ones
 1443 whose TE occurred during the 50 clk counts; the ones, instead, whose TE occur during the
 1444 FREEZE are stored in the pixel memory and read during a second readout. Obviously
 1445 since the readout of the fist sub-pulse finishes much later than the bunch ends up, each
 1446 pixel can be store only one hit. An example of the two sub-pulses is shown in figure ???:
 1447 in the acquisition we injected 5 pulses with both the collimators mounted on the table.
 1448 Looking at the spectrum **si vede che lo spettro del secondo pulse ha una coda più lunga a**
 1449 **destra: questo è dovuto al fatto che le hit con tot lungo hanno il TE che cade durante il**
 1450 **FREEZE e quindi vengono lette durante il secondo impulso.** On the other hand the 2D
 1451 histograms, being uniform and not showing disomogenities, suggest that the collimators
 1452 do not shield all the particles: this was due to a photon background higher than expected.
 1453 When we have put aside the collimators, instead, the fluence was too high that **the whole**
 1454 **matrix turns on in 50 clk counts; then the 2 pulses substructure no more appears (fig. 7.6).**
 1455 **CONTROLLA PERCHÈ PORTEBBE ESSERE UNA CAZZATA**

1456 After the testbeam a simulation of the emission of electrons from the accelerator and
 1457 their path across the triode and the collimators has been developed via Geant-4 **come si**
 1458 **ringrazia il lavoro di qualcuno in maniera formale?** The high background we saw although
 1459 the collimators were mainly produced by electrons Bremsstrahlung during the transition
 1460 through the alluminium collimators. **dalla simulazione si è visto che nessun elettrone**
 1461 **arriva sul chip quando ci sono montati i collimatori, mentre nel caso senza collimatori gli**
 1462 **eventi sono sostanzialmente tutti elettronni (frazione di fotoni prodotti in aria è?).** The
 1463 photons' simulated spectrum in the three configurations are shown in figure ???. **confronto**
 1464 **con quello che vedo nello spettro sopra: dati.**

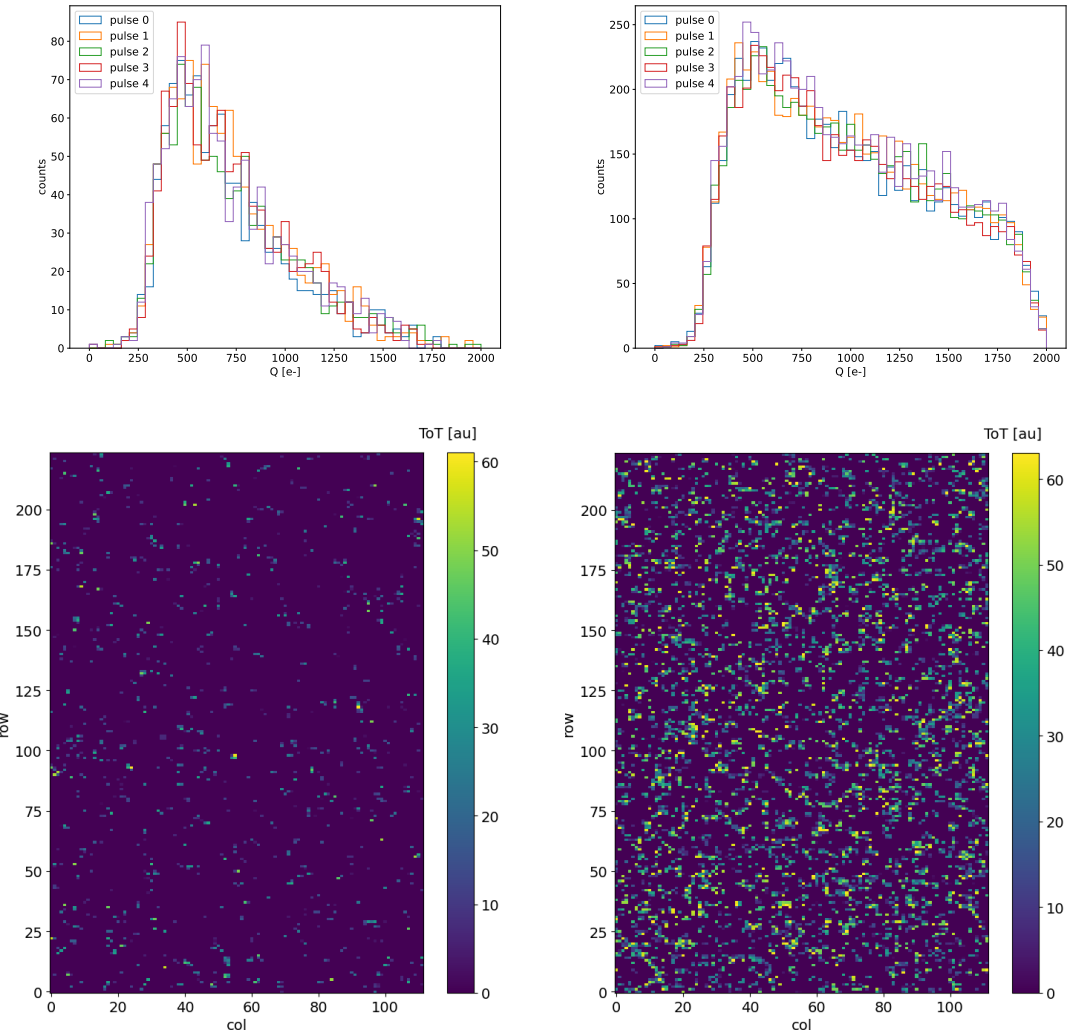


Figure 7.4: Acquisition with both the collimators: 5 pulses at $DDP=0.07$ Gy. (a) Spectrum of the charge released in the sensor: to apply the conversion I used the information found in the previous chapter. (b) 2D histogram of the ToT of the hits arrived in the sub-pulses.

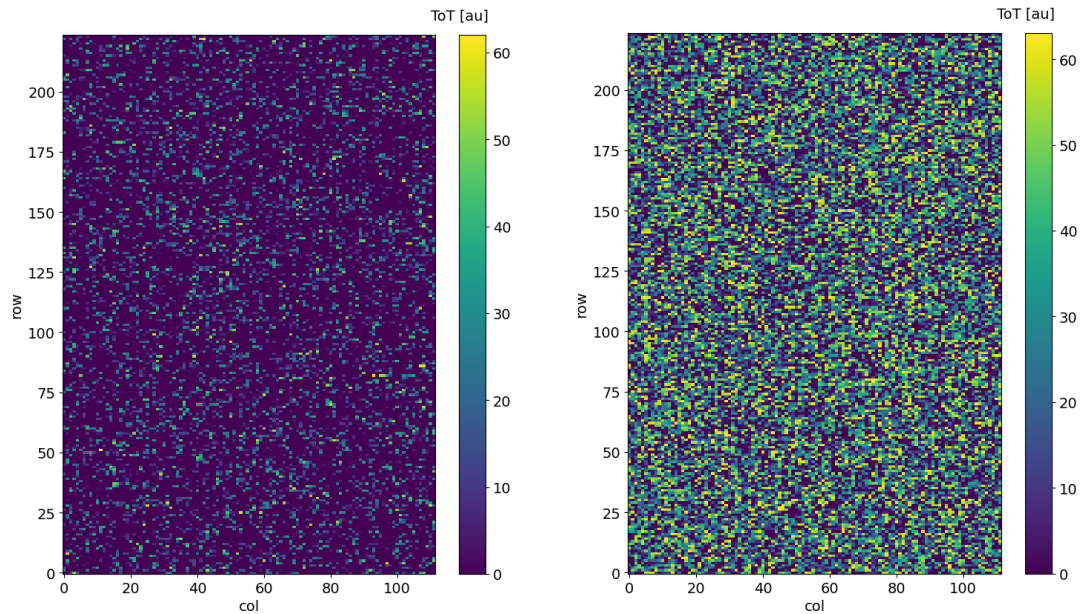


Figure 7.5: Acquisition with both the collimators: 5 pulses at DDP=0.6 Gy. 2D histogram of the ToT of the hits arrived in the sub-pulses. Compared with the previous maps, since the DDP is much higher, more pixels turn on.

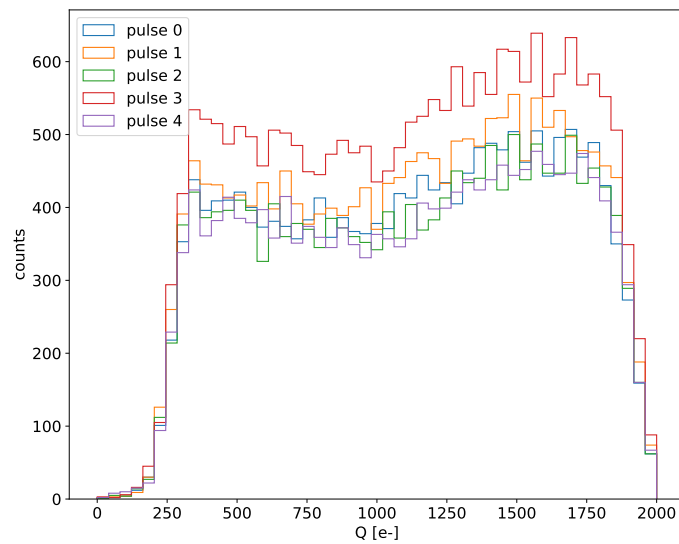


Figure 7.6: Acquisition without any collimator: 5 pulses at DDP=0.04 Gy.

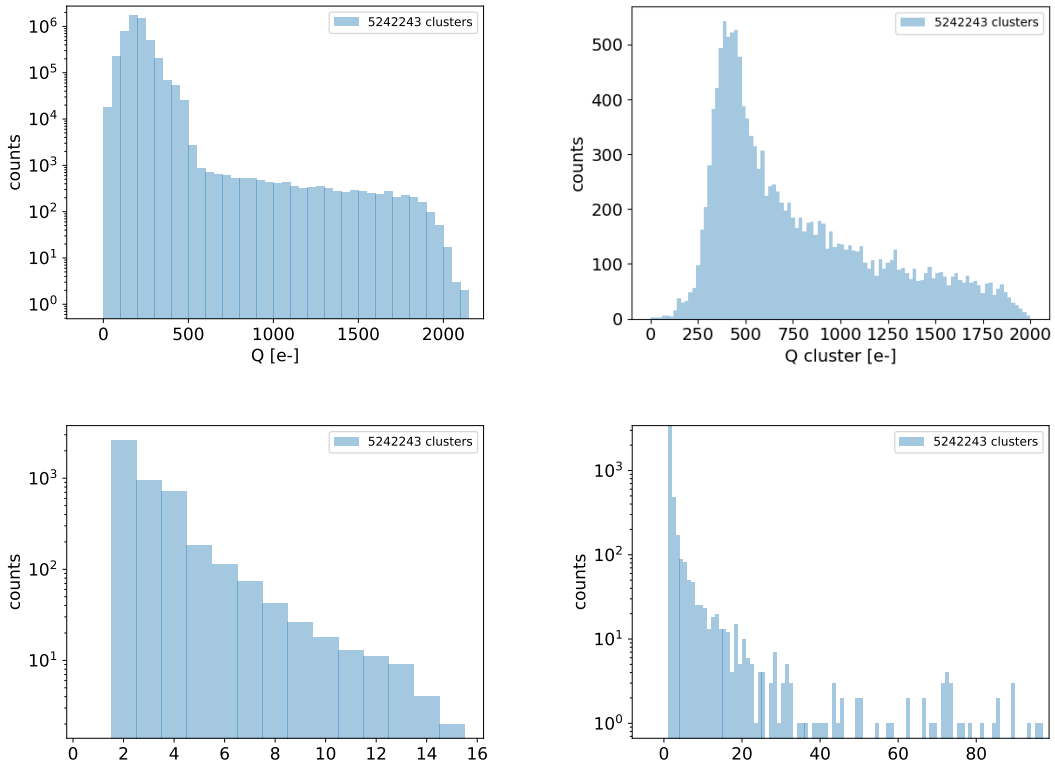


Figure 7.7: plot dei raggi cosmici da rigenerare

- 1465 • plot n di eventi che vedo con le diverse configurazioni
- 1466 • simulazione surya
- 1467 • confronta con misure dello spettro che vediamo senza e con collimatori.

1468 7.2.1 MIP spectrum using cosmic rays as source

1469 Since a MIP should produce about 2 ke- in the epitaxial layer, it should provide a signal
 1470 that in our conditions (full depletion and high gain) rolls over: in this situation making
 1471 prediction on the spectrum expected for MIPs becomes hard. Therefore, in order to
 1472 compare the spectrum observed at the testbeam with one certainly produced by MIP I
 1473 have made some acquisitions without any radioactive source, in order to look at the cosmic
 1474 ray events. To be confident with having selected MIPs from cosmic rays and cut the noise, I
 1475 have selected only the events with multiple hits: these events are mainly clusters produced
 1476 by the same impinging particle since the random coincidence probability is very low. In
 1477 fact the cosmic rays and noise rates on the whole matrix are respectively 0.02 Hz and
 1478 $\sim\text{Hz}$, the dead time in such a low occupancy condition can be always approximated with
 1479 $1\text{ }\mu\text{m}$ (this is not completely true for multiple hits events for which the priority chain
 1480 should be considered), the random coincidence rate is 10^{-8} Hz . Come mai lo spettro in
 1481 lab è diverso da quello visto con gli elettroni da 9 MeV al santa chiara? Chiedi a Surya il
 1482 rate visto sul detector senza collimatori.

1483 **Appendix A**

1484 **Pixels detector: a brief overview**

1485 **A.1 Radiation damages**

1486 Radiation hardness is a fundamental requirement for pixels detector especially in HEP
1487 since they are almost always installed near the interaction point where there is a high
1488 energy level of radiation. At LHC the ϕ_{eq} per year in the innermost pixel detector is
1489 $10^{14} n_{eq}/cm^2$; this number reduces by an order passing to the outer tracker layer [2] pag
1490 341 Wermes. Here the high fluence of particles can cause a damage both in the substrate
1491 of the detector and in the superficial electronics.

1492 The first one has a principal non ionizing nature, due to a non ionizing energy loss
1493 (NIEL), but it is related with the dislocation of the lattice caused by the collision with
1494 nuclei; by this fact the NIEL hypothesis states that the substrate damage is normalized to
1495 the damage caused by 1 MeV neutrons. Differently, surface damages are principally due
1496 to ionizing energy loss.

1497 **DUE PAROLE IN PIÙ SUL SURFACE DAMAGE** A charge accumulation in oxide
1498 (S_iO_2) can cause the generation of parasitic current with an obvious increase of the 1/f
1499 noise. Surface damages are mostly less relevant than the previous one, since with the de-
1500velopment of microelectronics and with the miniaturization of components (in electronic
1501 industry 6-7 nm transistors are already used, while for MAPS the dimensions of compo-
1502nents is around 180 nm) the quantity of oxide in circuit is reduced.

1503 Let's spend instead two more other words on the more-relevant substrate damages:
1504 the general result of high radiation level is the creation of new energy levels within the
1505 silicon band gap and depending on their energy-location their effect can be different, as
1506 described in the Shockely-Read-Hall (SRH) statistical model. The three main consequence
1507 of radiation damages are the changing of the effect doping concentration, the leakage
1508 current and the increasing of trapping probability.

1509 **Changing of the effective doping concentration:** is associated with the cre-
1510ation/removal of donors and acceptors center which trap respectively electrons/holes from
1511 the conduction band and cause a change in effective space charge density. Even an in-
1512version (p-type becomes n-type¹) can happen: indeed it is quite common at not too high
1513 fluences ($\phi_{eq} 10^{12-13} n_{eq} cm^{-2}$). A changing in the doping concentration requires an adjust-
1514ment of the biasing of the sensor during its lifetime (eq.2.2) and sometimes can be difficult
1515keeping to fully deplete the bulk.

1516 **Leakage current:** is associated with the generation-recombination centers. It has

1L'INVERSIONE OPPOSTA NON CE L'HAI PERCHÈ?

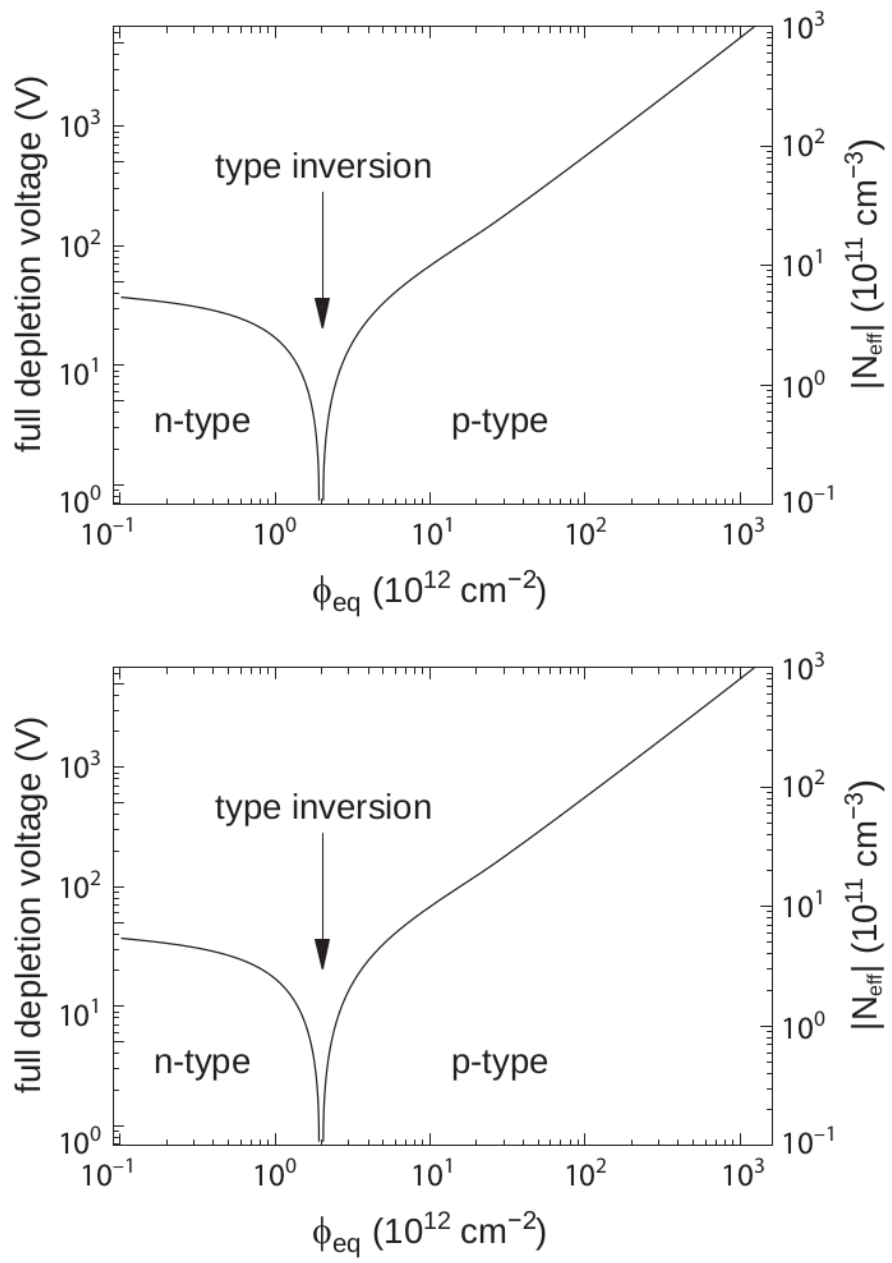


Figure A.1: 1b

1517 a strong dependence with the temperature ($I_{leak} \propto T^2$), whose solution is therefore to
1518 operate at lower temperature.

1519 **Increase of trapping probability:** since the trapping probability is constant in the
1520 depleted region, the collected charge decreases exponentially with the drift path. The
1521 exponential coefficient, that is the mean trapping path, decreases after irradiation and
1522 typical values are 125-250 μm and must be compared with the thickness of the depleted
1523 region which () corresponds to the mean drift path.

1524 Different choices for substrate resistivity, for junctions type and for detector design are
1525 typically made to fight radiation issues. Some material with high oxygen concentration
1526 (as crystal produced using Czochralki (Cz) or float-zone (Fz) process (**CONTROLLA**
1527 **LA DIFFERENZA TRA I DUE**)) for example, show a compensation effect for radiation
1528 damage; another example is the usage of n+ -in-p/n sensors (even if p+ -in-n sensors are
1529 easier and cheaper to obtain) to get advantage of inversion/to have not the inversion (since
1530 they are already p-type). After inversion the n+p boundary, coming from n+ in-n, but to
1531 keep using the sensor the depletion zone still must be placed near the diode.

1532 Single Event Upset, in sostanza è quando un bit ti cambia valore (da 0 a 1 o viceversa)
1533 perché una particella deposita carica nell'elettronica che fa da memoria registro/RAM/....
1534 Questo tipo di elettronica ha bisogno di un sacco di carica prima che il bit si "fippi"
1535 (cambi valore), infatti tipicamente per avere un SEU non basta una MIP che attraversa
1536 esattamente quel pezzo di chip in cui è implementata la memoria, ma un adrone che faccia
1537 interazione nucleare producendo più carica di quanto farebbe una MIP. Questo metodo pur
1538 essendo più comodo richiede less amount of area ha però come drawback che il registro può
1539 essere soggetto a SEU problema non trascurabile in acceleratori come HL-LHC adronici

1540

Bibliography

- 1541 [1] W. Snoeys et al. “A process modification for CMOS monolithic active pixel sensors
1542 for enhanced depletion, timing performance and radiation tolerance”. In: (2017).
1543 DOI: <https://doi.org/10.1016/j.nima.2017.07.046>.
- 1544 [2] H. Kolanoski and N. Wermes. *Particle Detectors: Fundamentals and Applications*.
1545 OXFORD University Press, 2020. ISBN: 9780198520115.
- 1546 [3] E. Mandelli. “Digital Column Readout Architecture for 10.1109/NSSMIC.2009.5402399
1547 the ATLAS Pixel 0.25 um Front End IC”. In: (2002).
- 1548 [4] M. Garcia-Sciveres and N. Wermes. “A review of advances in pixel detectors for
1549 experiments with high rate and radiation”. In: (2018). DOI: <https://doi.org/10.1088/1361-6633/aab064>.
- 1550 [5] C. Marinas. “The Belle-II DEPFET pixel detector: A step forward in vertexing in the
1551 superKEKB flavour factory”. In: (2011). DOI: [doi:10.1016/j.nima.2010.12.116](https://doi.org/10.1016/j.nima.2010.12.116).
- 1553 [6] J. Baudot. “First Test Results Of MIMOSA-26, A Fast CMOS Sensor With Inte-
1554 grated Zero Suppression And Digitized Output”. In: (2010). DOI: [doi:10.1109/NSSMIC.2009.5402399](https://doi.org/10.1109/NSSMIC.2009.5402399).
- 1556 [7] A. Dorokhov. “High resistivity CMOS pixel sensors and their application to the
1557 STAR PXL detector”. In: (2011). DOI: [doi:10.1016/j.nima.2010.12.112](https://doi.org/10.1016/j.nima.2010.12.112).
- 1558 [8] Giacomo Contin. “The STAR MAPS-based PiXeL detector”. In: (2018). DOI: <https://doi.org/10.1016/j.nima.2018.03.003>.
- 1560 [9] Nolan Esplen. “Physics and biology of ultrahigh dose-rate (FLASH) radiotherapy:
1561 a topical review”. In: (2020). DOI: <https://doi.org/10.1088/1361-6560/abaa28>.
- 1562 [10] Fabio Di Martino et al. “FLASH Radiotherapy With Electrons: Issues Related to
1563 the Production, Monitoring, and Dosimetric Characterization of the Beam”. In:
1564 *Frontiers in Physics* 8 (2020). ISSN: 2296-424X. DOI: [10.3389/fphy.2020.570697](https://doi.org/10.3389/fphy.2020.570697).
1565 URL: <https://www.frontiersin.org/articles/10.3389/fphy.2020.570697>.
- 1566 [11] M. Dyndal et al. “Mini-MALTA: Radiation hard pixel designs for small-electrode
1567 monolithic CMOS sensors for the High Luminosity LHC”. In: (2019). DOI: <https://doi.org/10.1088/1748-0221/15/02/p02005>.
- 1569 [12] M. Barbero. “Radiation hard DMAPS pixel sensors in 150 nm CMOS technology
1570 for operation at LHC”. In: (2020). DOI: <https://doi.org/10.1088/1748-0221/15/05/p05013>.
- 1572 [13] K. Moustakas et al. “CMOS Monolithic Pixel Sensors based on the Column-Drain
1573 Architecture for the HL-LHC Upgrade”. In: (2018). DOI: <https://doi.org/10.1016/j.nima.2018.09.100>.

- 1575 [14] I. Caicedo et al. “The Monopix chips: depleted monolithic active pixel sensors with
1576 a column-drain read-out architecture for the ATLAS Inner Tracker upgrade”. In:
1577 (2019). DOI: <https://doi.org/10.1088/1748-0221/14/06/C06006>.
- 1578 [15] D. Kim et al. “Front end optimization for the monolithic active pixel sensor of the
1579 ALICE Inner Tracking System upgrade”. In: *JINST* (2016). DOI: doi:10.1088/
1580 1748-0221/11/02/C02042.
- 1581 [16] L. Pancheri et al. “A 110 nm CMOS process for fully-depleted pixel sensors”. In:
1582 (2019). DOI: <https://doi.org/10.1088/1748-0221/14/06/c06016>.
- 1583 [17] L. Pancheri et al. “Fully Depleted MAPS in 110-nm CMOS Process With 100–300-
1584 um Active Substrate”. In: (2020). DOI: 10.1109/TED.2020.2985639.